INTEGRATING CAVITY ENHANCED SPECTROSCOPY FOR LIQUID AND GAS SENSING

A Dissertation

by

JOEL NATHAN BIXLER

Submitted to the Office of Graduate and Professional Studies of
Texas A&M University
in partial fulfillment of the requirements for the degree of

DOCTOR OF PHILOSOPHY

Chair of Committee,	Vladislav V. Yakovlev
Committee Members,	Gerard L. Coté
	Edward S. Fry
	Kristen C. Maitland
Head of Department,	Gerard L. Coté

December 2015

Major Subject: Biomedical Engineering

ABSTRACT

With continued advances in optical instrumentation coupled with new highly specific contrast methods, optical based spectroscopic techniques continue to find new applications in a wide range of fields from medical diagnostics to analytical chemistry. Fluorescence based detection has been used in a variety of medical and environmental sensing applications. Raman spectroscopy has long been used in a variety of industries and applications due to its unique ability to provide label free chemically specific information about a molecule. While both of these techniques have tremendous potential in both medical diagnostics and environmental sensing, often cost efficiency and sensitivity limit more wide spread use.

To overcome these limitations, we explore the use of integrating cavity enhanced spectroscopy as a means to greatly enhance the detection sensitivity of both Raman and fluorescence spectroscopy based detection. Using a new diffuse reflector, we have constructed novel integrating cavities that provide significant enhancement of linear optical processes. Enhancement of these processes stems from the long optical pathlength light experiences inside the cavity combined with the relatively large volume that can be probed when compared to traditional spectroscopic approaches. Integrating cavities have several advantages over other sources of signal enhancement in that there is no need for high cost laser sources, and the broad range of wavelengths over which the cavity is reflective affords the ability to use ultraviolet (UV) and blue excitation wavelengths. Raman spectroscopy greatly benefits from the use of more blue shifted sources. Additionally, this allows for one to take advantage of the endogenous fluorescence of many organic molecules that fluoresce under UV excitation.

The enhancement of both spontaneous Raman generation as a result of the integrating cavity is demonstrated by measuring the sensitivity of detection for three aromatic hydrocarbons. Fluorescence enhancement is demonstrated by exploring the detection limits of a urobilin zinc phosphor complex, a biomarker that has been shown to be a viable indicator of human and animal waste contamination in water sources. Finally, the design of a integrating cavity system for gas phase analysis will be demonstrated.

To my parents, Nathan and Mary,

and Brody

ACKNOWLEDGEMENTS

This work would not have been possible without the guidance and support of Dr. Vladislav V. Yakovlev. I would like to thank you for allowing me to work on this project, and for being an exceptional mentor over the last three years. I would like to show appreciation to Dr. Kristen C. Maitland, who served as my advisor during the pursuit of my master's degree. Your mentoring has been instrumental in my development as a researcher. I would also like to thank the rest of my committee, Dr. Gerard L. Coté and Dr. Edward S. Fry. Without the collaborations with Dr. Fry's laboratory, much of this work would not have been possible.

Many of my fellow graduate students have provided tremendous support over the years. I would like to thank my fellow labmates, Brett Hokr, Zhaokai Meng, Andrew Traverso, Jonathan Thompson, and Dawson Nodurft. Brett has been a tremendous source of knowledge, and I have greatly enjoyed the discussions we have had and the projects we have been able to work on together. Casey Pirnstill, Alex Abraham, Cory Olsovsky, Haley Marks, John Mason, and Michael Cone have all been great sources of assistance, discussion, and friendship during this work. Chase Winkler has also been a tremendous help with data collection for some of the experiments reported here.

I would like to extend a special thanks to the staff of the Air Force Research Laboratory who have supported me during my research. Dr. Robert Thomas, Dr. Benjamin Rockwell, and Gary Noojin have all been very helpful and supportive. I would also like to acknowledge support by the AFRL Pathways program, which provided financial support for part of my time at Texas A&M.

My parents, Nathan and Mary Bixler, have been a major source of love and

support during my pursuit of my doctorate. My father has been one of my biggest sources of inspiration, and one of the major reasons I decided to obtain a doctorate in the first place. Without their unconditional support, I do not think I could have completed this journey. My brother Daniel and sister Rachel have also been incredibly supportive of my endeavors, and I'd like to thank them as well. Finally, I'm of the mindset that pets are family as well. I've had Brody since he was an 8 week old puppy, and his unconditional love has helped me relax in times of stress, helped me celebrate in times of joy, and been the best of friends anyone could ask for.

TABLE OF CONTENTS

Page

LIST OF FIGURES

FIGURE Page

LIST OF TABLES

TABLE Page

1. INTRODUCTION

1.1 Motivation

Access to clean water and air is critical for human health. Pathogens found in water are estimated to cause greater than 2 million deaths annually around the world in addition to the countless number of illnesses they cause.[1] As industrialization continues to spread to new parts of the globe, water sources can become polluted with industrial waste rendering the water source non-potable for the local populations. Agricultural contaminants and waste products also greatly contribute to disease from drinking such water. As societies continue the shift towards more urban populations, water supplies that service these large population densities become a more valuable and vital commodity. It is critical that we develop cost effective methods that can allow for safe reuse of water, such that the needs of competing interest groups can be met.

Additionally, other industrial pollutants, such as the exhaust released from the incomplete burning of fossil fuels can present carcinogenic hazards. Research suggests that prolonged exposure to air pollution can cause cardiorespiratory diseases along with presenting neurotoxic effects.[2] As new methods to harvest energy are developed, it is critical to be able to monitor the air and water quality impact such technologies have.[3]

Breath analysis is another area where significant research is needed. Many currently used methods for diagnosing, monitoring and managing respiratory related diseases are invasive and often lack sensitivity to detect these diseases in their early state. Early detection can offer additional options for treatment and management.[4] Recent work in the area of breath analysis has shown that the detection and quan-

tification of volatile organic compounds (VOCs) can be used as biomarkers for physiological function and disease activity.[5–9] These compounds often are exhaled in the parts per billion (ppb) to parts per trillion (ppt), so highly sensitive techniques are needed to accurately detect and quantify exhaled VOCs.[10,11]

1.2 Current Sensing Standards

Modern analytical techniques such as liquid chromatography coupled with mass spectrometry (LC-MS), gas chromatography coupled with spectrometry (GC-MS), and tandem spectrometry (MS/MS) are quite powerful at detection and identification of small molecules, and are considered the gold standard for many detection applications. These techniques are employed for a variety of sensing applications ranging from protein identification and drug screening to detection of waste products in water sources.[12–14] These techniques provides highly sensitive analytical information by measuring the mass-to-charge ratio and abundance of gas-phase ions. Liquid or gas chromatography are used for the analytical separation of volatile substances in liquid and gas phases respectively. In gas chromatography, the components of a sample are heated or dissolved in a solvent and vaporized in order to separate the analytes. A carrier gas, such as helium, is used to carry the components of the sample into a GC column where separation takes place. The sample can then be passed to a mass spectrometer for detection. A basic schematic of this detection system is shown in Fig. 1.1. A liquid chromatography achieves separation by introducing the sample volume to be analyzed to a solvent under high pressure. The components are then passed through an analytical column filled with absorbent material. Separation occurs based on the different interactions each molecule has with the absorbent column.[15,16]

Mass spectrometry-based detection techniques are quite powerful at analyzing

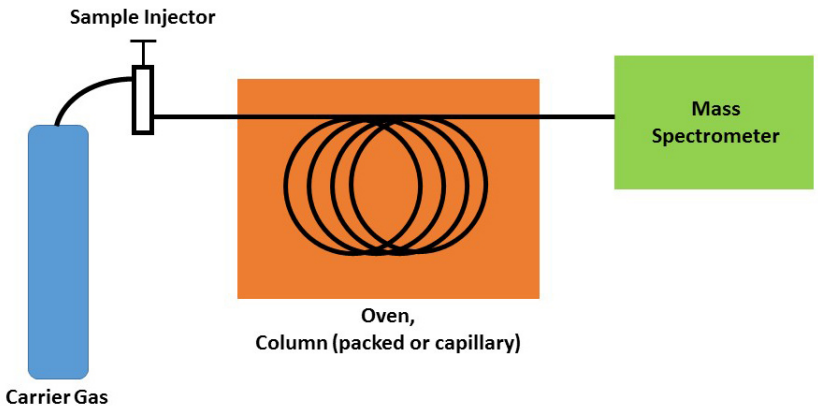

Figure 1.1: Schematic illustrating the basic operating principles of GC-MS

complex mixtures, and have found applications in a broad range of fields such as basic research, pharmaceuticals, agricultural, and medicine. While such technologies are quite powerful, they remain very expensive and often require a significant time delay between sample collection and analysis as samples taken from the field need to be shipped back to a laboratory for analysis. Additionally, expert interpretation is needed to analyze the results.[17–19]

1.3 Optical Sensing Techniques

Optical spectroscopic techniques are proving to be a viable substitute for LC-MS or MS/MS in some applications. Here, we will focus on fluorescent and Raman spectroscopy, as these methods have both been applied to a broad range of biomedical applications. Both techniques can provide highly specific detection of molecules of interest, and each has its own advantages and disadvantages. Non-linear counter-

parts exist for both Raman and fluorescent spectroscopy which can provide enhanced contrast.

1.3.1 Raman Spectroscopy

Raman spectroscopy has been used for decades as a means to provide detailed chemical information about a sample without the need for exogenous contrast. The technique has been applied to a variety of applications in the fields of physics, chemistry and the biomedical sciences, ranging from medical diagnostics to industrial control.[20–22] Raman spectroscopy is based on phenomenon of Raman scattering, which involves the inelastic scattering of incident photons from a molecule.

Raman spectroscopy probes the vibrational energy levels of the molecule, which are specific to the chemical bond structure and symmetry of an individual molecule, allowing for label-free, chemical identification via a spectroscopic fingerprint. Figure 1.2 shows the energy level diagrams for both Rayleigh and Raman scattering. The spontaneous Raman effect was first predicted in 1923 by Adolf Smekal and observed experimentally in 1928 by Sir Chandrasekhara Vankata Raman.[23] Suppose that we have a molecule in some vibrational state, shown as E_0 in Fig. 1.2. An incident photon of energy $h\nu_0$ is absorbed, raising the system to some intermediate or virtual state. It immediately makes a Stokes transition, emitting a photon of energy $h\nu_0 < h\nu_m$ or an anti-Stokes transition where $h\nu_0 > h\nu_m$. The difference in energy is given by equation 1.1 based on the conservation of energy where $h\nu_m$ corresponds to the molecular vibrational transition.

$$h\nu_m = h\nu_i - h\nu_s \tag{1.1}$$

The Raman shift can be calculated based on equation 1.2 where $\Delta\omega$ is the Raman shift, λ_{ex} is the excitation wavelength, and λ_{em} is the emission wavelength.

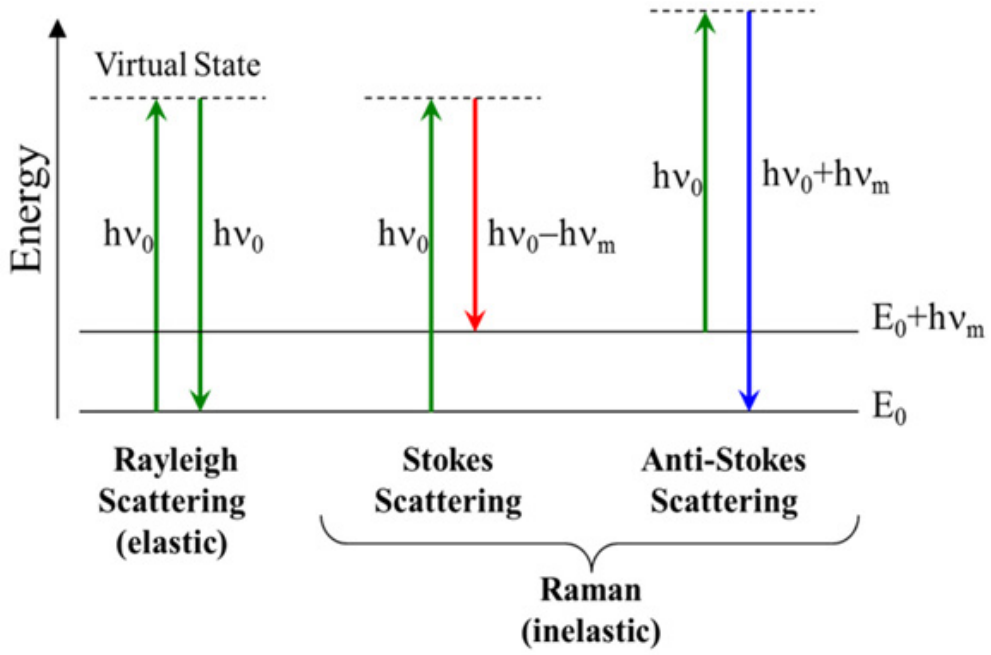

Figure 1.2: Energy level diagram describing Rayleigh (elastic) and Raman (inelastic) scattering. Raman scattering can occur as both a Stokes and anti-Stokes process.

$$\Delta\omega = (\frac{1}{\lambda_{ex}} - \frac{1}{\lambda_{em}}) * 10^7 \tag{1.2}$$

The factor of 10^7 converts the wavelength in nm to cm^{-1}, the common unit for Raman shifts. This allows for a Raman spectrum to be presented in the same format, regardless of excitation wavelength. It should be noted that Raman transitions are narrow in bandwidth. In most Raman spectroscopy applications, the measured Raman peak will be a convolution bandwidth of the laser source and Raman transition. The narrow emission allows for Raman spectroscopy to provide a spectral fingerprint for the molecule being probed.

The spontaneous Stokes Raman scattering is an inherently weak process, where only approximately 1 in 10^8 scattered photons carry the desired vibrational infor-

mation. This is because Raman cross-sections are quite small relative to Rayleigh scattering cross-sections, causing Rayleigh scattering to be the dominate process. Typcial Raman cross-sections are on the order of $\sigma_R \sim 10^{-30}$ cm^2/sr. The Raman cross-section does scale with a λ^{-4} dependence, allowing for increased signal generation through the use of blue shifted excitation sources. Since this is a linear optical phenomena, the signal intensity scales linearly with the input power as well.[20,24] For many applications, laser power can only be increased until the point where it begins to damage the sample of interest. Additionally, high power laser sources can be costly, limiting their availability in commercial or research applications.

This limitation has lead researchers to pursue methods to significantly enhance signal generation to allow for Raman spectroscopy to reach new applications.[25] Methods such as coherent anti-Stokes Raman spectroscopy (CARS) and surface enhanced Raman spectroscopy (SERS) both can provide significant enhancement to this, but require expensive laser source or individually tailored surface chemistry to enhanced the detection of a specific molecule.[26] CARS is a non-linear technique in which a pump and stokes beam interact with a sample. When the difference between the pump, ω_p, and Stokes, ω_s, frequencies match the molecular vibrational frequency, Ω_{vib}, the anti-Stokes signal is generated at a frequency given by equation 1.3.

$$\omega_{as} = 2\omega_p - \omega_s \tag{1.3}$$

This is depicted in the energy diagram shown in Fig. 1.3. CARS has been applied to a wide range of biomedical imaging applications.[22,27–30] These have ranged from chemically specific cell and metabolic imaging, as well as applications in cancer detection.[21,31]

SERS is another commonly used enhancement technique for Raman spectroscopy.

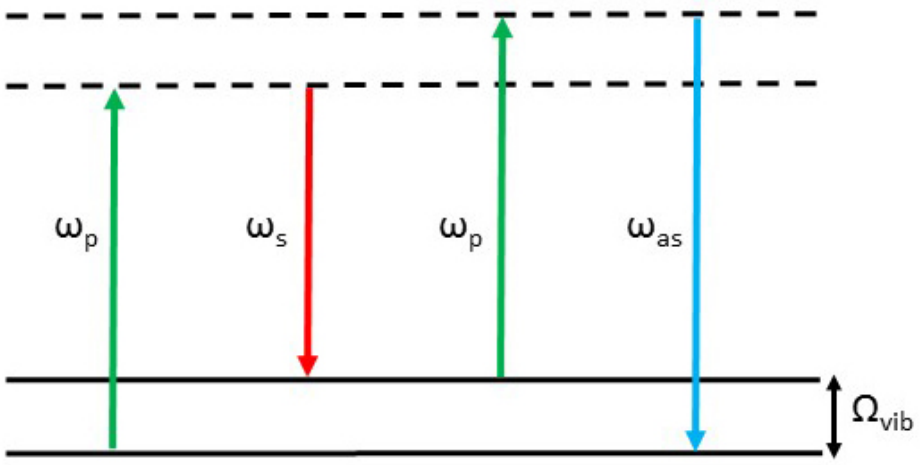

Figure 1.3: Diagram of the coherent anti-Stokes Raman scattering (CARS) process.

This approach provides enhancement by exciting localized surface plasmons of rough metallic nanoparticles. If a molecule of interest is located near this "hot spot," significant Raman enhancement can occur via localized surface plasmon resonance. For metalic nanoparticles, the maximum enhancement factor is given by 1.4 where E_{out} is the electromagnetic field outside the particle, E'_{out} refers to the field evaluated at the scattered frequency, and E_0 is the incident field intensity.[27]

$$EF = \frac{|E_{out}|^2 |E'_{out}|^2}{|E_0|^4} \tag{1.4}$$

Enhancement factors of up to 10^{14} have been reported using this technique, allowing for single molecule detection.[32] One limitation of this is that the molecule of interest must be within a few nanometers of the nanostructure surface to experience the enhancement. In order to provide molecular specificity, SERS substrates treated with functionalization techniques to bring the analyte closer to the metal structure.

Thus, specialized complex surface chemistry is required to be developed for each molecule of interest. This process can be timely, and can limit the practical use of SERS for biomedical sensing. This has lead to difficulties in reusing SERS substrates, where irreversible binding or changes in binding kinetics over time lead to issues in repeatability in measurements. Still, significant research has been put into the field of biomedical sensing applications, where detection of trace biomarkers in solution is required.[22,33]

While both CARS and SERS have found numerous applications in biological imaging and sensing, they each suffer in the arena of gas sensing. Absorption of gas phase molecules of interest onto SERS substrates has been demonstrated.[34] This method struggles to provide quantitative data, as the absorption kinetics can depend on temperature and time. Because of this, there is the need to develop an optical technique capable of providing chemically specific information on both liquid and gas phase samples with high sensitivity. Such a technique could have significant impact on gas sensing in both medical and environmental applications. The ability to make these measurements in near real time, and in locations outside of a research laboratory or clinical setting is also key to the adaptation of a new optical technique.

1.3.2 Fluorescence Spectroscopy

Similar to Raman scattering, fluorescent emission is an inelastic process involving a photon interacting with a sample. Generation of photons through the absorption of ultraviolet (UV) or visible light photons is a phenomenon termed photoluminescence, which can be divided into two major categories of fluorescence and phosphorescence. The difference between these two processes is based on the electronic configuration of the excited states and emission pathways. Fluorescent emission occurs when the radiative transitions are spin-allowed. This is the case when the transition takes

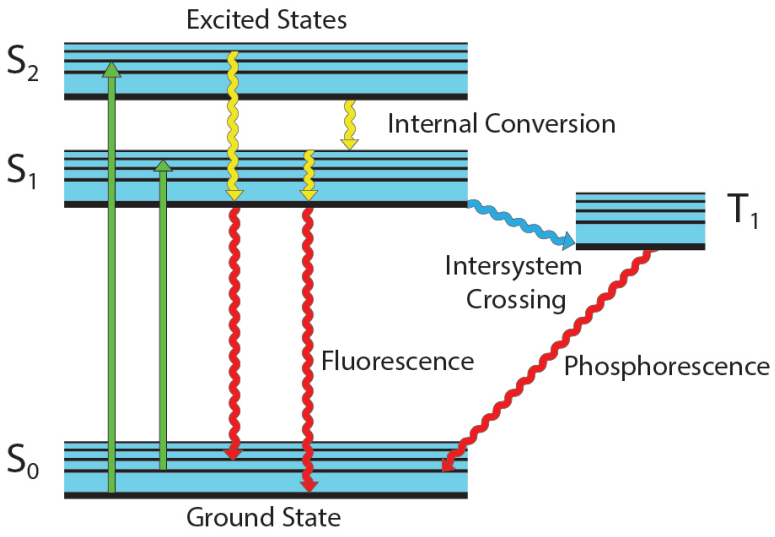

Figure 1.4: Energy level diagram for fluorescence and phosphorescence emission.

place between two states with equal multiplicity, i.e., singlet → singlet or triplet → triplet.[35] Fig. 1.4 shows the energy level diagram, or Jablonski diagram, for photoluminescence transitions. S_0, S_1, and S_2 correspond to the singlet states, and T_1 is the first triplet state. Green arrows show the absorption of excitation radiation, in this case green photons of wavelength 532 nm. Following the absorption, the system experiences relaxation followed by emission of a fluorescent photon. This is shown by the red lines pointing from S_1 to S_0. A transition from the singlet state, S_1, to the triplet state, T_1 is shown by the blue arrow. When this occurs, phosphorescence emission can occur by a decay back to the ground stat.

Fluorescence, unlike Raman scattering, has a time dependence to the decay. Excitation of a susceptible molecule by an incident photon occurs on the order of femtoseconds (10^{-15}). Vibrational and thermal relaxation from the excited state to the lowest energy level is significantly slower, occurring on the picosecond (10^{-12}) scale. The emission of a fluorescent photon typically occurs on the nanosecond (10^{-9}) timescale. As the decay is easily measurable with a fast photodetector, this information is used

to provide additional information about a system.[36] In the case of phosphorescence, the decay time is even longer, typically on the order of microseconds (10^{-6}).

Unlike Raman scattering which can occur from any excitation wavelength, fluorescent molecules have an absorption band. Only photons that fall within this band can result in fluorescent emission. If the incident photon contains more energy than is needed, the excess energy is usually converted to vibrational and rotational energy. On the other hand, if the incident photon does not have enough energy, no absorption occurs. The emission spectrum is independent of the excitation energy, as long as the source used falls within the absorption band. This is because, as shown in Fig. 1.4, rapid internal conversion from a higher energy band to the lowest vibrational energy level of the excited state S_1 occurs. It should be noted that all subsequent relaxation pathways, such as fluorescence emission or intersystem crossing, occur from the lowest vibrational level of the excited state S_1.

The phosphorescence excitation and emission spectrum of a urobilin-zinc acetate complex is shown in Fig. 1.5. This figure shows typical broad emission that is characteristic of fluorescence or phosphorescence. The shift between the absorption peak and emission peak wavelength is knows as the Stokes shift, named after George G. Stoke who first described the effect in 1852. Unlike Raman, there is no anti-Stokes counterpart to the emission.

Fluorescence does have the advantage over Raman scattering in that it is a much stronger effect. The quantum yield of a fluorophore is given by equation 1.5. For many fluorophores, this value can be greater than 50%, allowing for very sensitive detection.[37]

$$\Phi = \frac{photons\ emitted}{photons\ absorbed} \tag{1.5}$$

Fluorophores can subject to quenching and photobleaching, reducing the effective

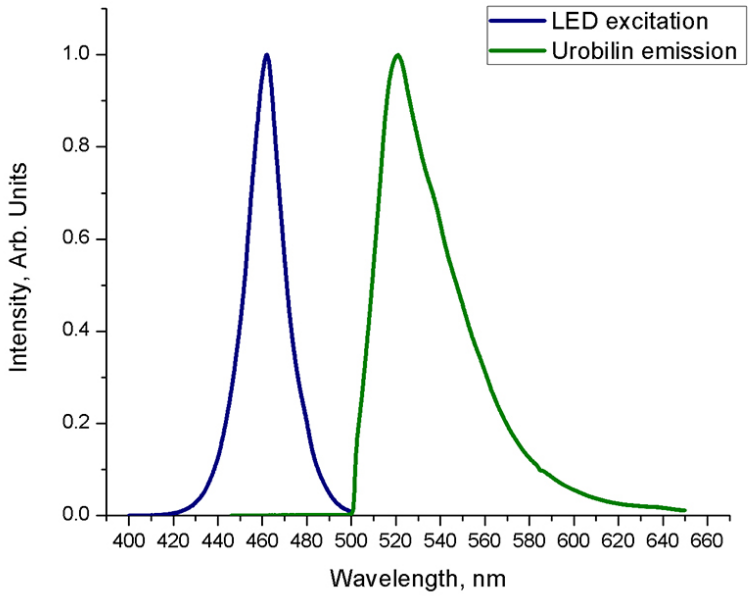

Figure 1.5: Excitation and emission spectrum of urobilin phosphor complex. The excitation is shown in blue, while the excitation is shown in green.

emission measured. These two phenomena differ in that quenching is a reversible process arising from a variety of competing processes that result in non-radiative relaxation from the excited state. Photobleaching occurs when a fluorophore permanently loses the ability to generate fluorescence due to chemical damage. Often, this occurs when a molecule in an excited triplet state interacts with another molecule resulting in covalent modifications.

Fluorescence has found widespread applications in biology and medicine. Multiphoton fluorescence has allowed for imaging in the brain through the skull using the second near infrared window.[38,39] Fluorescence tomography techniques have been used to study metabolic activity.[40] Microendoscopy techniques utilizing fluorescence have been studied with the hope of replacing traditional biopsy.[41–46] Fluorescence-based immunoassays have been developed for a variety of sensing applications, and

are commonly used world-wide.[47] Some researchers have even demonstrated single molecule detection, although often in controlled systems.[48,49]

Water quality monitoring is another area where fluorescence spectroscopy can be used. When water travels through the environments, it can collect dissolved organic material (DOM) composed of various chemical compounds. Fluorescence spectroscopy can provide information about the amount and type of DOM in a water supply. The amount of DOM in water can be important for a variety of things such as urban planning, ecological studies, along with understanding the effects of the trace organic matter on the ecosystem the water supply supports.[50]

1.4 Conclusion

Both Raman and fluorescence-based spectroscopy have the potential to greatly enhance currently used detection techniques such as GS-MS, LC-MS, and MS/MS, but lag behind in terms of absolute sensitivity. If the detection limits can be enhanced, optical-based sensing techniques could find more applications in environmental monitoring, medical diagnostics, and in every day use. This is particularly true if the total cost of the system and analysis can be significantly reduced. As optical technology continues to decrease in cost, there is plenty of opportunity to make this a reality.

While numerous enhancement schemes have been developed for Raman scattering, cost and repeatability still prohibit wide-spread adoption. This dissertation will focus on the use of integrating cavities as an enhancement method for linear optical processes such as spontaneous Raman scattering and fluorescence emission. Previous techniques for cavity enhanced spectroscopy will be discussed in Chapter II, followed by a general discussion of the theory of integrating cavities in Chapter III. Raman enhancement utilizing an integrating cavity will be discussed in Chapter IV, fol-

lowed by the demonstration of fluorescence enhancement in Chapter V. A discussion of practical methods for implementing integrating cavity enhanced spectroscopy will be discussed in Chapter VI. Finally, the direction of future work and conclusions will be discussed in Chapter VII.

2. CAVITY ENHANCED SPECTROSCOPY

2.1 Introduction

Optical cavities are one of the fundamental components of a laser. Resonant optical cavities consisting of two highly reflective mirrors aligned parallel to each other, allows for light to circulate in a closed path. When placed around gain medium, the feedback of the optical resonator allows for stimulated emission and the buildup of radiation. By allowing light to leak out from one of the ends of the optical resonator, a laser beam can be created. Pulsed laser system often utilize high quality (high-Q) optical resonator to generate short pulses with high peak power. While perhaps the most important application of an optical cavity is in laser physics itself, they have found widespread applications in other areas related to physics, chemistry, and highly sensitive spectroscopy.[51] Many other forms of optical cavities, such as whispering gallery mode resonant cavities have found applications in biosensing.[52,53]

One of the most common applications for optical cavities is for highly sensitive absorption spectroscopy. Cavity ring-down spectroscopy has been used to measure the absorption of numerous weakly absorbing materials.[5,54,55] The high sensitivity stems from the incredibly long interaction length between the matter and field inside a high finesse cavity. Multiple passes through an weakly absorbing material allow for enhanced sensitivity in absorption measurements. This technique has produced significantly higher sensitivity than obtainable in conventional absorption spectroscopy. In this Chapter, we will review applications and the optical approaches commonly used for cavity ring-down spectroscopy. Following this, we will look at what has been done in the field of cavity enhanced Raman spectroscopy.

2.2 Cavity Enhanced Absorption Spectroscopy

Direct absorption spectroscopy of atoms or molecules in a gas phase is a powerful tool used in the field of chemistry. Absorption spectroscopy can provide information about quantitative concentrations as well as measuring the frequency-dependent absorption cross-section. Conventional absorption spectroscopy techniques use a broad band source that is passed through a sample. The transmittance of the probe radiation is measured by a photodetector on the opposite side of the sample. Changes in the intensity of the source are used to calculate absorption based upon the Beer-Labmert law given in equation 2.1.

$$T = \frac{I}{I_0} = e^{\sigma l N} \tag{2.1}$$

Here, T is the transmittance, I_0 and I are the intensities of the incident and transmitted radiation respectively, σ is the attenuation cross-section, l is the path length, and N is the concentration of the molecule being probed. The sensitivity of this technique is limited by the ability to measure small changes in transmission over any noise in the source or detector. Sensitivity can thus be increased by increasing the pathlength, l, through the sample.

One way to greatly enhance the detection sensitivity of absorption spectroscopy is by placing the sample inside of a high finesse optical cavity. By doing this, the effective pathlength of the incident radiation through the sample can be greatly increased based on the number of passes a photon will travel through that sample. This concept has lead to the development of cavity ring-down spectroscopy (CRDS). Here, instead of measuring the magnitude of the absorption of light, the rate of absorption is probed. To do this, the time decay of light leaking out of the cavity is measured as opposed to the absolute intensity. The decay time can then be related

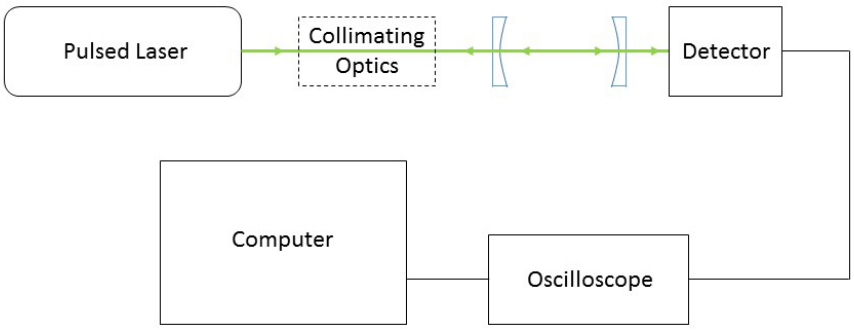

Figure 2.1: A block diagram for the typical experimental setup for cavity ring-down spectroscopy. Here, the collimating optics are optional depending on the output quality of the source. (Adapted from Berden *et al.*[55])

back to the concentration of absorber inside the cavity. This relationship will be discussed in more detail in Chapter 3.

The idea to use an optical cavity to measure absorption can originally be traced back to work done by Herbelin *et al.* done in 1980.[56] Here, Herbelin *et al.* proposed the idea to use an optical cavity to measure the reflectance of mirror coatings. These reflection losses are in a way a measure of the absorption of the optical coatings. This was done by modulating the intensity of a continuous wave (CW) light source, and measuring the phase shift created by the cavity. Shortly after, Anderson *et al.* developed the idea of abruptly turning off the light source and measuring the decay in intensity of the light leaking out of the cavity.[57] This method allowed for more accurate measurements of absorption. The development of pulse lasers lead to wide-spread adaptation of this technique for sensitive absorption measurements.

The typical experimental setup used for CRDS is shown in Fig. 2.1. A pulsed laser source is often used to allow for absorption measurements, but this source can be CW. The collimating optics are optional depending on the beam quality of the laser

source. The ring down cavity consists of two highly reflective mirrors separated by some distance, d. A fast photodiode connected to an oscilloscope is use to measure the decay in light intensity. The readout of the oscilloscope is then read in by a computer so that the data can be recorded and saved.

Cavity enhanced absorption spectroscopy has previously been applied to the analysis of exhaled breath. Studies primarily using GS-MS have shown that there exists a panel of volatile organic compounds that are exhaled along with CO_2, H_2O, and N_2 in trace quantities that can be used to diagnose diseases such as lung cancer, chronic obstructive pulmonary disorder, and asthma among others.

Several optical-based techniques that utilize the basic principles of cavity ring down spectroscopy have been explored for use in applications related to breath analysis. The most common techniques used are cavity ring down spectroscopy (CRDS),[58] integrating cavity output spectroscopy (ICOP),[59] cavity enhanced absorption spectroscopy (CEAS),[60] along with variants of CEAS such as off-axis cavity-enhanced absorption spectroscopy(OA-CEAS).[61]

The experimental setup commonly used in CRDS was shown in Fig. 2.1. This technique is a direct absorption technique that can be preformed with pulsed or continuous light sources with higher sensitivity attributed to the use of a high-Q cavity. Much of the literature published on this technique demonstrates detection of a single gas, though multiplexing schemes are available.[55] This limitation exists due to the fact that a laser source is used in conjunction with a fast photodiode, providing no spectral information. If the source is capable of being swept in frequency, additional information about the absorption cross-section of the sample being probed can be obtained, but analysis is limited to the bandwidth of the source. Commonly, diode lasers are used for this, but with limited tuning range.

ICOS detection can be considered to be identical to CEAS, although ICOS is

traditionally used when pulsed laser sources are employed as opposed to continuous sources. This technique also has limited free spectral range, and the range decreases with the number of beam round trips. The detection of biomarkers present in breath with these techniques requires narrow linewidth ($<$ 1 MHz), wavelength-tunable, single-mode sources such as an external cavity laser.[61] Still the tuning range is often limited to 80 to 100 nm, providing limited absorption information, particularly for complex systems. Additionally, many of the VOCs of interest absorb in the infrared, requiring sources that output between 1.5 or 2 μm. Detection in this range requires more costly indium gallium arsenide (InGaAs) detectors.

To obtain the needed sensitivity, the cavity length must be kept relatively long. Typical cavity enhanced sensing schemes use cavity lengths on the order of 1m, thus the total device can be bulky and cumbersome. Additionally, because of the spectral reflective nature of the highly reflective cavity mirrors used, laser sources must be carefully aligned into the cavity. This alignment is extremely delicate, thus limiting the use of these devices in the field. Any slight misalignment of the source into the high-Q cavity would render the system useless, and significant time from a trained technician would be required to restore operation. The mirrors used can also be costly, and are extremely sensitive to damage. The gain in the cavity is proportional to the mirror reflectivity and is given by equation 2.2 where G is the cavity gain factor, and R is the mirror reflectivity.[62]

$$G = \frac{R}{(1 - R).} \tag{2.2}$$

Cavity ring down spectroscopy as been used over a broad range of wavelengths to provide absorption information on gas phase sample, but limitations still exist. One limitation that has not yet been discusses is error caused by scattering. Since these

techniques only measure an attenuation of light intensity over time, if the absorption cross-section is not significantly larger than the scattering cross-section, this can result in large amounts of error in the measurements produced.

2.3 Cavity Enhanced Raman Spectroscopy

While there are many reports that utilize cavity enhanced absorption spectroscopy for highly sensitive spectroscopy, less research has been preformed related to the use of an optical cavity to enhance spontaneous Raman scattering effect. As previously mentioned, Raman cross-sections are typically quite small, often on the order of 10^{-30} cm^{-1}, and thus methods to enhance this optical phenomenon are needed to open the door for more applications for Raman spectroscopy, particularly for medical diagnostic purposes.

In literature, cavity enhanced Raman scattering (CERS) can refer to one of two techniques with very different operating principles. Symes *et al.* published a report in 2006 where they defined CERS to be a non-invasive Raman technique in which the illuminating pump and scattered frequencies are spectrally coincident with resonant modes of a spherical microdroplet. These modes are commonly referred to as whispering galley modes or morphology dependent resonances. Here, the incident radiation remains trapped within the whispering galley mode, allowing for the intensity of both the incident laser light and Raman scattered wavelengths to build providing conditions to generate nonlinear stimulated Raman scattering (SRS).[63] Using this technique, a gain factor of 5 was observed, only allowing for detection limits on the order of millimolar of nitrates such as $NaNO_3$. The optical system in these experiments consisted of a neodymium-doped yttrium aluminium garnet (Nd:YAG) laser pump laser and a Dye laser that was used as a seed. A portion of the 532 nm emission from the Nd:YAG was used to seed the Dye laser.Thus, the optical system

was costly and cumbersome. Additionally, for Raman enhancement to occur, the Raman shift must correspond to a wavelength that is capable of resonating in the microdroplet whispering galley mode.

The other common variant of CERS utilizes a more traditional high-Q optical cavity. A confocal cavity is the most commonly used optical cavity to provide Raman enhancement. Hill *et al.* first reported using a multipass cell for enhancing Raman scattering in 1977.[64] Here, the optical system consisted of two lenses and on-axis or off-axis retroreflecting mirror assemblies was employed. The system attained a focal volume of 1.1 mm X 0.3 mm X 0.3 mm, but exhibited significant Raman enhancement with an enhancement factor on the order of 20. Detection of flame gases was demonstrated with this system.

System similar to those used in cavity absorption spectroscopy have also been used for Raman enhancement. The optical system is identical as to the diagram shown in Fig. 2.1, but a CW laser is often used in place of the pulsed source. If a laser is frequency stabilized to a resonance frequency of the cavity, power buildup can occur by several orders of magnitude.[65] This technique has been termed power build-up cavity spectroscopy[66,67] in addition to CERS. The first practical demonstration of this idea was done by Taylor, Gluga and Penzhorn in 2001 where they stabilized a 1 W, 532 nm laser to a short, linear cavity by using electronic feedback. Raman signal was observed from hydrogen in a 90° collection geometry.[66] The enhancement factor here was determined to be on the order of 50, and detection of hydrogen at tens of parts-per-million required integration for 1 minute. Significant losses occurred when a Raman cell containing the gas to be analyzed was placed inside the cavity, thus limiting the detection limit.

In the work done by Ohara *et al.*, a power build-up cavity with finesse of 10,300 was demonstrated and used to detect nitrogen gas. To achieve this, a stable TEM_{00}

laser source was used. A cavity length of 40 mm was used with two concave mirrors with radius of curvature of 0.1 m. The laser was coupled into the cavity using a gradient refractive index (GRIN) lens and collection was again done in a 90° scattering geometry. With this setup, multiple longitudinal modes were coupled into the optical cavity, limiting the spectral bandwidth of the device to about 30 cm^{-1}.[67]

Salter *et al.*, demonstrated a similar cavity-enhanced Raman spectroscopy system that utilized a cw diode laser coupled into an external linear optical cavity composed of two highly reflective mirrors. In this case, the cavity mirrors were placed inside of a gas cell. This allowed for significantly higher sensitivity as compared to placing a gas cell inside of a optical cavity where losses from reflections off the cell surfaces result in a significant decrease in optical pathlength or power buildup inside the cavity. The laser is stabilized to the cavity by optical feedback from light exiting the cavity, and Raman light is collected in a forward scattering collection geometry. Faraday isolators are required to prevent back reflections from the gas cell BK7 windows from reflecting back into the laser diode. The cavity had a length of 35 cm, and the diameter of the beam inside the cavity was estimated to be 0.3 mm. This system was used to analyze several gases including H_2, atmosphere, CH_4, and benzene and detection sensitivities on the order of parts-per-million levels were reported. Integration times of 20 seconds to 100 seconds were used depending on the gas being analyzed, providing significant improvement as compared to other gas phase Raman spectroscopy techniques.

The final variant of CERS uses a very different configuration to the linear optical cavity. Here, two spherical mirrors form the cavity, as shown in Fig 2.2. This particular example shows a near-confocal system containing two focal points, O and O' as opposed to a confocal system where only one focal point exists. Li *et al.* constructed a near-confocal CERS system for multitrace-gas detection that was capable of greater than 50 reflections in the cavity.[68] A low-power, 200 mW 532-nm laser was

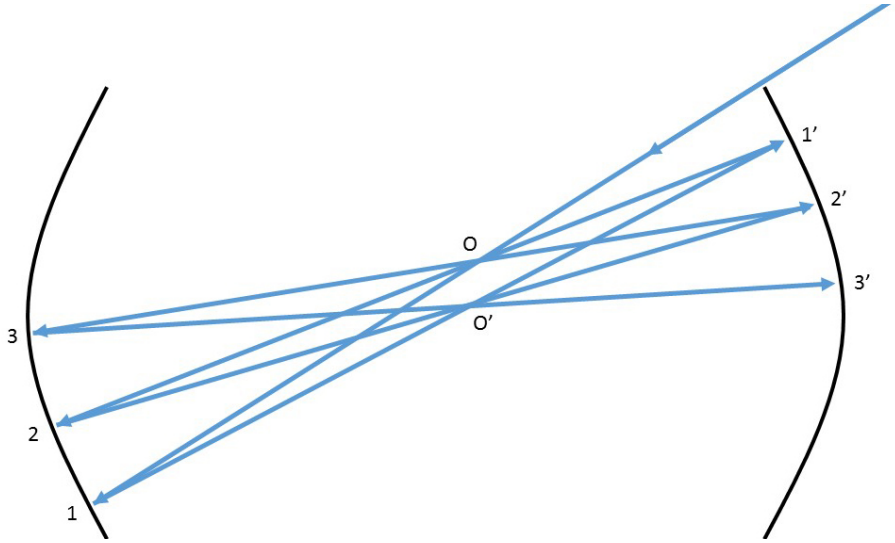

Figure 2.2: Schematic illustrating a near-confocal optical cavity that can be used for cavity enhanced Raman spectroscopy. Here, the two spherical mirrors are shown as the curves on the left and right, and O and O' are the two focal points. (Adapted from Li *et al.*[68])

used as the excitation source. With cavity mirrors that were only 99.8% reflective, a power of 9W was observed at the two focal spots. Detection in this system was done 90° relative to the plane of the spherical mirrors. A compound lens system along with filters to remove any of the excitation light couple light into a spectrometer for detection. To aid in collection of the Raman signal, a third spherical mirror with wide band reflectivity was placed opposite of the detector. This sytem was used to analyze mixtures of up to 8 gases including CO_2, C_2H_4, C_2H_2, CO, N_2, C_2H_6, CH_4, and H_2. Methane was detected at a concentration of 509 ppm with an integration time of 2 seconds and 200 averages.

For linear CERS system, Raman signal can either be collected at a 0° forward or 90° scattering geometry. With 0° forward scattering systems, the signal collected is that which leaks out of the front mirror of the optical cavity, and thus up to 50% of the total signal can be lost out the wrong mirror. With 90°geometries,

collection optics can be placed close to the optical cavity, but signal is collected from a much smaller sample volume. All of the CERS systems described rely on power buildup inside of the optical cavity to provide enhancement of spontaneous Raman scattering. The power buildup inside of the cavity stems from the high reflectivity of the mirrors, allowing for each photon to have an incredibly long effective pathlength inside. Sampling in a forward or backward scattering geometry allows for a larger sample volume, but at a potentially lower collection efficiency.

2.4 Summary

Cavity enhanced spectroscopy has found broad ranging applications in the realm of absorption spectroscopy. Due to the long interaction volume between the probe radiation and the sample of interest, small absorption values can easily be measured. This family of techniques is particularly useful for measuring the absorption of gas phase samples, where Rayleigh scattering adds only minimal error to the measurements. When combined with a tunable laser source, cavity enhanced Absorption spectroscopy can be used to provide information about the absorption cross-section over a range of frequencies. While this technique has found some applications in the analysis of exhaled breath, due to the limitations of just measuring an attenuation of the probe light, it is difficult to provide identification of the chemical composition of a mixture based purely on absorption.

Cavity enhanced Raman spectroscopy has been demonstrated with several highly reflective optical cavities. This technique is capable of identifying mixtures of gases without the need for tunable or expensive laser sources. Enhancement of Raman scattering occurs due to the buildup of the excitation laser radiation inside of the optical cavity. If a gas sample is placed inside the cavity, spectroscopy information about the constituents of the gas can be obtained. In order to generate the buildup of

power inside the cavity needed for Raman spectroscopy, careful alignment and mode matching can be required. Because of this, such systems are extremely susceptible to vibration and misalignment of the laser into the cavity, rendering use in the field more difficult. Additionally, some type of optical feedback is often needed to match the laser to the cavity mode. If multiple longitudinal modes are coupled into the cavity, the spectral bandwidth can suffer.

3. INTEGRATING CAVITIES*

3.1 Introduction

Until this point, all of the discussion regarding optical cavities has been about systems which use specular reflectors such as highly reflective metallic mirrors. These type of reflectors are characterized by the law of reflection which states that when a ray of light reflects off of a smooth surface, the reflected ray leaves that surface at only one angle such that the angle of incidence is equal to the angle of reflection. Linear two mirror optical cavities take advantage of this relationship to "trap" a ray of light between the two mirrors, causing it to bounce back and forth many times.

Conversely to this are a class of reflectors known as diffuse reflectors. Diffuse reflection occurs when a ray of light is reflected off from a surface that is rough at the microscopic level, resulting rays that reflect and diffuse in many different directions. This type of reflection is more common in the physical world with examples including clothing, paper, or even snow. All of these objects appear to have the same brightness, even when observed from different viewing angles due to the diffuse reflections that occur.

The following chapter will discuss the basic principles of diffuse reflectors along with examples commonly found in a research laboratory. Following this, the temporal dynamics of light interacting with a integrating cavity will be discussed. These principles of diffuse reflectors are key to providing the enhancement of the integrating cavity. The construction of the integrating cavities used in the work presented here will be outlined. Finally, integrating cavity ring down spectroscopy (ICRDS) and

*Portions of this section are reprinted with permission from "Measuring the absorption coefficient of biological materials using integrating cavity ring-down spectroscopy," M.T. Cone, J.D. Mason, E. Figueroa, B.H. Hokr, J.N. Bixler, C.C. Castellanos, G.D. Noojin, J.C. Wigle, B.A. Rockwell, V.V. Yakovlev, and E.S. Fry, 2015 *Optica*, **2,** 162-168 Copyright [2015] by the Optical Society of America.

it's biomedical applications will be discussed.

3.2 Diffuse Reflectors

A diffuse reflection is a material that causes an incident ray of light to reflect and diffuse, resulting in no relationship between the angle of incidence and angle of reflection. This is depicted in Fig. 3.1(a) where three incident rays are shown. Fig 3.1(b) shows rays of light reflecting off of a specular reflector. For both rays, the angle between the incident ray and the surface normal, θ_i is equal to the angle between the reflected ray and the surface normal, θ_r. Unlike specular reflection, diffuse reflection results in light leaving the surface at all angles. To understand why this occurs, it is important to look at the structure of a diffuse reflector. Due to the roughness of its surface, each individual ray can potentially meet a surface with a different orientation. Each surface acts as a partial reflector, where the reflections from this surface still obey the law of reflection. Thus, after the first reflection, multiple additional reflections are possible. This principle has been applied to studying biological tissue using the technique of diffuse reflectance spectroscopy.[69] In this case, when light propagates through tissue, it can undergo multiple scattering events. Some photons will scatter multiple times before it exits the tissue as reflected light.

Diffuse reflectors are characterized by two main properties: the reflectance and bidirectional reflectance distribution function (BRDF) of the material.[71] Reflectance is simply measured as the percentage of the incident radiant power that is reflected from the surface. The BRDF is the ratio of the radiance from a sample to the irradiance upon that sample for a given direction of incidence (θ_i, ϕ_i) and direction of scattering (θ_s, ϕ_s) and has units of inverse steradians. This can be expressed in terms of power as shown in equation 3.1, where P_i is the power incident on the sample, P_s is the power collected by a detector that can detect photons from the

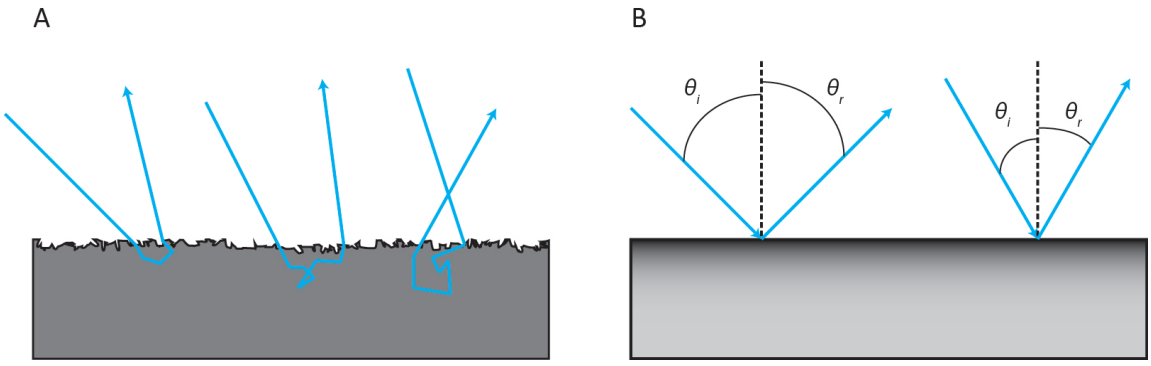

Figure 3.1: Diagram showing specular and diffuse reflection. (A) Rays reflecting from a rough, diffuse reflecting surface. (B) Rays reflecting off a smooth, specular reflecting surface. Adapted from Cone *et al.*[70]

solid angle $d\Omega$ where A is the area of the sample.[70]

$$BRDF \equiv \frac{radiance(\theta_s, \phi_s)}{irradiance} = \frac{P_s/A\cos(\theta_s)d\Omega}{P_i/A} = \frac{P_s}{P_i\cos(\theta_s)d\Omega} \tag{3.1}$$

Thus, this give a measurement of the intensity distribution for radiation after reflection from a diffuse reflector for any given angle of incidence. The ideal diffuse reflector, or Lambertian reflector, is one where light from any given direction is reflected in a way that the outgoing radiance is the same in all directions. This can be expressed as follows:

$$I = I_0 \cos\theta_s. \tag{3.2}$$

Thus, the BRDF for a Lambertian reflector is given by:

$$BRDF_{Lambertian} = \frac{P_s}{P_i\cos(\theta_s d)\Omega} = \frac{\rho P_i\cos(\theta_s)}{P_i\cos(\theta_s)d\Omega} = \frac{\rho}{d\Omega}, \tag{3.3}$$

where ρ is the reflectivity of the material. From equation 3.3, it can be seen that the BRDF for an ideal Lambertian reflector is constant.

Diffuse reflectors have found widespread use in optical laboratories. Perhaps the common device that utilizes a diffuse reflector is the integrating sphere and has been used in the field of optics since 1900.[72] Integrating spheres serve the purpose of spatially integrating radiant flux. This can be useful for generating a uniform illumination source, measuring the total radiative flux of a laser or lamp, and measuring optical properties of materials. The inverse adding-doubling method which incorporates an integrating sphere is the most common technique employed to measure the absorption and reduced scattering properties of biological tissue.[73–75]

The primary constituent of an integrating cavity is the diffuse reflecting material that cover the inner surface of the cavity. There are currently several high-quality diffuse reflectors that are commercially available for use in integrating cavities or other applications. Barium sulfate based powders, coatings, and paints, such as Eastman Kodak 6080, have been used as diffuse reflectors for over forty years.[76,77] Grum *et al.* values of absolute luminous reflectance of the barium sulfate-based powder and paint to be 99.5% and 99.2% respectively.

Other diffuse reflector variants based on barium sulfate or other proprietary materials have been developed more recently. Spectrareflect® is a specially formulated barium sulfate coating that offers a near perfect diffuse reflectance surface. The reflectivity is limited to 96-98% over the wavelength range of 400 to 1100 nm and depends on the thickness of the coating.[71] The reflectivity drops off significantly in the UV, where it is only 94% reflective at 250 nm. Duraflect® is another coating for use in hostile environments, with a reflectance value of $> 95\%$ for 350 to 1200 nm. Infragold® is an electrochemically plated, diffuse, gold-metalic coating with high reflectance in the infrared.[71]

Spectralon® is the current commercial product with the highest diffuse reflectance for use in the UV and visible wavelength range.[71] The material has a reflectance of

99.0-99.2% from 400 nm to 1500 nm, but falls off to only 95% at 250 nm. Spectralon® is a thermoplastic resin that can be machined into different shapes based on need. The material is also highly Lambertian from across the entire visible spectrum.

Similar to linear cavity enhanced spectroscopy techniques, where sensitivity in absorption measurements is dependent on mirror reflectivity, the reflectance of a diffuse reflecting material is critical to performance in any cavity enhanced spectroscopy technique. Because of this, E. S. Fry, J.A. Musser, M. T. Cone *et al.* developed a new diffuse reflecting material for use in integrating cavity spectroscopy.[70,78] The material is a fumed silica, or quartz powder based on a line of hydrophilic Aerosil products manufactured by Evonik Industries (Essen, Germany). Fumed silica is a synthetic amorphous silicon dioxide produced by burning silicon tetrachloride in an oxygen-hydrogen flame.[79] The average particle size for Aerosil EG50 is 20 to 40 nm, but due to the irregular shape, these particles form aggregates of partially fused particles which can also form larger agglomerates that can be on the order of several micrometers in size.[79]

Fumed silica powder was chosen for several reasons. First, quartz is known to have near zero absorption over a wide range of wavelengths spanning the UV to the visible. The idea for using this powder as a diffuse reflector came from the concept of light reflecting off a air-glass interface. The reflectivity at normal incidence for an uncoated air-glass interface, ρ, is approximately 0.04. For a stack of glass plates such that a small air gap exists between each, the total reflected light can be given by

$$R = \frac{i_r}{i_0} = \frac{2N\rho}{1 + (2N - 1)\rho}, \tag{3.4}$$

where N is the number of plates, i_r is the reflected light intensity, i_0 is the intensity of the incident light, and no back reflector is present.[70] This idea was originally

described by Stokes in 1860.[80] From equation 3.4, it can be seen that as N increases, R approaches 1. As reported by Cone *et al.*, the reflectivity of the stack reaches 0.999 as N approaches 12,000.[70] Thus, fumed silica, with it's nanometer sized particles, can be used as a substitute for quartz plates, allowing for high reflectivity for a relatively thin wall thickness due to the large number of air-glass interfaces. Cone *et al.* report the highest diffuse reflective values ever measured for this material, with a reflectivity of 0.99919 at 532 nm and 0.99686 at 266 nm, providing significant advantage over commercial products such as Spectralon® particularly in the UV. This material was also demonstrated to be a nearly Lamberitan diffuse reflector, making it the ideal material for integrating cavity-based spectroscopy.

3.3 Temporal Dynamics

Previously, we have discussed cavity ring-down spectroscopy, and diffuse reflectors with no mention of how an effective pathlength or reflectivity is calculated. In this section, the theory behind the temporal dynamics of integrating cavities will be discussed. The equations presented here for integrating cavities were originally derived in detail by Fry *et al.*[81] and are related to what is published in an technical guide for integrating spheres produced by Labsphere.[82]

To measure the reflectivity for an integrating cavity with reflectivity near 1, a cavity ring-down measurement can be used. To do this, a temporally short pulse of light is coupled into the integrating cavity via an multimode optical fiber. The decay in intensity, or "ring-down" of this pulse is then sampled using a second multimode optical fiber. For an empty cavity, the absolute reflectance of the cavity can be calculated based on the 1/e decay constant of the pulse of light, using

$$\tau = \frac{1}{-\ln \rho}(\frac{\bar{d}}{c}). \tag{3.5}$$

Here, τ is the decay constant, ρ is the cavity reflectivity, $\bar{d}$ is the average distance between reflections inside the cavity, and c is the speed of light.[78,81,83] The average distance between reflections for a cavity of arbitrary geometry can be expressed as

$$\bar{d} = 4\frac{V}{S}, \tag{3.6}$$

where V is the volume of the cavity and S is the surface area. The average number of reflections, n, inside a cavity of reflectivity, ρ, is simply given by

$$n = -\frac{1}{\ln \rho}. \tag{3.7}$$

The average pathlength inside a cavity, L, can be expressed as

$$L = n\bar{d} = -\frac{4}{\ln \rho}(\frac{V}{S}) \approx \frac{4V}{S(1-\rho)} \tag{3.8}$$

where the final approximation is valid in the case where ρ is close to unity.

Fig. 3.2 shows the experimentally measured cavity ring down for the cavity used for fluorescence enhancement.[84] To make this measurement, the frequency double output of a neodymium-doped yttrium aluminium garnet (Nd:YAG) laser that produced 10-ns full-width at half-maximum (FWHM) pulses of 532 nm light was launched into a multimode optical fiber. The tip of the fiber was placed into the integrating cavity. A second multimode optical fiber used to sample the decay in intensity of the input pulse was connected to a Hamamatsu 1P21 photomultiplier tube (PMT) with rise time of 2.2 ns. The data was collected using a Hewlett Packard Infinium oscilloscope. The ring-down signal was averaged over 1024 shots.

In order to determine the decay constant for the cavity, the output pulse is fitted to an exponential function. To account for the time of the input pulse, the measured

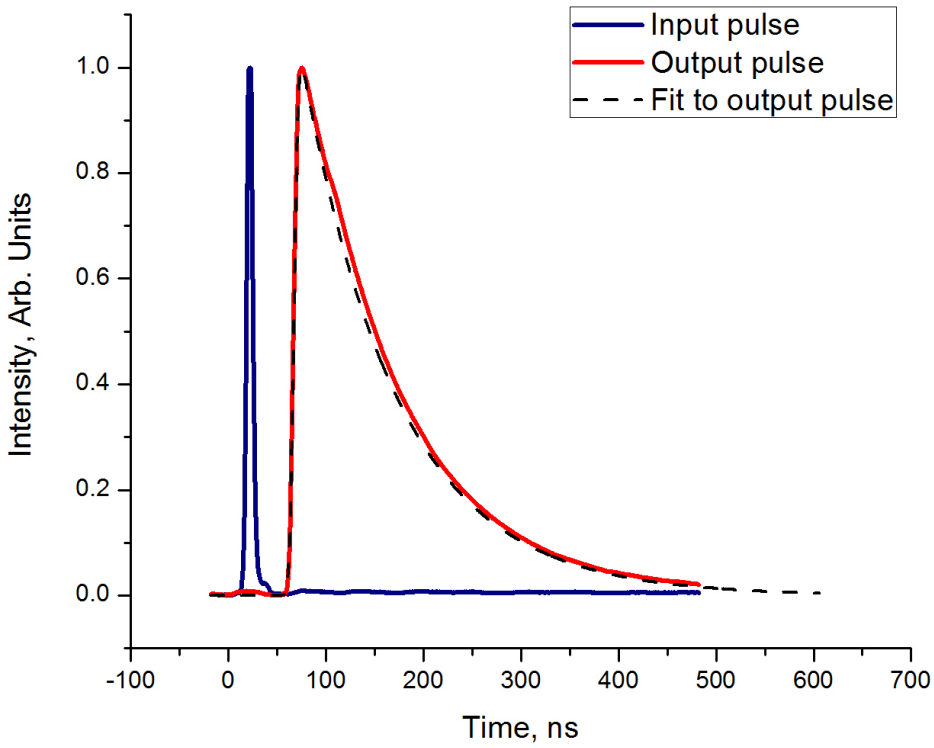

Figure 3.2: Ring-down measurement used to determine cavity reflectance. The blue trace depicts the input laser pulse, whereas the red trace shows the decay of radiation inside the cavity as measured by a PMT. The black dashed trace is a fit to the decay curve.

decay curve was fit using the convolution of a Gaussian, which represents the input pulse, and an exponential decay given by

$$Fit(t) = A\,exp\left(\frac{\omega^2}{2\tau^2} - \frac{t-t_s}{\tau}\right) \times \left(1 - erf\left(\frac{\omega^2 - \tau(t-t_s)}{\sqrt{2}\omega\tau}\right)\right), \tag{3.9}$$

where A is an amplitude fit coefficient, ω is the width of the Gaussian function, t_s is a time shift from $t = 0$ for the offset between the input and output pulse, erf(...) is the error function, and τ is the exponential decay constant. Another approach to measuring the decay constant is to simply fit only the tail of the measured ring-down, and has been shown to provide basically the same result. In this case, the fit simplifies to

$$Fit(t) = A \exp\left(\frac{t}{\tau}\right). \tag{3.10}$$

Once τ has been measured for a cavity of known geometry, the reflectivity ρ and average pathlength L can be calculated. For the ring-down fit shown in Fig. 3.2, the decay constant was measured to be 98.14 ns. The cavity was a right-circular cylinder with diameter and height equal to 50.8 mm. Using equation 3.6 and equation 3.5, the reflectivity was determined to be 0.9988 at 532 nm. From equation 3.8, this corresponds to a pathlength of ≈ 30 m for the sample region inside the cavity.

The properties of the integrating cavities discussed above are critical for enhancement in integrating cavity-based spectroscopy. Similar to traditional cavity-based absorption spectroscopy techniques, the long effective pathlength allows light to have multiple passes through a sample of interest. For absorption spectroscopy, this allows more accurate measurements of samples with very low absorption coefficients, such as water in the UV.[85] The other property that is critical for enhancement is the Lambertian nature of the cavity walls. This means that regardless of where a sample

is inside the integrating cavity, it will be probed by the input radiation. Additionally, the entire volume of the cavity can be probed simultaneously. Thus, a larger sample volume can be interrogated as compared to traditional spectroscopy, where signal generation is limited to the focal volume of the excitation optics. Furthermore, since the cavity is highly reflective over a broad range of wavelengths, the emitted signal will also reflect inside the cavity. Thus, a portion of the signal generated from anywhere inside the cavity can be collected.

All cavities used for work in this dissertation were made from the Aerosil EG50 powder developed by the laboratory of Prof E. S. Fry at Texas A&M University. This material was chosen due to the fact that it posses the highest values of diffuse reflectivity ever recorded. This is critical for the total pathlength, where even a change from 0.999 to 0.99 results in a 10% change in pathlength for light inside the cavity. This material also maintains its high reflectivity into the UV, which is critical for both fluorescence and Raman spectroscopy. Many biological samples possess natural endogenous fluorescence when excited with ultraviolet light, and Raman scattering cross-sections scale with λ^4.

3.4 Integrating Cavity Design and Construction

This next section will detail the construction process for the integrating cavities used in these experiments. All cavities used in the experiments presented here were constructed by the laboratory of Prof. Edward S. Fry. As previously mentioned, the material that was selected is Aerosil EG50 manufactured by Evonik Industries is the material used due to its high reflectivity. This material has a high specific surface area (m^2/g, and is highly hydrophilic. Since the number of air-glass interfaces are critical for a high reflexivity, water absorption can result in a decrease in reflectivity if it index matches these gaps. The procedure to prepare the powder has been described

in detail by Cone *et al.* and Musser *et al.* and is briefly described here.[70,78,83]

First, to minimize the amount of water in the material, the powder is baked in a Fischer Scientific Isotemp Vaccuum Oven that is coupled to a liquid nitrogen sorption pump at a temperature of 280 °C. The oven is filled with argon while the material cools. Following this, the baked powder is packed using a hydrolic press into a semi-solid material. The powder is packed between 30 to 1000 psi, as this range has been demonstrated to show the lowest transmission.[78] The quartz powder used is intrinsically a very hard material, and can build up significant static charge when being packed. These features lead to the material "biting" into the packing mold or jig while a cavity is constructed. To minimize this, the powder was often pre-packed to a lower pressure.

Cavities were constructed using two separate methods. First, attempts were made to produce a cavity that had an internal quartz cell. This cell would allow for control of the gas or liquid placed inside of the integrating cavity. Due to the fragile nature of the inner quartz pieces, cavities made in this manor had to be hand pressed using a custom made mold. This technique resulted in a significantly lower cavity reflectivity than compared to packing with a hydrolic press. An example of a cavity packed with an internal quartz cells with 532 nm laser light coupled in can be seen in Fig 3.3.

Due to the poorer wall quality for cavities packed with internal quartz pieces, the majority of the cavities used for the experiments presented here where packed using an alternate technique. Here, the cavity is made in halves. Identical cylindrical pieces of quartz tubing ar used as the mold for each half. The powder is then packed in each half using the hydraulic press allowing for higher pressure than is possible with hand packing. The semi-solid nature of the compressed powder makes it possible to machine the cavity halves using standard machining procedures such as turning

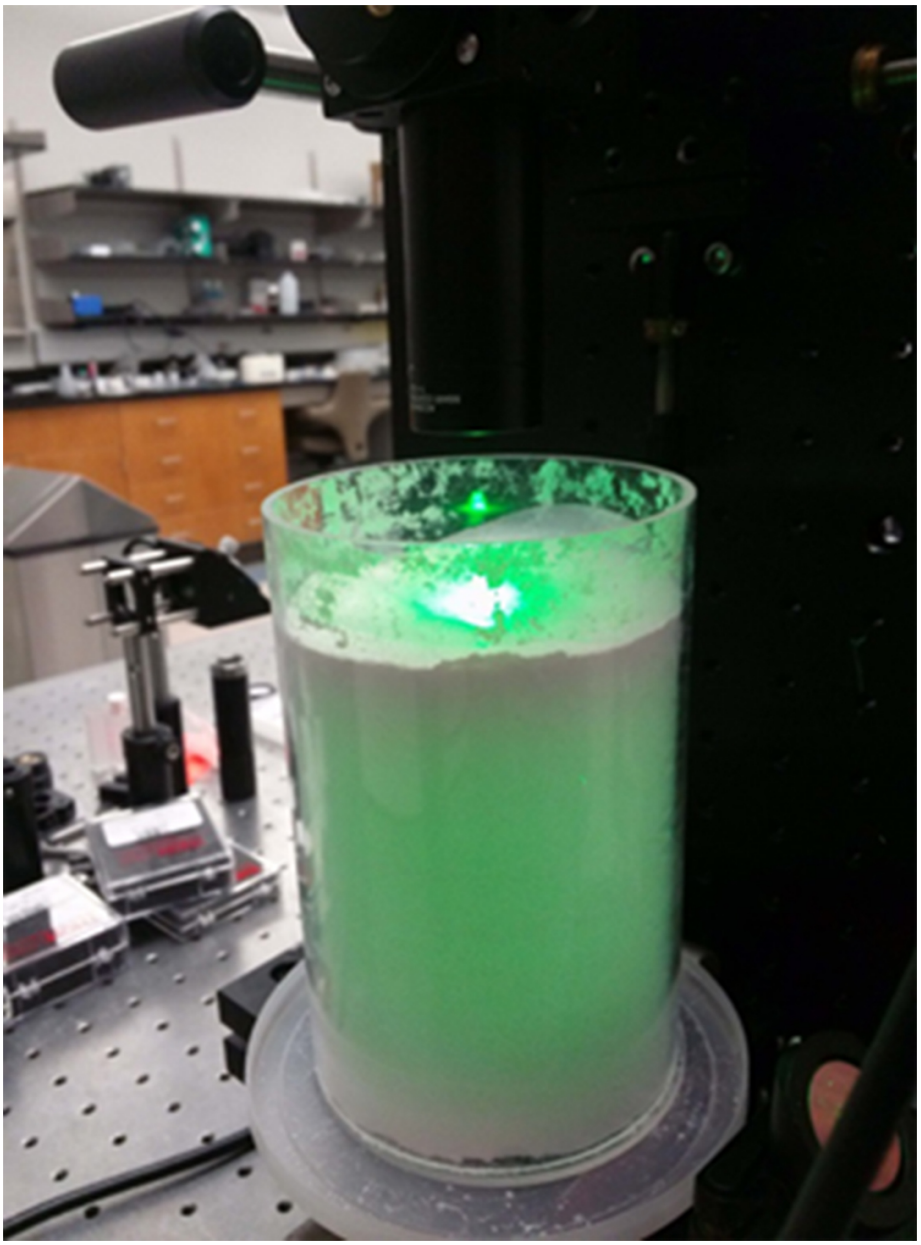

Figure 3.3: Integrating cavity packed with an internal quartz cell. The outer mold for this cavity is a single cylindrical piece of quartz.

on a lathe or boring with a mill. Since $\bar{d}$ can be solved for any geometry of cavity, the inner bore of the cavity was chosen to be a right circular cylinder. Due to the brittleness of the packed powder, a wall thickness of 3/4 to 1 inches was used for all cavities. While thinner walls are theoretically fine, this thickness was kept for the purposes of ease while machining out material. A typical diameter and height of 50.8 mm was used. This was selected due to the availability of quartz tubing at this size, and limitations on outer diameter based on the hydraulic press and oven available.

Finally, in order to couple light into and out of the cavity, a small through hole was drilled into one of the cavity halves. This hole had a diameter of 2 mm to limit losses to reflectivity. Any opening placed in the cavity walls will decreased the reflectivity based on the ratio of surface area removed to total surface area. Thus, a hole of this size will decrease the reflectivity slight, but will not greatly impact this measurement. This is why the ring-down trace and corresponding reflectivity shown in Fig. 3.2 is slightly lower than the values previously reported by Cone and Musser. Fig 3.4 shows a rendering of the cavity halves sitting next to each other on a flat surface. These pieces have an external diameter of 4 inches, a wall thickness of 2 inches, and a depth of 1 inch. The small through hole drilled in the piece on the right is used for coupling light into the cavity.

For integrating cavity-based spectroscopy, the cavity halves are placed on top of each other. A cross-section of this is shown in Fig. 3.5. It should be noted that the gap that appears in this rendering was intentionally left to illustrate the two halves of the integrating cavity.

Since the fumed silica powder is quite hydrophilic, any liquid sample that will be analyzed inside the cavity must be contained. To do this, quartz crucibles (Technical Glass Products, USA) were used as a sample holder. High purity quartz was selected for its minimal absorption in the UV and visible, and crucible was specifically chosen

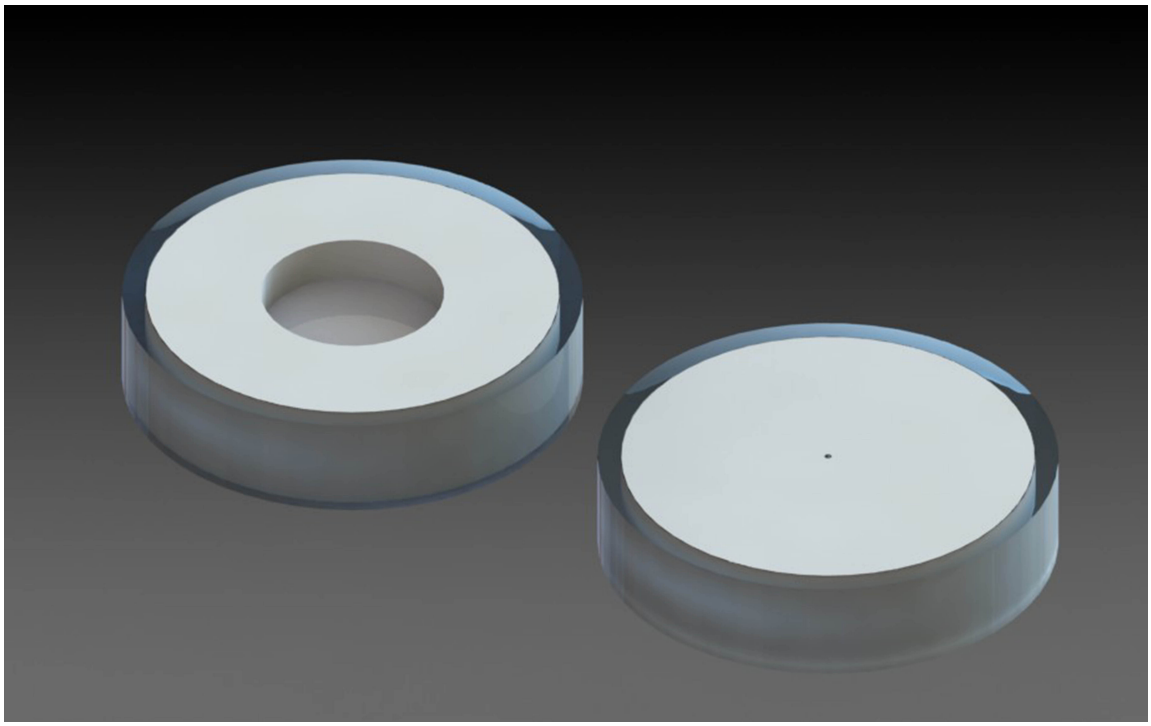

Figure 3.4: A rendering of two halves of a integrating cavity made from packing fumed silica powder with a hydraulic press. The cavity bore is created by removing powder from the solid disk with a mill. A small through hole can be observed in one of the pieces used for coupling light into and out of the cavity.

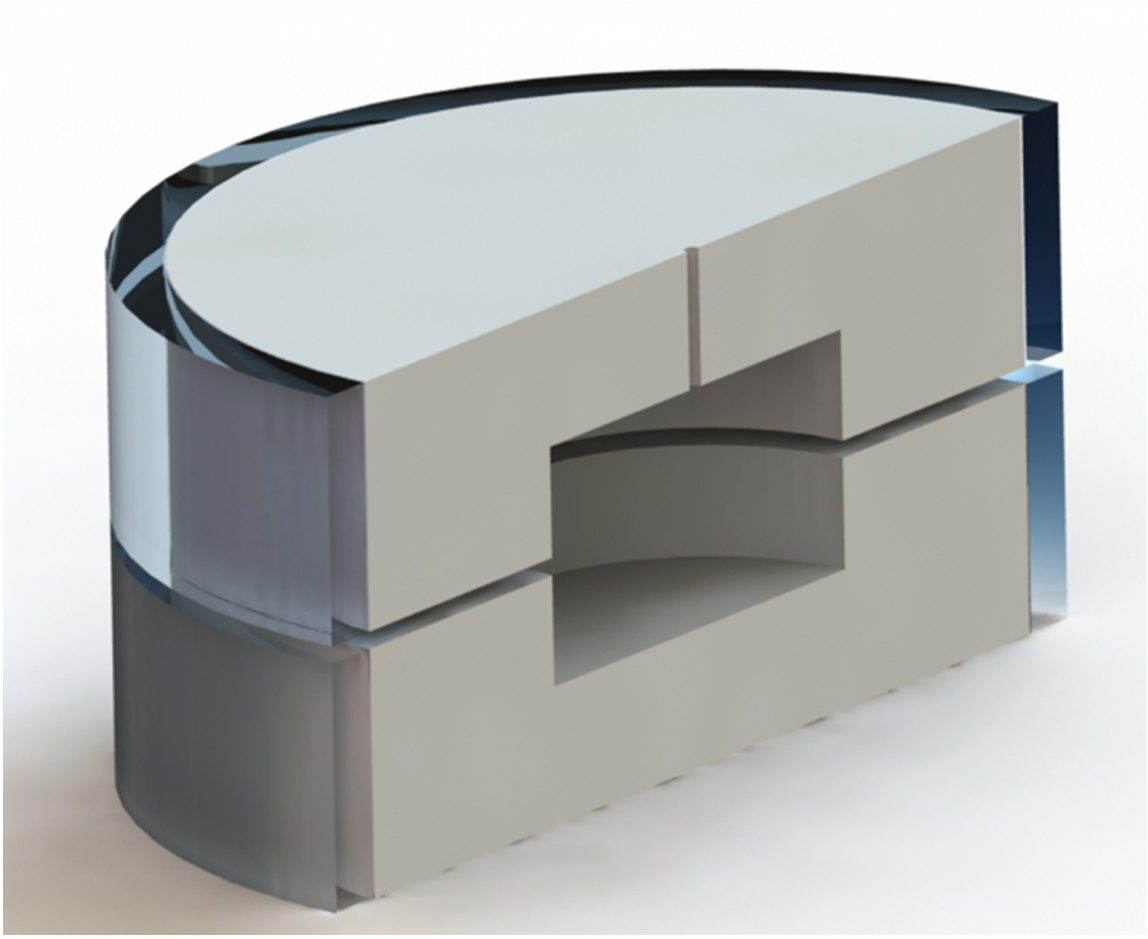

Figure 3.5: A cross-section of an integrating cavity made from two cylinders that are placed on top of each other. The slice is directly through the center of the cavity. The through hole for coupling light into and out of the cavity can be seen. It should be noted that the gap that appears in this rendering was intentionally left to illustrate the two halves of the integrating cavity.

due to its flat bottom and large capacity relative to other options. Stability of the sample holder was key as the cavity must be removed from the optical setup so that the sample could be changed and if liquid came in contact with the walls, this could add background to the measured spectrum rendering the cavity useless.

3.5 Integrating Cavity Ring Down Spectroscopy

Finally, in this chapter we will discuss a novel technique to accurately measure the absorption coefficients of biological material termed integrating cavity ring-down spectroscopy (ICRDS). As previously mentioned in section 2.2, cavity ring-down spectroscopy (CRDS) has been shown to be a powerful technique at measuring the absorption coefficient of weakly absorbing material. Here, a linear optical cavity is employed that uses highly reflective mirrors. Due to the high reflectivity, light coupled into the cavity passes through the sample multiple times, allowing for accurate measures of the absorption of the material inside the cavity. While this technique is quite robust for measuring the absorption of gases and other samples with no scattering, it is incapable of distinguishing the effects of scattering from the obtained result. Thus, if the scattering coefficient is on the order of the absorption coefficient of the material being measured, CRDS provides a measure of the attenuation (or extinction) coefficient. Other methods for determining the scattering must be used in order to attempt to calculate an accurate absorption coefficient.

This is particularly a problem for biological material, where scattering dominates absorption across most wavelengths.[86] Because of this, traditional techniques to measure absorption, such as the use of a spectrophotometer, cannot be applied to biological tissue. Instead, methods such as the inverse adding-doubling technique that utilizes an integrating sphere was developed.[73,87–89] While this method has been widely adopted for use in measuring the optical properties of tissue, it suffers

in several regards. First, the inverse adding-doubling solution assumes a unique combination of the albedo, the optical depth, and the anisotropy can be determined from the measured transmission and reflection measurements, which is not always the case. If a sample is too thick, the technique can fail. Second, the method requires the user to input a set of optical properties that are then iterated upon until a solution is obtained. If the input parameters differ greatly from the real parameters being solved for, the method could converge to a local minimum as opposed to the global minimum. Finally, if there is any error in the measured reflectance and transmission, this errors will compound itself in the calculation of absorption and reduced scattering coefficients.

Because of these limitations, there is the need for a more robust technique for measuring the absorption coefficients of biological material. Accurate knowledge of these values is critical for biomedical imaging techniques, modeling of light transport in tissue, and laser-based procedures such as refractive correction surgery.[90,91] In traditional CRDS, scattering causes light to escape from the cavity, but in ICRDS where the sample is completely surrounded by the highly reflective material, scattering from the sample does not impact the measured ring-down signal. Additionally, traditionally CRDS requires that the input source be mode matched to the cavity, limiting the range of wavelengths absorption measurements can be taken from. In ICRDS, the diffuse nature of the light inside an integrating cavity causes there to be no preferred cavity modes, allowing for absorption measurements to be made as long as the wall is sufficiently reflective.

To demonstrate this technique, the absorption coefficients of retinal pigmented epithelium (RPE) cells was measured. Recall that for an empty cavity, the decay

constant τ for the exponential decay inside of an integrating cavity is given by

$$\tau = \frac{-1}{\ln \rho}\left(\frac{\bar{d}}{c} + \delta t\right). \tag{3.11}$$

Previously, the δt term was neglected, but corresponds to the average "wall time" for each reflection as was depicted in Fig. 3.1. Since biological material such as RPE cells must be kept in some buffer solution (phosphate buffered saline) to stay viable, the samples used in these experiments contained a volume of cells and buffer. Because of this, with a sample inside the cavity, equation 3.11 becomes

$$\tau_{RPE} = \frac{1}{-\ln \rho + (\alpha_{PBS} + \alpha_{RPE})\bar{d}_s}\left(\frac{\bar{d}}{c} + \frac{\bar{d}_s}{c_s} + \delta t\right). \tag{3.12}$$

where τ_{RPE} is the absorption coefficient for the RPE cells, $\bar{d}_s$ is the average distance between reflections in the sample, c_s is the speed of light in the sample, $\bar{d}$ is the average distance between reflections excluding those that occur in the sample, α_{PBS} and αRPE are the absorption coefficients for the PBS buffer and the RPE cells respectively.

In order to be able to determine a quantitative absorption coefficient value from the measured decay times, the number of cells inside the cavity must be known along with the decay time of a known absorber. This allows for an absolute measure of an absorption coefficient. Because of this, the ring-down times for a calibrated dye solution must also be determined. Equation 3.12 becomes

$$\tau_D = \frac{1}{-\ln \rho + (\alpha_{pw} + \alpha_D)\bar{d}_s}\left(\frac{\bar{d}}{c} + \frac{\bar{d}_s}{c_{pw}} + \delta t\right), \tag{3.13}$$

where c_{pw} is the speed of light in pure water, α_{pw} and α_D are the absorption coefficients for pure water and the dye, respectively. Thus, if the decay times for samples

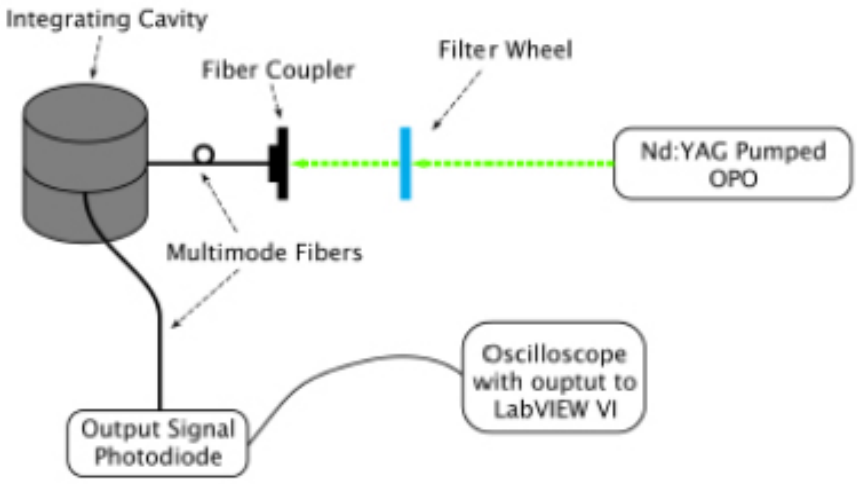

Figure 3.6: Diagram showing the experimental setup for ICRDS absorption measurements. Printed with permission from the Optical Society of America.[83]

with equal volume of RPE cells, the PBS buffer, and two dye solutions are measured, equations 3.12 and 3.13 can be used to derive an expression for the absorption coefficient of the RPE cells.[70] This expression is given by

$$\alpha_{RPE} = \frac{\tau_{PRE}^{-1} - -\tau_{PBS}^{-1}}{\tau_{D1}^{-1} - -\tau_{D2}^{-1}}(\alpha_{D1} - \alpha_{D2}), \tag{3.14}$$

where $D1$ and $D2$ refer to the two concentrations of calibrated dye.

Fig. 3.6 showns a diagram of the optical setup used to measure the absorption coefficients. In order to experimentally measure these values, a Quanta Ray Pro290 Nd:YAG-pumped VersaScan 355 midband OPO that produced 6 ns pulses and was tunable over a range of 412 - 2550 nm was used as the laser source. Light from the OPO was launched into a multimode fiber that was used to couple the input pulse into the integrating cavity. A neutral density filter wheel was used to attenuate the input pulse to prevent detector saturation. Another multimode fiber connected to a

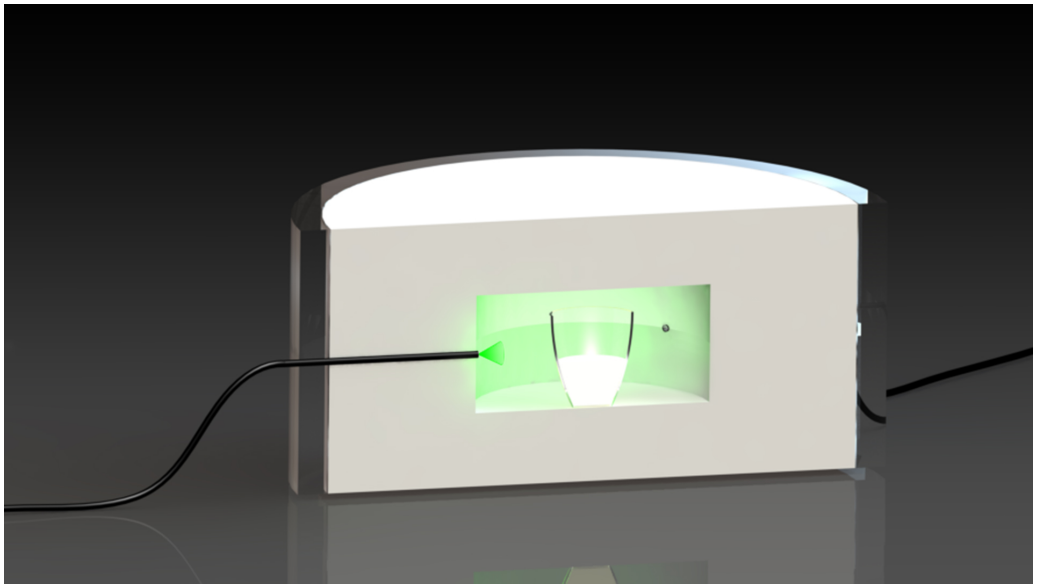

Figure 3.7: Diagram showing a cross-section of the integrating cavity with the quartz crucible sample container. a pulse of green laser light is being delivered to the cavity via a multimode fiber on the left side of the image. The multimode fiber on the right side of the image samples the decay in this signal. Printed with permission from the Optical Society of America.[83]

Thorlabs DET 100 photodiode sampled the ring-down signal inside the cavity. An oscilloscope and LabVIEW VI were used to average 50 shots and record the data. Fig. 3.7 shows a rendering of a cross-section of the integrating cavity with a sample inside. Here, a pulse of green laser light is being delivered to the cavity via an optical fiber on the left side of the image. The optical fiber on the right side of the image samples the decay in this signal. The tip of this fiber can be seen in the cavity wall to the right of the crucible with the sample solution.

Human telomerase reverse transcriptase transformed human retinal pigmented epithelium cells(hTERT-RPE) cells were used for demonstrate a proof of principle absorption coefficient measurements. Cells were purchased from the American Type Culture Collection, and a detailed description of the methods used to culture the

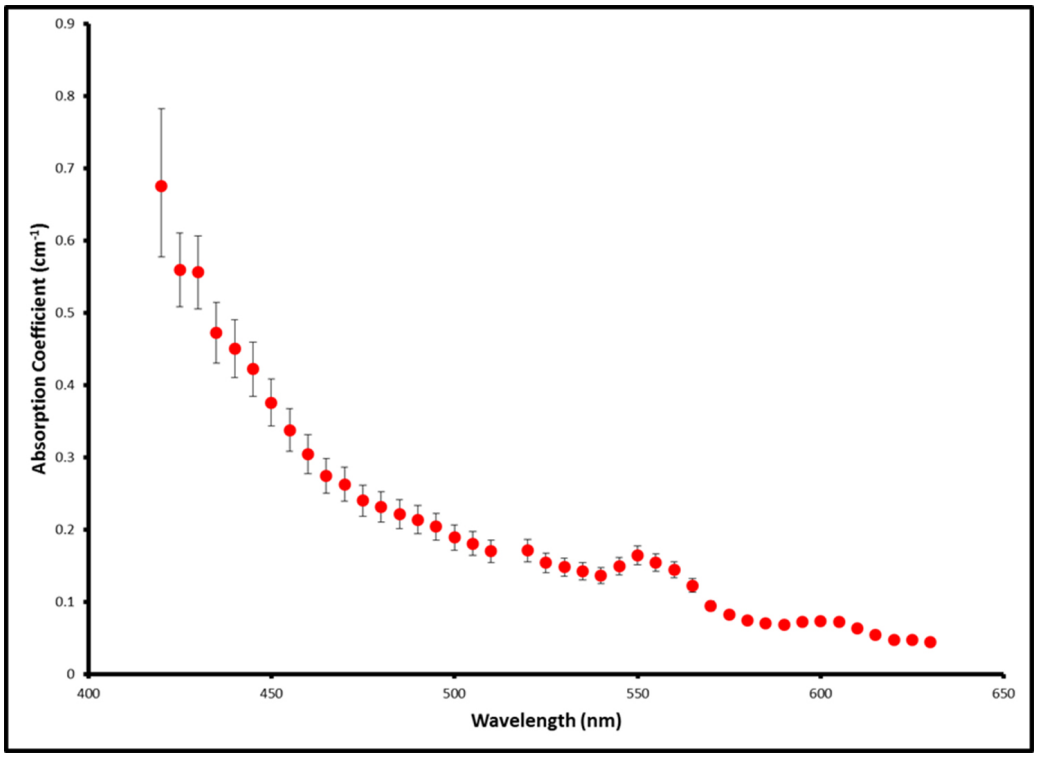

Figure 3.8: ICRDS measurements of the absorption coefficients from 420 to 630 nm for a sample containing 60 million RPE cells. The cells were suspended in PBS solution witha total volume of cells and buffer equal to 3 mL. The contribution to the absorption due to the buffer has been subtracted out. Printed with permission from the Optical Society of America.[83]

cells was previously published by Denton *et at.*[92] Cell culturing and preparation for absorption coefficient measurements was done by Dr. Jeffrey Wigle and his laboratory that is part of the 711$^{\text{th}}$ Human Performance Wing, RHDO.

Fig. 3.8 shows the results of measuring the absorption coefficients for RPE cells suspended in a PBS buffer. The total number of cells inside the crucible was approximately 60 million. The contribution from the buffer to the absorption coefficients has been subtracted out and detailed above. The absorption coefficient at 515 nm was excluded due to low output signal from the OPO. The error bars shown correspond to the combination of error from the uncertainty in decay constants, the

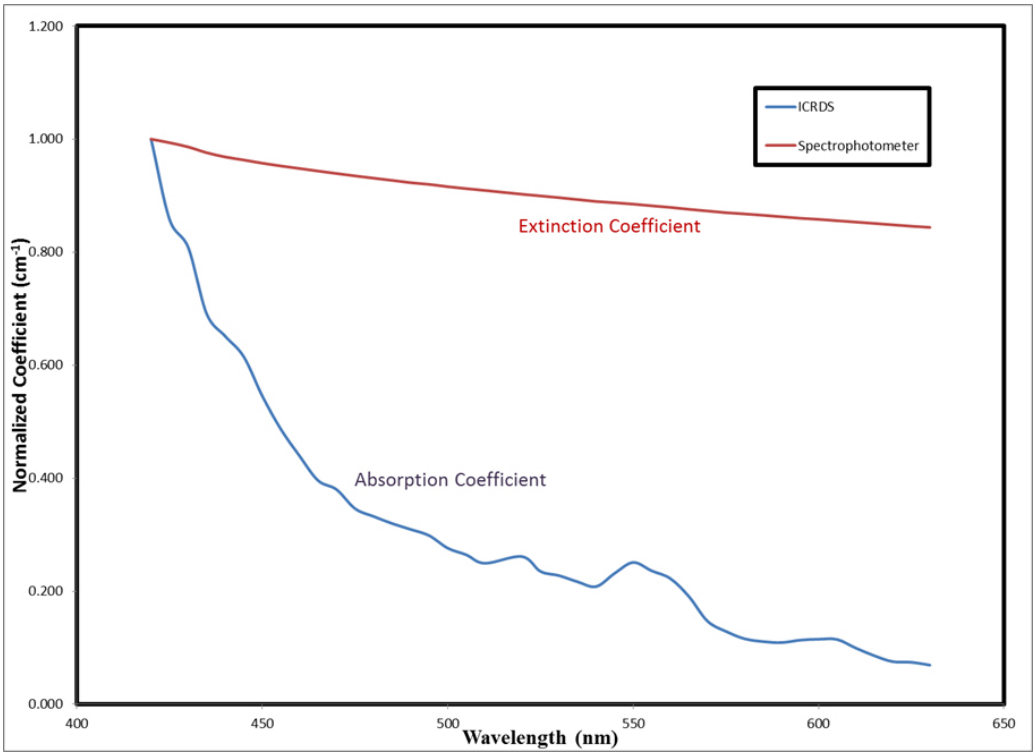

Figure 3.9: Comparison of ICRDS and spectrophotometer measurements for the absorption coefficient of RPE cells. The left vertical scale corresponds to the ICRDS data, while the right vertical scale corresponds to the spectrophotometer data. Printed with permission from the Optical Society of America.[83]

accuracy in determining the concentration of calibrated dye solutions used, and the accuracy of the spectrophotometer used to measure the absorption coefficients of the calibrated dye. An Agilent Carry 6000i spectrophotometer was used to measured the absorption coefficients of a more highly concentrated dye solution, and this system lists an accuracy of 0.0003 absorbance units.

Fig. 3.9 shows a comparison of the absorption coefficients obtained for the same sample using ICRDS and a commercial spectrophotometer. The spectrophotometer data gives coefficients that are on the order of 100 times larger than those values measured by ICRDS. This is because scattering contributes to the attenuation of signal

measured by the spectrophotometer. Simple experiments of adding microspheres to a solution of buffer or calibrated dye show that the decay constants measured by ICRDS are not effected by the addition of scattering to a sample.

While the OPO has a tuning range from 412 to 2550 nm, the initial data set was limited to the range shown above for several reasons. First, the absorbance of the Irgalan Black calibrated dye drops off considerably above 650 nm, and water absorption begins to dominate the absorption measured in this range. Since cells are predominately composed of water, the lack of a calibrated absorber in this range rendered the ring-down times measured for a RPE buffer solution useless. This could be overcome by using a second set of calibrated dye solutions that exhibit higher absorbance above 650 nm. Second, the reflectivity of the integrating cavity begins to fall off with longer wavelengths. A reflectivity of 0.995 was measured at 1064 nm, compared to the reflectivity of 0.9992 at 532 nm. Thus, the technique is less sensitivity to change in absorption for longer wavelengths. Since water absorption increases with longer wavelengths, ICRDS should still be capable of measuring accurate absorption coefficients for biological material beyond 650 nm, as long as careful consideration is given to the selection of calibrating dyes. Since the powder maintains high reflectivity into the UV, it is possible this technique could be used to obtain absorption coefficients for shorter wavelengths as well. Care would have to be taken to ensure any fluorescence generated from the sample caused by the UV excitation would not impact the ring-down time measured.

We have shown that ICRDS is a powerful spectroscopy technique that can provide accurate measures of absorption coefficients, even for samples that are highly scattering. This technique is ideally suited for weakly absorbing materials, where measurements via other techniques cannot provide accurate results. It should also be noted that if the material placed inside the cavity is too highly scattering, ICRDS

will not obtain an accurate result. This is because it is possible that the entire volume of the sample will not be exposed to the input light as the light would be unable to penetrate deep into the sample. Thus ICRDS would not be measuring absorption for the number of cells placed inside the cavity, but only some volume fraction. While these experiments focused on measuring the absorption coefficients of cells, this technique could easily be applied to measuring the absorption of other samples such as thinly sliced bulk tissue, sub-cellular constituents, or aerosolized particles.

4. SPONTANEOUS RAMAN ENHANCEMENT

4.1 Introduction

Raman scattering is the inelastic scattering of a photon from a molecule. The frequency of the scattered photon is determined by the frequency of a vibrational level of the molecule. The frequency shift of the Raman light with respect to the pump light is unique to the molecule, making Raman spectroscopy a valuable tool for molecular and structural identification.[93] The energy level diagram for Raman scattering was shown in Fig. 1.2 and discussed in more detail in Chapter 1. While Raman scattering can provide detailed information about a sample, spontaneous Raman scattering, the linear effect, is incredibly weak when compared to Rayleigh scattering. Typical Raman cross-sections are on the order of 10^6 to 10^7 smaller than their Rayleigh counterpart, causing Rayleigh scattering to be the dominate effect. Because of this, researchers have worked to develop novel techniques to enhance the generation of Raman scattered photons in order to open the door for new applications for this type of spectroscopy. Several nonlinear methods have been developed, and were briefly discussed in Chapter 1. While providing significant enhancement, these techniques have limitations such as the cost of the laser systems or repeatability of signal generation that have limited their use.

In this Chapter, we will demonstrate a novel method for enhancement of spontaneous Raman scattering using the elastic scattering from the walls of an integrating cavity. The highly reflective nature of the cavity walls causes pump photons to scatter multiple times throughout the cavity. Provided that the scattering medium exhibits very low absorption in the spectral range of interest, a large enhancement factor can be attained in a simple and relatively inexpensive setting. To demonstrate

the enhancement capabilities of an integrating cavity, we will first measure Raman spectra of atmosphere. Following this, we will demonstrate the ability to detect traces of environmental toxins placed inside the cavity using Raman spectroscopy.

4.2 Integrating Cavity Enhancement Theory

Enhancement of linear optical processes inside an integrating cavity occurs for the similar reasons as to where the enhancement of a linear optical cavity comes from. For techniques such as cavity enhanced absorption spectroscopy, the highly reflective cavity mirrors allow for photons to have multiple passes through a sample, resulting in increased attenuation of the reflected light over time. By sampling the decay in the intensity of light that escapes from the cavity, an absorption coefficient be calculated knowing the average pathlength each photon travels through the sample. For these techniques, cavity gain can be expressed by several functions. The gain of cavities with two highly reflective mirrors can be expressed as

$$G = \frac{R}{1-R}, \tag{4.1}$$

where G is the cavity gain and R is the mirror reflectivity. For mirrors with reflectivity greater than 99.99%, this value can by on the order of 10^4 or greater for more highly reflective mirrors. Additionally, the gain can simply be related to the cavity finesse or to the quality factor (Q-factor). For an optical resonator, the Q-factor is given by

$$Q = \frac{2\pi\ stored\ energy}{energy\ lost\ per\ cycle} = \frac{2\pi v_0 T_{rt}}{l}, \tag{4.2}$$

where v_0 is the optical frequency, T_{rt} is the round-trip time, and l is the fractional power loss per round trip assuming $l \ll 1$. This is the same as saying that $(1-R) \ll 1$.

Traditional cavity enhanced Raman spectroscopy allow for gain by three main

mechanisms when compared to Raman signal generated using a microscope system. First, the volume probed can be significantly greater than the volume probed using traditional optics such as a microscope objective. For instance, in the cavity enhanced Raman system reported by Salter *et al.*, they estimated that the laser light localized to a 0.3 mm diameter beam that propagated through a cavity 35 cm long.[94] This allows for a sampling volume of approximately 24 mm^3. Enhancement also stems from the simple fact that any photon coupled into the cavity will undergo n number of bounces where n is given by

$$n = -\frac{1}{\ln \rho}. \tag{4.3}$$

Here, ρ is the mirror reflectivity. The increased number of passes through a sample allows for increases signal generation compared to a single pass system.

Finally, since the laser frequency has to be matched to a cavity mode, power build up by three orders of magnitude inside the cavity can be seen.[94] Since the spontaneous Raman scattering generated is proportional to input power, this power increase can result in three orders of magnitude enhancement. It should be noted that these gain mechanisms only are viable when Rayleigh scattering and absorption inside the cavity are negligible. Both of these effects will decrease the losses per round trip, effectively resulting in a lower reflectivity.

The gain mechanisms in integrating cavity enhanced spectroscopy are very similar to those listed above for a traditional linear cavity, but with some advantages and disadvantages of its own. Fig. 4.1 shows a cross-section slice of a generic integrating cavity with a single entry and exit port. Two rays representative of a focused cone of light are shown entering the cavity. Due to the diffuse reflective nature of the cavity walls, the light scatters off the wall such that the outgoing radiance is the same in all directions. The scattered, or reflected rays, drawn in this Fig. 4.1 are intended to

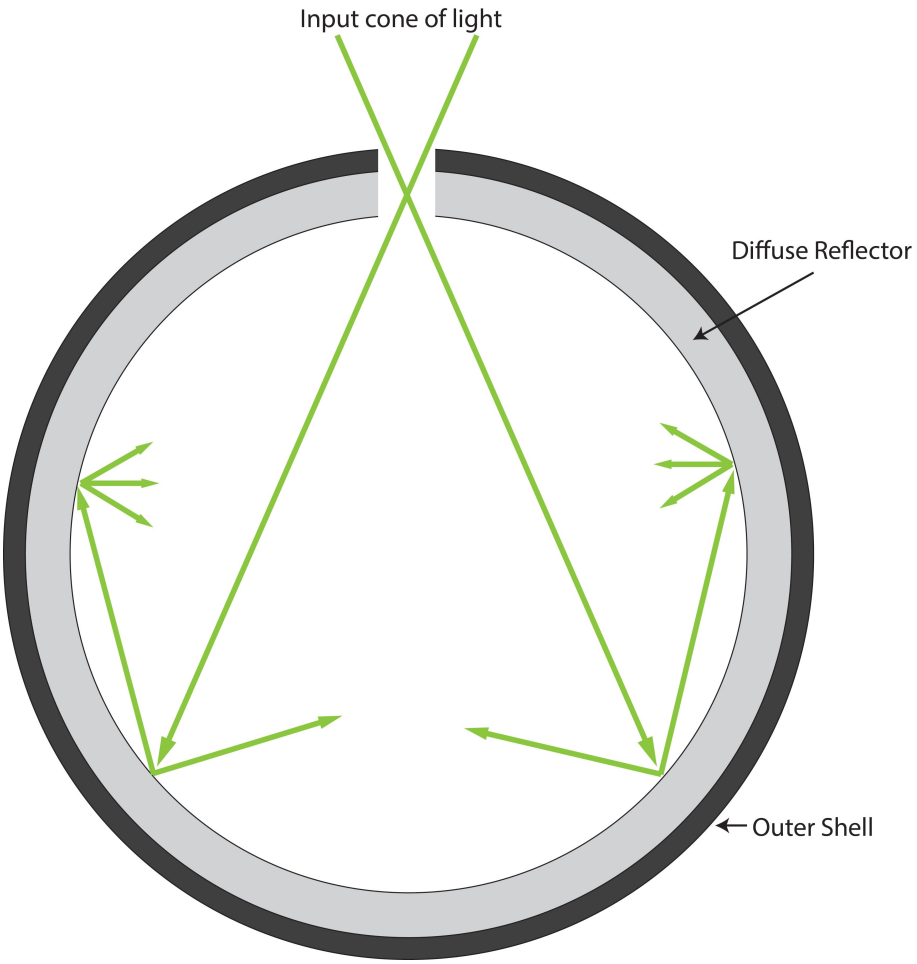

Figure 4.1: Cross section of a generic integrating cavity.

show this. If the diffuse reflector is nearly Lambertian, this creates an isotropic field inside of the integrating cavity. Because light fills the entire volume of the integrating cavity, Raman signal can be generated from molecules located anywhere within the cavity. Thus, for a right-circular cylinder of with diameter and height equal to 50.8 mm, a sample volume of 103,000 mm^3 can be achieved. This offers a factor of 10^3 larger sample volume compared to the linear optical cavity developed by Salter *et al.*

Another advantage to an integrating cavity is that scattering of the excitation light by the sample inside the cavity does not effect the enhancement provided. This was demonstrated by Cone *et al.* by measuring the ring-down times of a cavity with a sample of pure water and a sample with water and silica microspheres.[70] The addition of scattering to the cavity did not change the ring-down time, and thus did not decrease the pathlength inside.

Since there are no preferential cavity modes inside of an diffuse reflecting cavity, the excitation source does not have to be mode matched to the cavity. This allows for selecting any excitation wavelength, so long as the cavity is reflective at that frequency. Since Raman cross-sections scale as a function of λ^4, and the fumed silica powder is still highly reflective for blue shifted wavelengths, Raman excitation can be done at a more efficient wavelength.

Finally, linear cavities require careful alignment to ensure the laser beam does not escape the cavity due to changes in the angle of propagation following each specular reflection from the cavity mirrors. On the other hand, an integrating cavity simply requires light to be coupled into it. Provided that the entrance aperture is sufficiently large (on the order of 1-2 mm), efficient coupling into the cavity is relatively easy to achieve.

4.3 Raman Spectroscopy of Atmosphere

Gas Chromatography coupled with mass spectrometry remains the gold standard for gas phase analysis. However, vibrational spectroscopic techniques such as Raman spectroscopy have great potential for quantitative analysis of gases. But generating Raman signal from a gas sample can be difficult due to how the incredibly weak the effect is. For most gases, Rayleigh scattering is quite weak, and Raman cross-sections are on the order of 10^6 smaller resulting in even less signal. Because of this, for Raman spectroscopy of gas samples to be practical, significant enhancement of the signal is needed.

Cavity enhanced Raman spectroscopy has previously been demonstrated using a linear optical cavity consisting of two highly reflective mirrors. If a laser source is mode matched to the cavity, significant power buildup can occur inside of the cavity, allowing for increased generation of Raman signal from a relatively low power laser source. Depending on the number of modes that can propagate inside of the cavity, the spectral resolution of these system can be quite limited, with reports on the order of $30cm^{-1}$. Additionally, precise alignment is needed to coupled a laser source into the cavity to achieve the needed power buildup. This makes linear cavity systems impractical for operation in more stressful environments.

Integrating cavity enhancement offers a means to achieve the needed enhancement. To demonstrate the enhancement capabilities of integrating cavities, we first measure a Raman signal from the atmosphere.[95] Since the integrating cavity will be filled with atmospheric gas unless it is under vacuum, this simply involves coupling narrow band laser light into the cavity and detecting the output with a spectrometer.

The cavity used in this experiment was described in detail in Chapter 3. Briefly, fumed silica powder was used as a diffuse reflector for the integrating cavity walls.

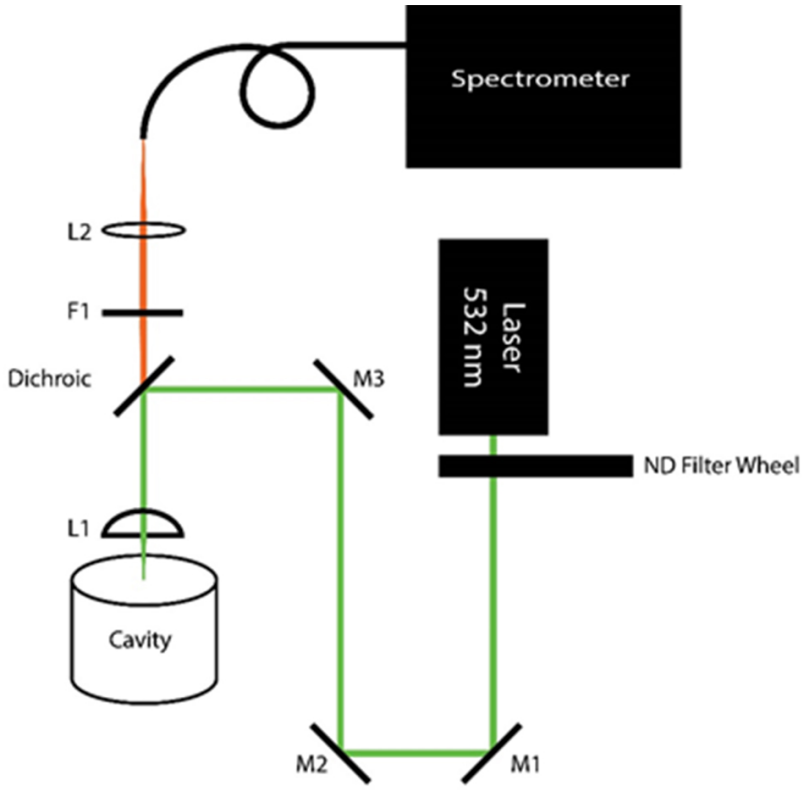

Figure 4.2: Diagram of the Raman spectroscopy system used for measuring Raman scattering from atmosphere.

The cavity was manufactured using two quartz rings, each of 101.6 mm inner diameter and 50.8 mm height. The quartz powder was packed using a hydraulic press such that two semi-solid discs were made. A 50.8 mm right-circular cylinder bore that was 25.4 mm deep was machined into each half. In one of the cavity halves, a 2 mm hole was drilled in the center of the 50.8 mm inner cavity, to create an aperture to couple light into and out of the cavity. The two discs were stacked on top of each other to create the integrating cavity.

The optical setup used for Raman spectroscopy from air is shown in Fig. 4.2. Here, a 150 mW, 532-nm neodymium-doped yttrium orthovanadate (Nd:YVO_4) laser was

used as the excitation source. The output of the laser was passed through a neutral density filter wheel with filters ranging from ND 0 - 4. For all Raman measurements, 0 ND was placed in the path of the laser. This filter wheel was only used to aid in aligning the laser beam into the integrating cavity. The beam was then directed up a periscope before being reflected off a 532-nm dichroic mirror mounted at 45°(Semrock Di02-R532-25x36, USA). The beam was gently focused into the integrating cavity using a 25.4 mm diameter 20 mm focal length aspheric condensor lens (Thorlabs ACL2520, USA). This lens was selected due to its relatively high numerical aperture (NA = 0.543). A high NA lens was used to attempt to maximize the collection of Raman signal generated inside the cavity, since this signal would exit the cavity in a very diffuse manor. The Raman signal passed through the dichroic and an additional 532-nm long pass filter (Semrock BLP01-532R-25, USA). This was used to remove any of the excitation light that returned from the integrating cavity and passed through the dichroic. The Raman signal was focused onto the tip of a fiber bundle using a matching 20-mm focal length aspheric condenser lens. The fiber bundle consisted of one central fiber surrounded by 6 additional fibers, each with a 200-μm core. The individual fibers are arranged in a line on the other tip, which is imaged to the slit of a 0.300 Acton CCD spectrometer (Princeton Instruments, USA). The CCD was thermoelectrically cooled to -70°C to minimize electrical noise. With the spectrometer slit set to 10 μm, the spectral resolution was limited to 3.25 cm^{-1} for the 532 nm laser source.

Raman spectra for atmosphere were recorded with a slit width of 200 μm, with typical integration times of 200 ms and 30 accumulations. The integrating cavity was aligned to the optical system via a custom adjustable stage with 5 degrees of freedom. The stage could move the cavity with micrometer precision in the x,y, and z directions, as well as adjusting the pitch and tilt. Alignment was achieved by first

aligning the cavity so to increase the detected fluorescence background. Following this, the alignment was optimized by maximizing the single shot peak intensity for the nitrogen line located at 2330 cm^{-1}. While optimal alignment is not necessary to couple light into the cavity, this was necessary to maximize coupling of the signal into the optical fiber.

The Raman spectrum of atmosphere without any post processing is shown in Fig. 4.3. While the Raman lines for O_2 and N_2 can clearly be seen, there is also a significant background contribution to the spectrum from the integrating cavity. Broad fluorescence background is typically seen from quartz, and is often seen with a glass microscope slide placed under a commercial Raman microscope. Accurate removal of this background, without attenuation of the Raman peaks is critical for detecting signal went the intensity of the Raman peak is significantly lower.

Several techniques have been developed to achieve this goal. Since the background is broad in wavelength and the Raman peaks are quite narrow, it is possible to accurately remove fluorescence background without altering the Raman peak intensities.[96] Perhaps the simplest method that has been proposed is to simply fit a polynomial function to the spectrum. While this approach can do a reasonable job of background removal, fitting to all of the spectral data can result in the Raman peaks influencing the fit, and thus changing their intensities after subtraction based on the fit. To overcome this issue, a modified polynomial fit method has been developed.[97] Here, the spectrum is first fit with a N-th order polynomial. Following this, the fit is checked point-by-point and for every point of the fit that is greater than the corresponding point in the raw spectrum, the fit point is replaced with the spectral point. This process is then iterated over, typically 25-100 times. Due to the odd shape of the fluorescence background seen in Fig. 4.3, this method leave significant background behind after subtraction, particularly near the oxygen Raman line. A

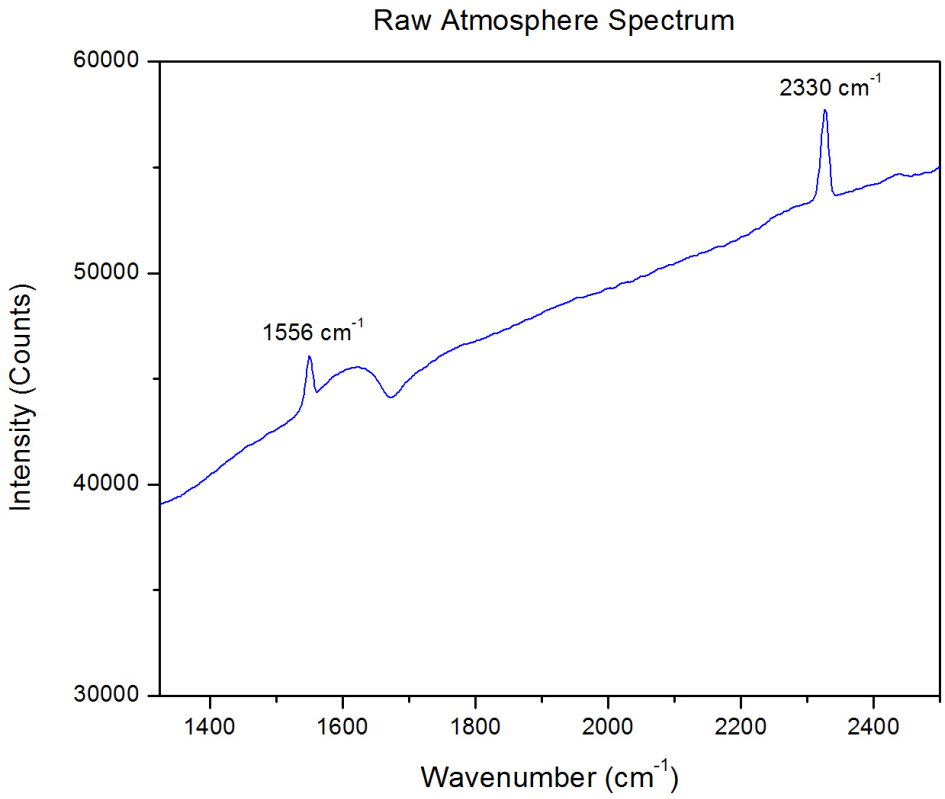

Figure 4.3: Raman spectrum of atmosphere without background subtraction. The 1556 cm^1 peak is from O_2 and the 2330 cm^{-1} peak is from N_2.

second approach is to apply a rolling-circle filter to the spectrum.[98] The rolling-circle filter acts as a high pass filter, removing only the low frequency components of the signal. Finally, intelligent algorithms have been proposed that first detect Raman peaks by continuous wavelet transform (CWT), then estimate the peak-width from derivative calculations based on the CWT and finally remove fit the background using a penalized least squares method.[99]

To remove the varying background seen in the spectrum in Fig. 4.3, we employ a combination of several previously developed methods. Since single polynomials do not fit the entire range of the spectrum, a cubic spline is used instead. Cubic splines can be used to fit any arbitrary shaped curve, including Raman spectra.[100] Smoothing, or dampened splines can be used to fit the general shape of the background, but will still attempt to fit to the Raman peaks. Before fitting a cubic spline, the raw signal is low pass filtered by using a moving window. The window assigns no weight points that lie outside six mean absolute deviations, allowing for quickly rising Raman peaks to be ignored. This results in a smooth version of the Raman spectrum, with significant attenuation the Raman peaks. After smoothing, a dampened cubic spline is fit to the data. The dampening coefficient is chosen to be sufficiently small so that the Raman peaks are mostly ignored, but the spline still follows the shape of the background curve. Similar to the iterative polynomial fit methods, the spline fit is checked point-by-point, and each point of the fit that is greater than the smoothed spectra is replaced with the smoothed value. The corrected fit function is then passed as an argument to the fitting function, and a new split curve is returned. The iteration allows for each successive fit to further ignore the Raman peaks, as typically the only values of the fit that are greater than the spectrum are those on the edges of the Raman peaks. An example of this fitting can be seen in Fig. 4.4 where the black trace shows the raw data and the red trace shows the cubic spline

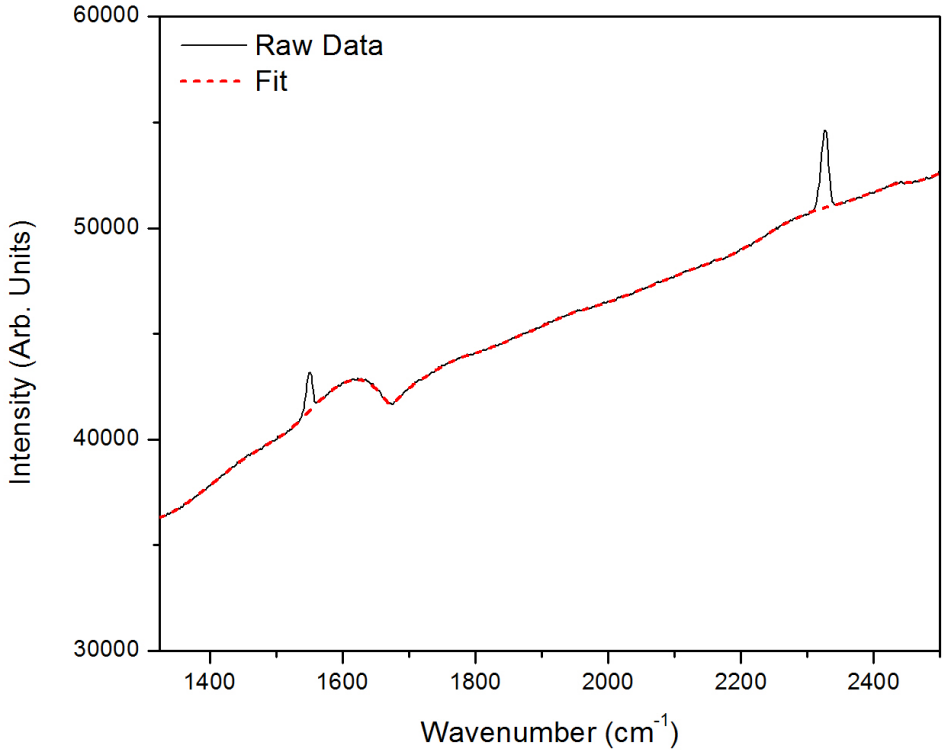

Figure 4.4: Raman spectrum of atmosphere and the fit used to subtract the cavity background.

fit. The fit curve completely ignores the Raman peaks, while perfectly matching the shape of the background.

Fig 4.5 shows the Raman signal remaining following subtraction of the fit curve. The fit does not removed the noise in the original spectrum, or decrease the intensity of the Raman peaks. Noise can be filtered at this point by using smoothing methods such as Savitzky-Golay filter. This is a generalized moving average with filter coefficients determined by an unweighted linear least-squares regression and a second order polynomial model. One advantage of the cubic spline fitting approach

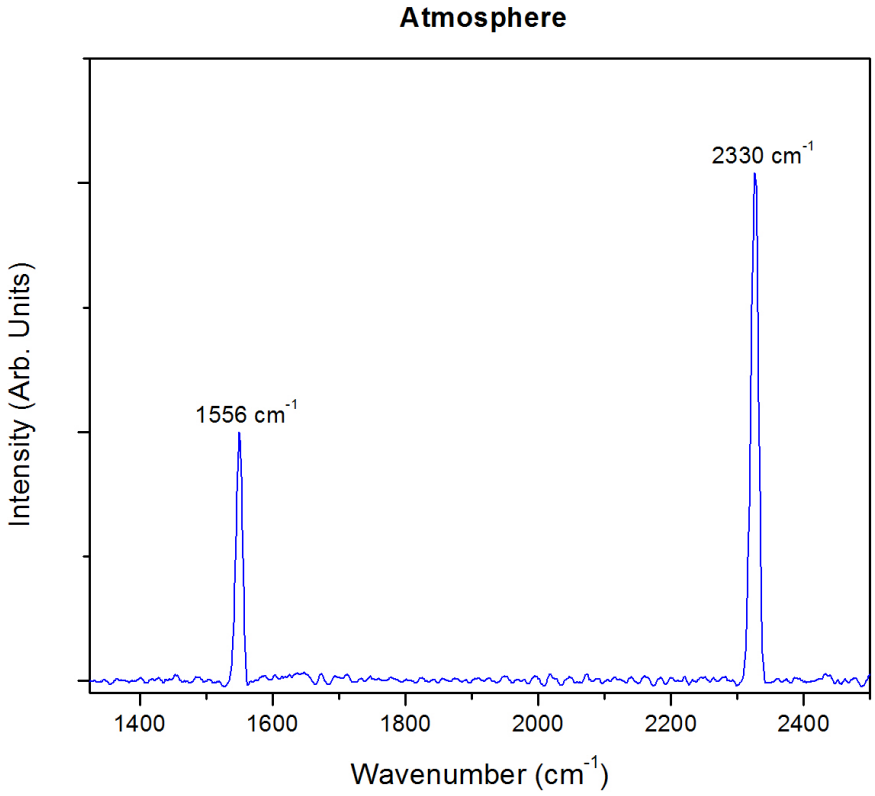

Figure 4.5: Raman spectrum of atmosphere with cavity background subtracted. The 1556 cm^1 peak is from O_2 and the 2330 cm^{-1} peak is from N_2.

is a relatively few number of iterations are needed. Here, only 3 iterations of the fit were used. Work is still needed to optimize the dampening parameter used so that the method can be generalized and automated. Currently, the dampening parameter is chose by trial and error. This could potentially be done by using similar methods to those developed by Zhang *et al.*, that first detects the location and width of peaks before fitting to the background.[99]

This spectrum, while only of atmosphere, demonstrates the ability of an integrating cavity to provide significant enhancement of Raman scattering. We can compare

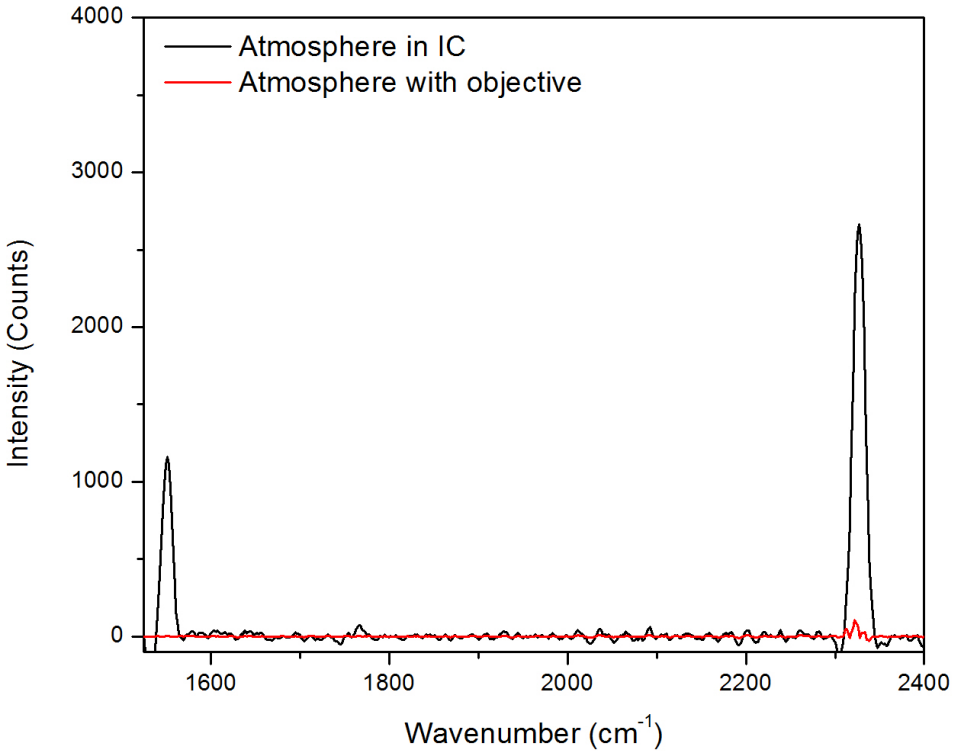

Figure 4.6: Raman spectrum of atmosphere collected with an intergrating cavity (black trace) and with a 20x, 0.5 NA microscope objective. The spectrum collected with a microscope objective was taken with an intergration time of 60 seconds and 60 accumulations. The Raman spectrum taken inside the integrating cavity used an integration time of 40 ms and 30 accumulations.

the Raman spectrum from atmosphere inside an integrating cavity to that collected with a microscope objective. This is shown in Fig. 4.6. The Raman spectrum of atmosphere in the integrating cavity was taken with a 20 ms integration time for 30 accumulations. The Raman second Raman spectrum was taken with a 20x, 0.5 NA microscope objective (Olympus) with a 60 second integration time and 60 accumulations. When account for total detection time, the integrating cavity accounts for 10^5 increase in the number of photons detected by the spectrometer CCD. More efficient collection of the emission from the cavity could allow for an even greater increase.

4.4 Detection Limits for Environmental Toxins

To further demonstrate the enhancement provided by integrating cavity Raman spectroscopy, we will experimentally determine the detection limits for three polycyclic aromatic hydrocarbons (PAH). The first of these is benzo[a]pyrene (BaP). BaP is one of the principle carcinogens found in cigarette smoke.[101] Exposure to BaP has been directly linked to the formation of lung cancer.[102] Exposure can occur from cigarette smoke, fossil fuel industries, fossil fuel combustion, as well as biomass combustion.[103] BaP has been classified as a group 1 carcinogen by the United States Environmental Protection Agency. Pyrene is the second hydrocarbon used for detection studies. While not as toxic as BaP, pyrene has been shown to potentially be toxic to the kidneys and liver, and to aquatic life.[104] Naphthalene is the third hydrocabon that will be used for Raman spectroscopy. Naphthalene has been shown to be carcinogenic in rats. Because of this, the US EPA has classified naphthalene as potentially carcinogenic in humans, and has created exposure limits of 10 ppm per 8 hour time-weight average.[103] The chemical structure of all three PAH's are shown in Fig. 4.7. BaP has the chemical formula of $C_{20}H_{12}$, naphthalene has a formula of $C_{10}H_8$, and pyrene has a formula of $C_{16}H_{10}$.

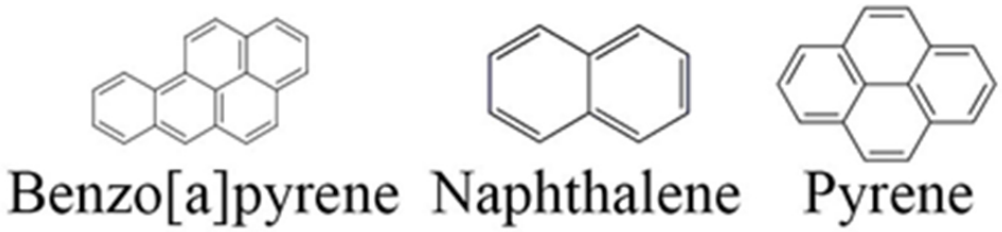

Figure 4.7: Chemical structure of the three polycyclic aromatic hydrocarbons: benzo(a)pyrene, naphthalene, and pyrene.

Raman spectra of all three PAH's were recorded with a commercial Raman microscope (Horiba Scientific). The Raman spectrum for naphthalene is shown in Fig. 4.9. The strongest spontaneous Raman line is located at 1383 cm^{-1}. This line will be used for determining detection limits from integrating cavity Raman spectroscopy. A second line can be seen at 1577 cm^{-1+}. This line is sufficiently far enough from the oxygen peak that will also be seen in Raman spectra collected with the integrating cavity.

4.4.1 532 nm Detection Limit Study

.

Raman spectra for BaP and pyrene are shown in Fig 4.8 and Fig. 4.10, respectively. The strongest Raman shift for BaP is seen at 1235 cm^{-1}. This line, along with the line at 1385 cm^{-1} will be used for determining the detection limits of this PAH. Pyrene has the strongest Raman shift at 1403 cm^{-1}, along with a second line at 1239 cm^{-1}. The 1403 cm^{-1} line was primarily used for detection limit evaluations. All samples will be contained in a quartz crucible during data acquisition. The oxygen and nitrogen peaks can be used to normalize data from sample to sample. The

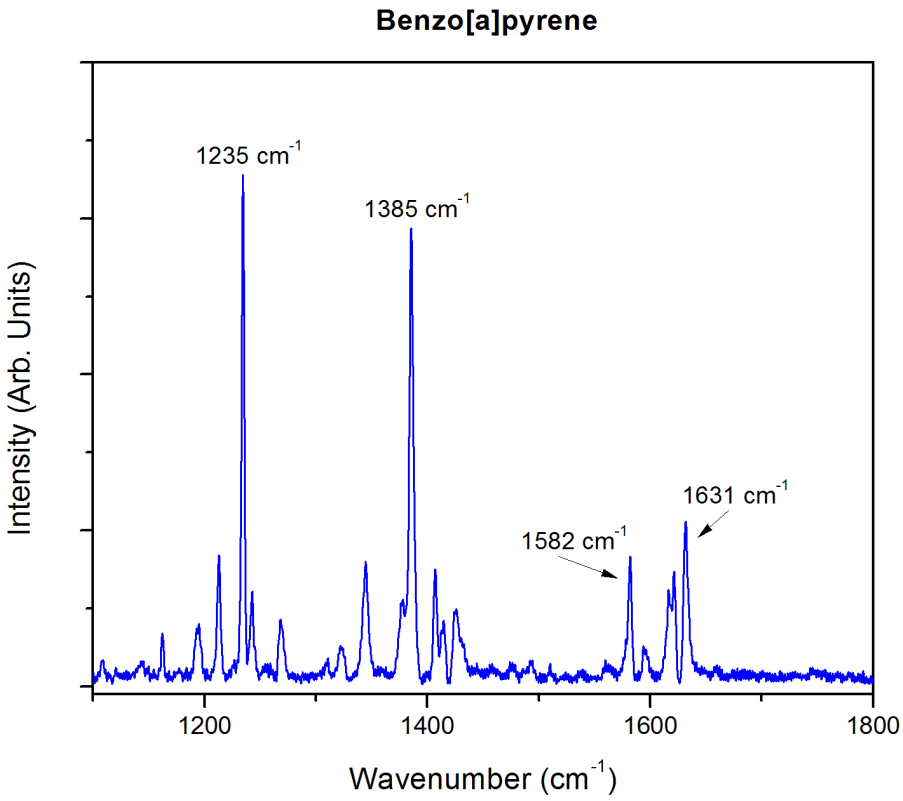

Figure 4.8: Raman spectrum of benzo(a)pyrene recorded with a Horiba Scientific Raman microscope. The Raman shifts for the four of the lines shown are labeled.

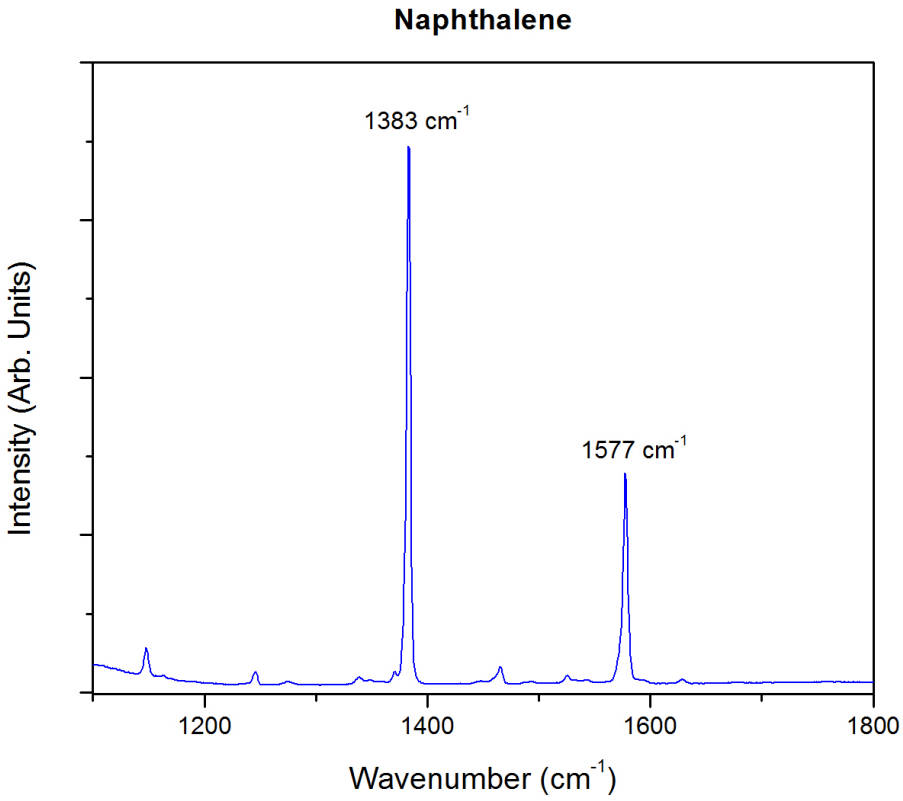

Figure 4.9: Raman spectrum of naphthalene recorded with a Horiba Scientific Raman microscope. The Raman shifts for the two strongest lines are labeled.

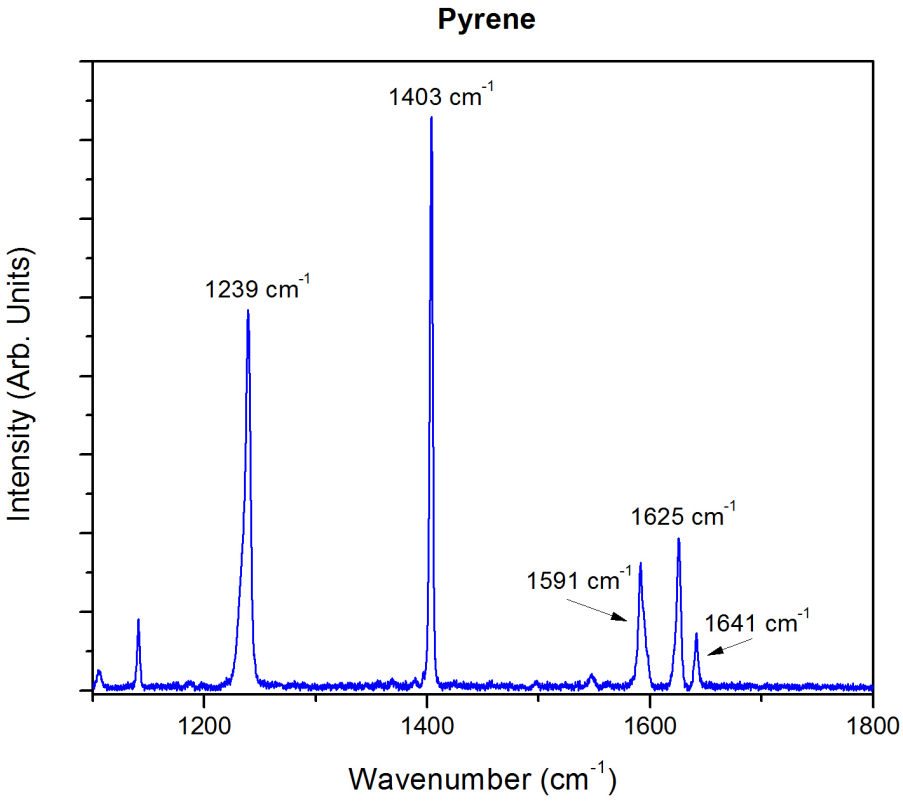

Figure 4.10: Raman spectrum of pyrene recorded with a Horiba Scientific Raman microscope. The Raman shifts for the five of the lines shown are labeled.

intensities of these lines should not change from sample to sample, and thus can be used for aligning the cavity into the optical system, and to normalize spectral data to account for any variation in cavity alignment. Additionally, normalization to the oxygen or nitrogen peaks can allow for scaling spectral data that is collected at different integration times.

To experimentally determine detection limits for the three PAH's listed above, samples were carefully weighed out into quartz crucibles using a micro balance (Citizen CX265). BaP weights ranged from 80 μg to 400 μg, pyrene weights ranged from 100 μg to 510 μg, and naphthalene weights ranged fro 200 μg to 550 μg. These values were converted to a molar concentration by calculating the molar mass of each sample and dividing this by the volumetric area of the cavity bore. Raman spectra were then collected for each sample. To demonstrate the repeatability of these measurements, five sets of spectra were recorded for each concentration. The integration times of the spectrometer were set to the longest time possible such that no saturation of the detector occurred. Normalization of the data sets to account for differences in integration time was done by scaling the oxygen peaks of an individual spectrum to the mean intensity value of the oxygen peak for each concentration.

The raw Raman spectrum for all concentrations of BaP is shown in Fig. 4.11. The 1556 cm^{-1} oxygen peak was used for normalization. The intensity of the 1385 cm^{-1} peak was used to calculate a regression for concentration versus Raman intensity. This peak was chosen due to its relative strength, and its proximity to the oxygen peak. The background in all the spectra was removed using the iterative cubic spline fitting model discusses previously in this section. Fig. 4.12 shows a plot of the intensity of the intensity of the 1385 cm^{-1} Raman line vs. the concentration of BaP in the cavity. A linear regression fit to this data resulted in a $R^2 = 0.933$. Error bars indicate the standard deviation of the average peak intensity from each of the five

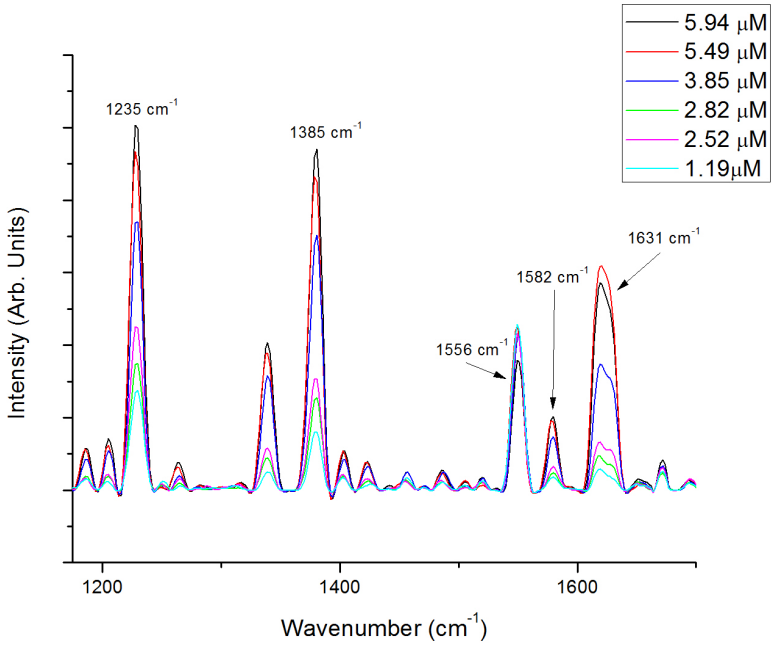

Figure 4.11: Raman spectrum of benzo(a)prene measured inside an integrating cavity with background subtraction.

samples. The minimum concentration was limited by the smallest mass that could reliable be weighed by the balance used. Based on the equation of the linear fit to this data, the minimal detection limit for BaP is 700 nM with 532 nm excitation.

Fig. 4.13 shows the Raman spectra for each concentration of naphthalene placed inside the integrating cavity. The spectra are shown before correction for differences in integration times was applied. Intensity calculations were based off the Raman peak at a shift of 1383 cm^{-1}. Fig. 4.14 shows the intensity of the 1383 cm^{-1} Raman line vs. the concentration of naphthalene in the cavity. Again, the minimum concentration detected was limited by the smallest mass that could be repeatably weight by the balance. Based on the equation for the linear fit to this data, the minimal detectable limit of 3.1 μM for the 532 nm excitation.

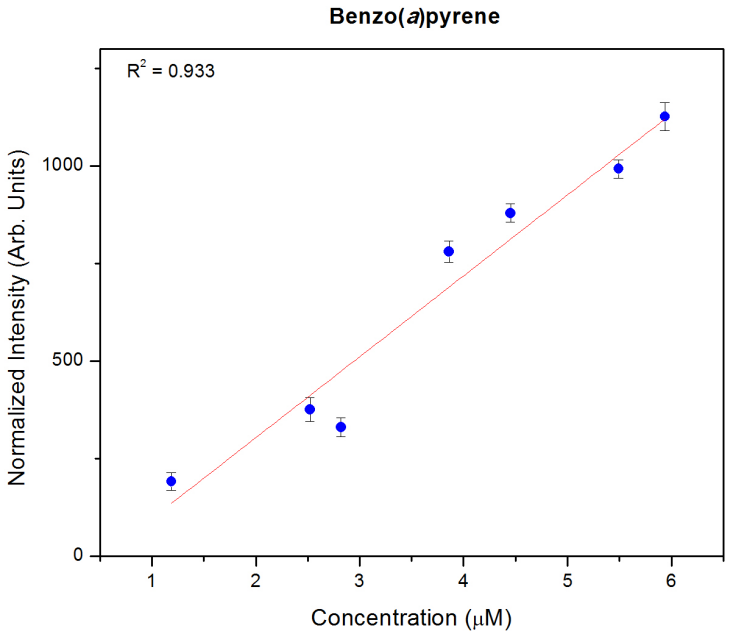

Figure 4.12: Plot showing the intensity of the 1385 cm^{-1} Raman line vs. the concentration of BaP in the integrating cavity. A linear regression fit to this data resulted in a $R^2 = 0.933$.

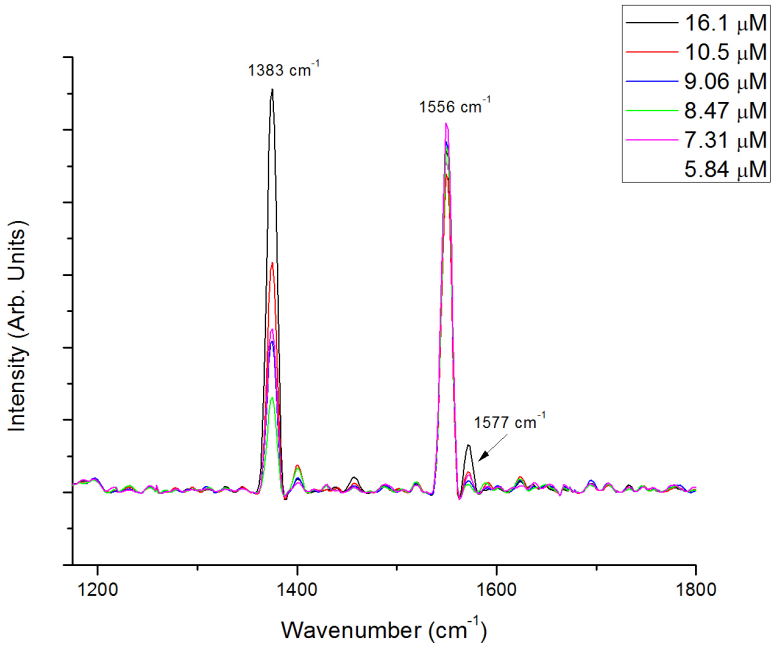

Figure 4.13: Raman spectrum of naphthalene measured inside of an integrating cavity after background subtraction.

Finally, Fig. 4.15 shows the Raman spectrum of all concentrations of pryene measured inside of an integrating cavity after background subtraction. Here, the 1403 cm^{-1} Raman shift was used for calculating Raman intensities. Fig. 4.16 shows a plot of the intensity this Raman shift vs. the concentration of pyrene in the integrating cavity. A linear regression fit to this data returned an $R^2 = 0.975$. Based on the equation of this line, the minimum detectable concentration of pyrene with 532 nm excitation is 690 nM.

4.4.2 473 nm Detection Limit Study

While previous Raman spectra were collected using 532 nm excitation, here we will experimentally determine the detection limit of pyrene with the use of a 100 mW, 473 nm diode pumped solid state (DPSS) laser. With all other parameters the

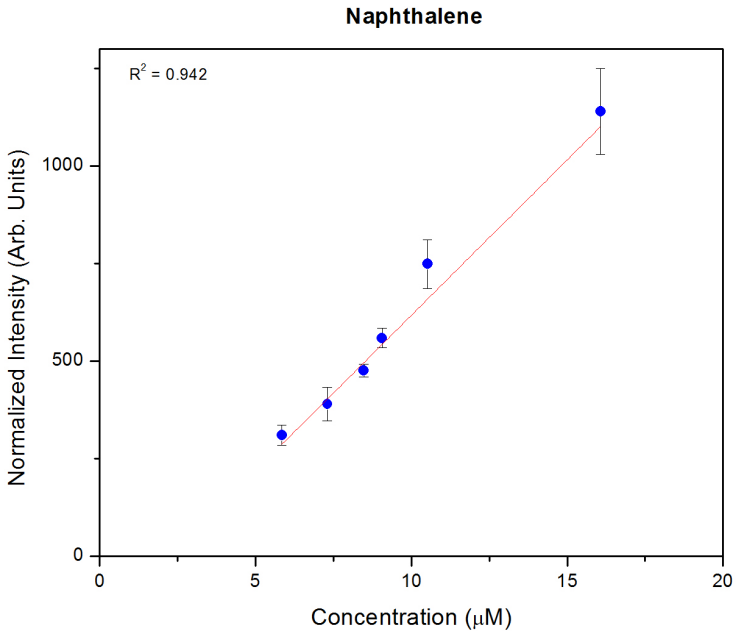

Figure 4.14: Plot showing the intensity of the 1383 cm^{-1} Raman line vs. the concentration of naphthalene in the integrating cavity. A linear regression fit to this data resulted in a $R^2 = 0.942$.

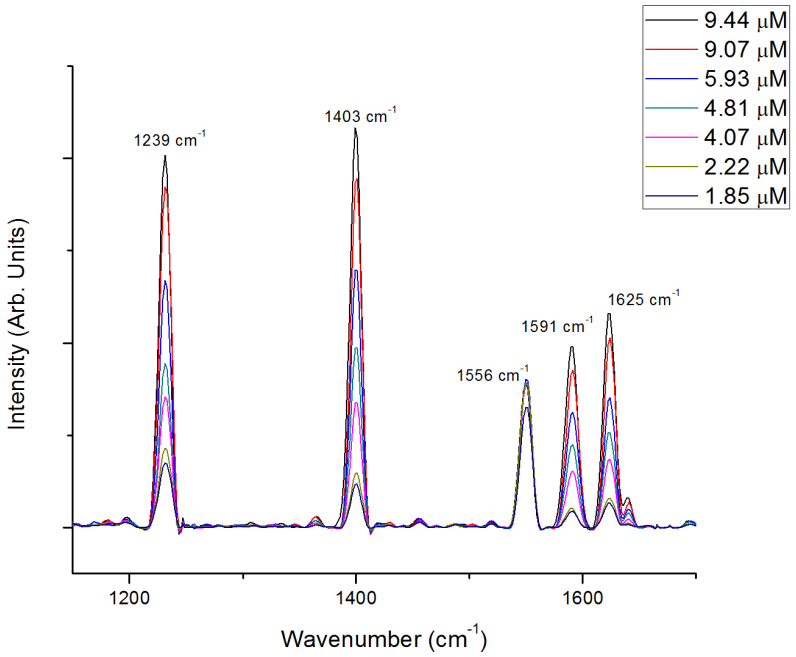

Figure 4.15: Raman spectrum of pryene measured inside of an integrating cavity after background subtraction. A linear regression fit to this data resulted in a $R^2 = 0.975$.

same, we expect a 1.6 increase in Raman signal generation by using a 473 nm DPSS laser as opposed to the 532 nm source. This is due to the power of Raman scattered light, P_s, being proportional to I_0/λ^4, where I_0 is the intensity of the excitation source.

The experimental setup for the 473 nm excitation is shown in Fig. 4.17. The optical design is identical to the setup described for 532 nm Raman spectroscopy. Here, a 488 nm dichroic mirror (Di02-R488-25x36, Semrock) was mounted at 45° to direct the excitation source down into the cavity. The same optics were used to focus light into and collect light exiting from the cavity. A 488 nm long pass filter (BLP01-488R-25, Semrock) was used to remove any additional excitation light from being sent to the spectrometer. An 0.300m Acton CCD spectrometer with a 1200

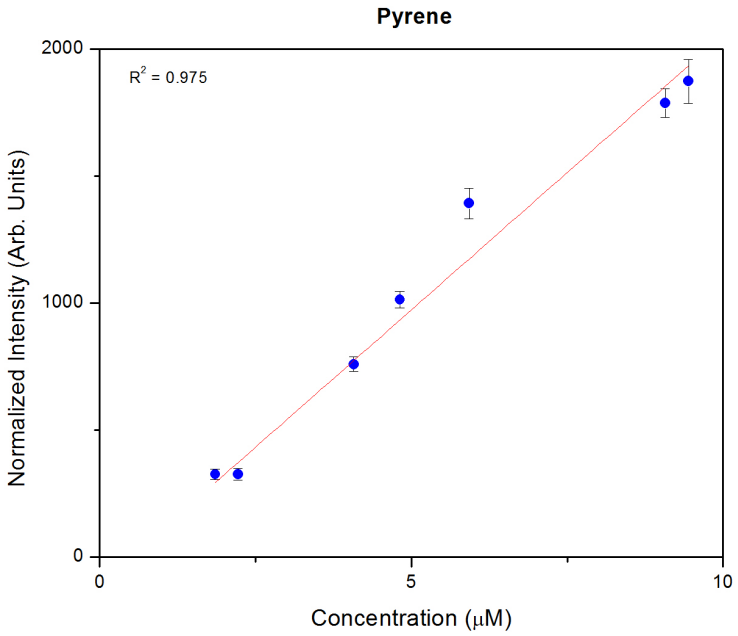

Figure 4.16: Plot showing the intensity of the 1403 cm^{-1} Raman line vs. the concentration of pyrene in the integrating cavity.

lines/mm grating was used for data acquisition. All spectra were recorded with a slit width of 50 μm.

Because repeatably weighing out samples of lower mass than those values previously use is not possible, different techniques were employed to further test the detection limits for the PAH's used here. To do this, 500 μg of pyrene was measured on a differential scale. This mass was then dissolved in volume of ethanol, creating a solution pryene of with a concentration of 1 mM. A pipette was then used to deposit the desired mass of pyrene into a clean crucible. The crucible was placed in a fume hood with a piece of lens paper covering the top. This was done to ensure dust or other debris did not contaminate the sample. The crucible was allowed to sit for an hour to all the ethanol to evaporate off, leaving only pyrene in the crucible. Using

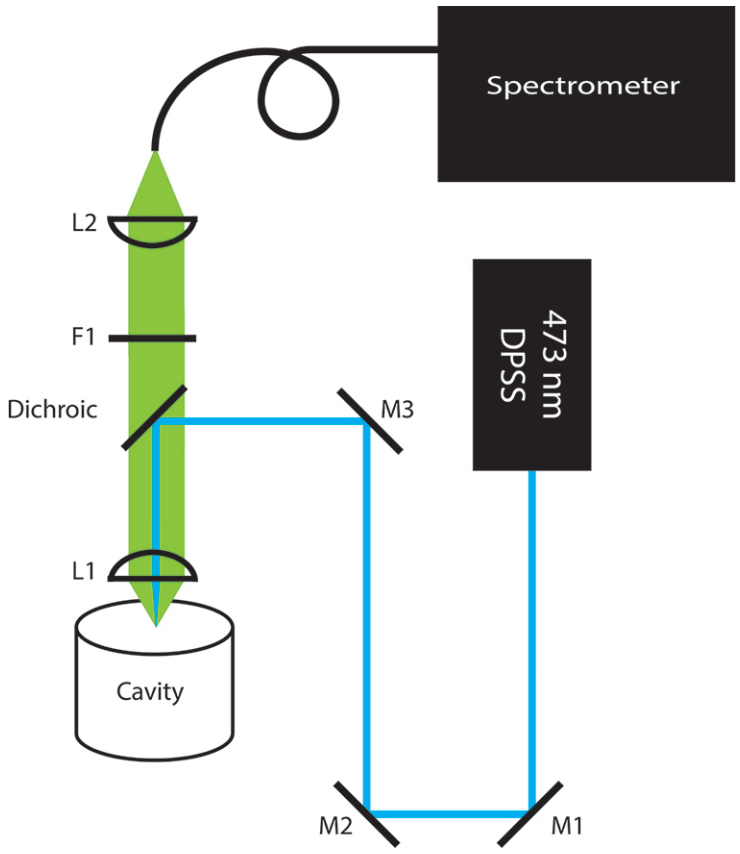

Figure 4.17: Optical system used for polycyclic aeromatic hydrocarbon Raman spectroscopy.

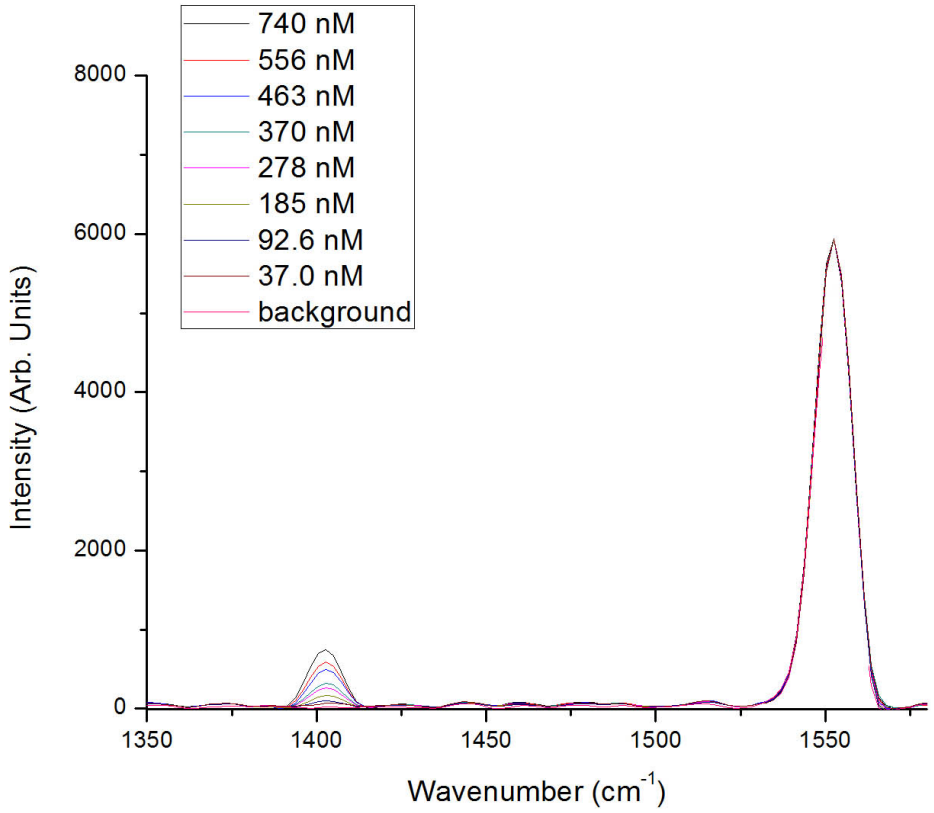

Figure 4.18: Plot of the Raman spectra for pyrene with 473 nm excitation for all concentrations.. The spectra shown correspond to the average spectra obtained after background subtraction for the 5 samples at each concentration.

this method, samples were prepared with masses ranging from 40 ug to 100 ng. Pure ethanol evaporations were used as a background for detection limit purposes. Following the evaporation, the crucible was placed in the integrating cavity and aligned into the optical system. Spectra were recorded with the maximum possible integration time that did not result in saturation of the detector and for 50 accumulations. Typical integrating times ranged from 2 to 5 seconds per accumulation. Five samples were made at each concentration for data acquisition.

Fig. 4.18 shows a plot of the average Raman spectra for all pyrene concentra-

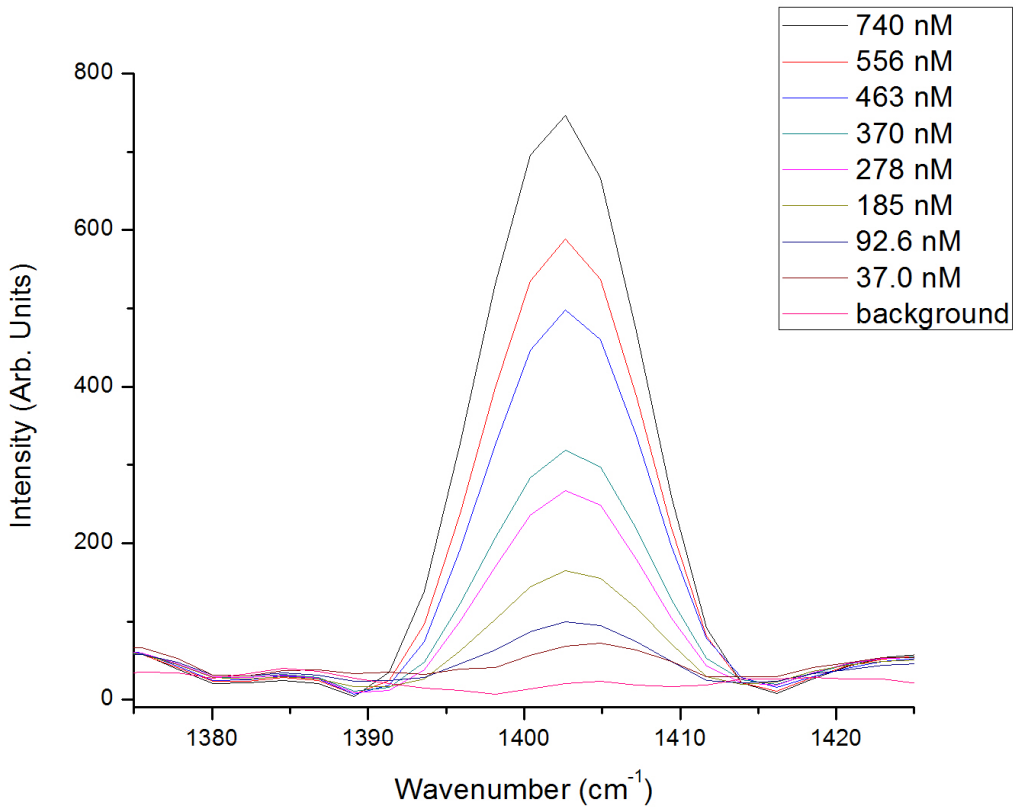

Figure 4.19: Plot of the Raman spectrum for pyrene from 1375 cm^{-1} to 1425 cm^{-1} showing the Raman shift at 1403 cm^{-1} for all concentrations.

tions measured. The individual spectra for each concentration can be found in Appendix A. The Raman spectra were normalized to the oxygen peak at 1556 cm^{-1}. This allows for correction based on any difference in integration times used, as well as for adjustment for any inconsistency in cavity alignment. Fig. 4.19 shows a zoomed in view of the Raman shift at 1403 cm^{-1}.

The cavity background was subtracted using the same iterative cubic spline fit detailed in Section 4.4.1. Following background removal, the intensity of the peak was calculated using two methods. The first method simply recorded the maximum value of the Raman shift. This method can be prone to error in background removal. For weaker signals, integration of the Raman shift can often result in more sensitive detection. To do this, a Gaussian function with fixed center location and fixed width was fit to each spectra.[94] The only variables in the fit were the amplitude of the Gaussian, and an offset. The Gaussian function was then integrated with the baseline offset term excluded. This allows for more accurate subtraction of any remaining background, as well as a better measure of the magnitude of the peak.

Fig. 4.20 shows a plot of the intensity of the Raman shift as a function of concentration of pyrene in the integrating cavity. A linear regression fit to this data returned an R^2 value of 0.988. Error bars indicate the standard deviation of the average peak intensity measured from 5 samples. Using a detection threshold of 3σ (corresponding to the mean of the blank plus three times the standard deviation of the blank), the limit of detection was found to be 13.16 nM.

Integrating cavities can provide significant Raman enhancement. Here, we demonstrate the potential for detection of PAH's in the tens of nanomolar range. The strong linear fits to all plots of concentration versus intensity data indicate the high potential for this technique to provide quantitative data regarding the concentration of an sample provided proper calibration has been preformed. The use of further blue

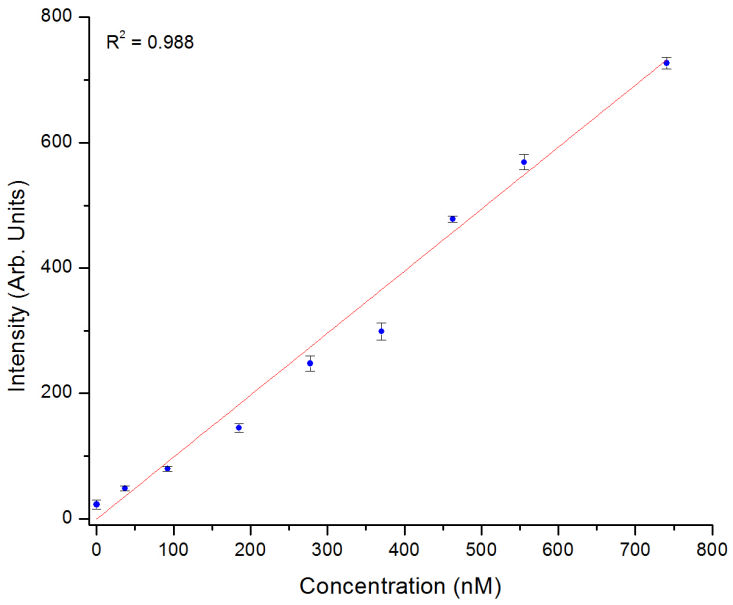

Figure 4.20: Plot of the intensity of the Raman shift for pyrene vs. the concentration of pyrene inside the integrating cavity. A linear regression fit to this data returned an R^2 value of 0.988. Error bars indicate the standard deviation of the average peak intensity measured from 5 samples. From this fit, the limit of detection using a 3σ threshold was determined to be 13.16 nM.

shifted excitation light, or higher power sources could further reduce these detection limits.

4.5 Summary

Integrating cavity enhanced Raman spectroscopy can provide significant enhancements factors to spontaneous Raman spectroscopy. Based on the nitrogen peak measured with 532 nm excitation with an integrating cavity compared to the signal collected from a microscope objective, we can estimate this enhancement factor to be on the order of 10^5. The enhancement can be further increased with the use of more blue shifted sources, since the power of the scattered signal scales proportional to I_0/λ^4. Increasing the excitation intensity will result in an increased background signal from the integrating cavity, in addition to the increased Raman signal generation. *A priori* knowledge of the location of the Raman shifts can allow for filtering to enhance signal to noise and improve detection limits.

Samples with strong fluorescence would cause significant decreases in the enhancement offered by an integrating cavity. Typically, Raman spectroscopy is preformed with red shifted sources for samples with strong endogenous fluorescence, to minimize the fluorescence background. Since the reflectivity of the integrating cavity drops off for longer wavelengths, the enhancement factor would also decrease. Despite this, integrating cavity Raman spectroscopy could find application in liquid and gas analysis, where absorption or fluorescence from blue excitation light will not overwhelm the Raman signal.

5. FLUORESCENCE ENHANCEMENT*

5.1 Introduction

In this Chapter, we will use the same integrating cavity described above to provide enhancement for fluorescence spectroscopy-based sensing. The enhancement provided by the integrating cavity of fluorescent emission come from the same basic principles as was seen with the enhancement of spontaneous Raman scattering. First, due to the Lambertian nature of the diffuse reflector that makes up the integrating cavity, a isotropic field exists inside the cavity. This means that, regardless of location, any fluorophore inside the cavity can be excited. Second, because of the long effective pathlength light experiences inside the cavity, photons can undergo multiple passes through a sample. Because of this, photons that pass through the sample, but are not absorbed by any fluorophores, can have multiple changes to undergo absorption followed by remission via a fluorescent or phosphorescent transition as was depicted in Fig. 1.4.

To demonstrate the enhancement capabilities of an integrating cavity for fluroescence-based sensing, we will determine the detection limits for a urobilin phosphor complex. Following this, we will demonstrate that slightly increasing the scattering inside a sample can result in further fluorescence enhancement. With too much additional scattering, the entire volume of a sample placed inside the integrating cavity is unable to be probed, reducing the measured fluorescence emission. This technique has tremendous potential for a wide variety of sensing applications such as detection of

*Portions of this section are reprinted with permission from "Ultrasensitive detection of waste products in water using fluorescence emission cavity-enhanced spectroscopy," J.N. Bixler, M.T. Cone, B.H. Hokr, J.D. Mason, E. Figueroa, E.S. Fry, V.V. Yakovlev, and M.O. Scully, 2014 *Proceedings of the National Academy of Sciences*, **111,** 20 and "Utilizing scattering to further enhance integrating cavity enhanced spectroscopy," J.N. Bixler, C.A. Winkler, B.H. Hokr, J.D. Mason, V.V. Yakovlev, 2015 *Journal of Modern Optics*

dissolved organic material and adding sensitivity to fluorescence-based immunoassays.

5.2 Ultrasensitive Detection of Waste Products in Water Using Fluorescence Emission Cavity-Enhanced Spectroscopy

5.2.1 Background

It is axiomatic that the quality of water is essential for human health.[105] The increasing worldwide contamination of freshwater systems with thousands of industrial and natural chemical compounds is one of the key environmental problems facing humanity today, where pathogens in water cause more than 2 million deaths annually.[1] With more than one-third of the accessible and renewable freshwater used for industrial, agricultural, and domestic applications, pollution from these activities leaves water sources contaminated with numerous synthetic and geogenic compounds.[1,106] In addition, natural disasters can result in large scale disruptions of infrastructure, resulting in compromised water quality. Diarrheal disease caused from such disasters may be a major contributor to overall morbidity and mortality rates.[107] Thus, the cleanliness and safety of public water sources has prompted researchers to look for rapid and sensitive indicators of water quality. While most water filtering systems are quite efficient in removing large-size contaminants, smaller particles frequently pass through. These contaminants are often poorly soluble in water, thus, present in quantities of less than 1 nM. Here, we demonstrate femtomolar detection of urobilin, a biomarker found in human and animal waste in water.

Modern analytical tools have become extremely efficient in the detection and analysis of chemical compounds. For example, liquid chromatography coupled with detection by tandem mass spectrometry has been commonly used for detection of trace pharmaceuticals and other wastewater-derived micropollutants.[108] While such

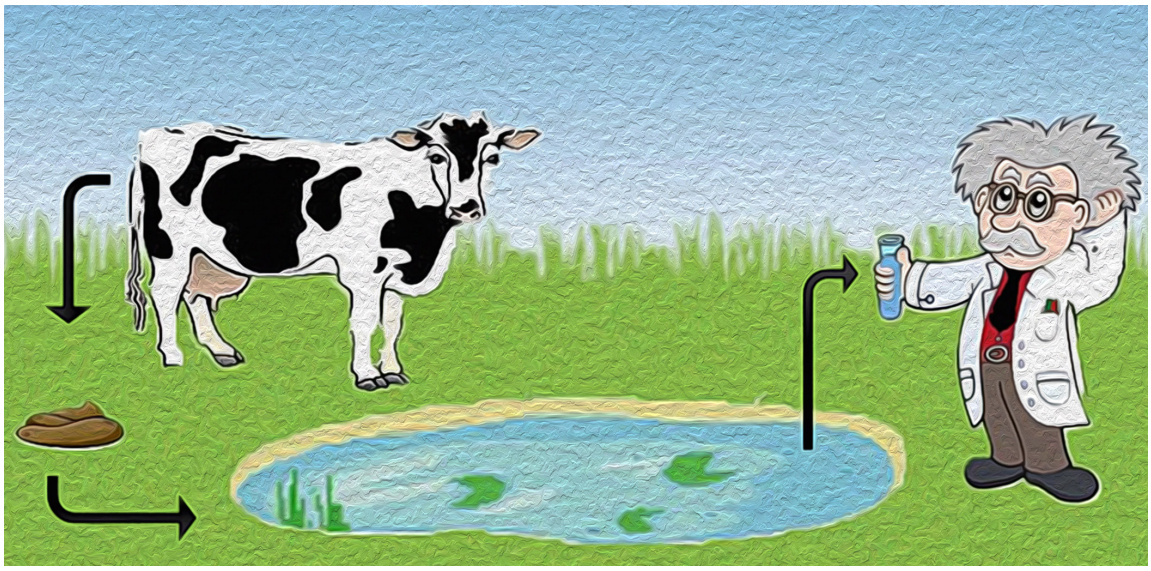

Figure 5.1: Conceptual figure of animal waste polluting a water supply.

methods are very powerful in identifying trace pollutants, cost prohibits their widespread use by environmental researchers and, most importantly, prevents real-time analysis of water quality.[109] Other techniques utilizing bench top gas chromatography/mass spectrometry have also been demonstrated as viable methods for detection of basic pharmaceuticals with reduced cost.[110] Despite this, these methods are still cost prohibitive, can hardly be used in field studies, and are unlikely to ever be used for real-time quality control.

In addition to pharmaceutical and other synthetic pollutants, such as pesticides, animal and human waste (i.e., feces, urine) is an enormous source of water contamination that can be found in both recreational and source waters. Fig. 5.1 shows a conceptual rendering of how animal waste can contaminate source waters. These discarded products when released into water can carry a variety of diseases such as polio, typhoid, and cholera.[14] In extreme cases pollution of an ecosystem can result in environmental crises, such as devastation to the aquatic population, red-tide blooms,

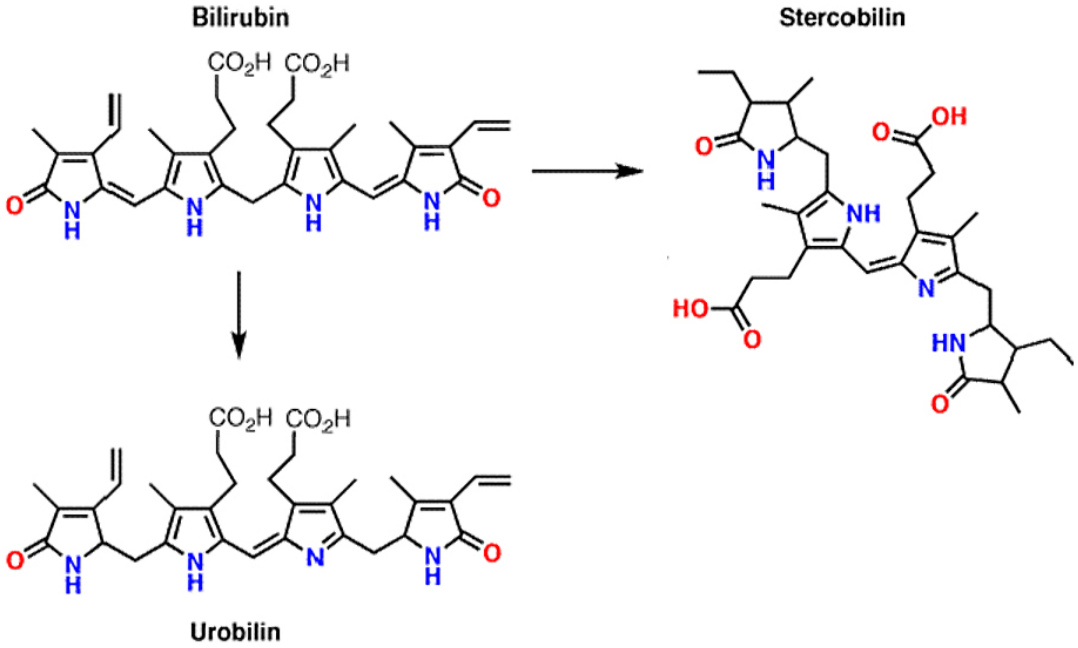

Figure 5.2: Chemical structure of bilirubin, stercobilin, and urobilin. These products are generated from hemoglobin metabolism, and are found in human and animal waste products.

as well as beach closings. Molecular methods based on polymerase chain reactions are commonly used to monitor viral, bacterial, and protozoan pathogens in wastewater.[111] Microbiological indicators such as fecal coliforms, E. coli and Enterococci are the indicators most commonly used to analyze and evaluate the level of fecal contamination. However, the suitability of these indicators has been questioned,[112] and it takes a substantial time from the extraction of water sample for analysis to the moment when the results are ready.

An alternative indicator that has been shown to be helpful in detection of waste in water supplies is urobilin.[113] Urobilin is one of the final by-products of hemoglobin metabolism, and is excreted in both the urine and feces of many mammals, including

both humans and common livestock (cows, horses, and pigs).[114] Fig. 5.2 shows the chemical structure for bilirubin, stercobilin, and urobilin. In addition, as urobilin can be indicative of disease such as hepatic dysfunction, or jaundice, an ultrasensitive technique for detection and quantification of this in solution has both diagnostic and environmental applications.

Urobilin detection in solution has previously been demonstrated using the formation of a phosphor group from the combination of urobilins and zinc ions.[115] Normal heme catabolism results in the production of bilirubin, a red product, which is then broken down into two end products, stercobilin, the bile pigment found in fecal material, and urobilin, the yellow pigment found in urine. Both urobilin and stercobilin have been shown to be viable biomarkers for detection of fecal pollution levels in rivers.[116]

Fluorescent detection of urobilin in urine has previously been demonstrated based on the Schlesinger's reaction in which an urobilinogenzinc chelation complex exhibits a characteristic green fluorescence when excited by blue light.[117] Methods for detection of urobilinoids using high-performance liquid chromatography with a reversed-phase column and a ultraviolet detector have also been presented,[118] however, the initial sensitivity of this method proved insufficient for clinical analysis. Miyabara and coworkers reported an increase in detection sensitivity of this methodology, but only to detection levels of 1.5 nM,[115] where efficient excitation and collection of the fluorescent signal remained the limiting factor. Traditional epi-illumination fluorescence spectroscopy systems utilize an objective lens to focus excitation light into the sample and collect the fluorescence emission. In such a configuration, the signal generated is limited to the focal volume of the optics. In addition, the generated signal is diffusive in nature, only a small fraction of the total emitted light is collected. Because only a small volume of a sample can be probed at any given time

with such a configuration, detection of sub-nanomolar concentrations remains difficult as these measurements are akin to single molecule detection. Thus, a method that could allow for probing a larger volume of a sample, while also providing means for collecting more of the fluorescence emission could greatly enhance the ability to detect sub-nanomolar concentrations of urobilin.

5.2.2 Materials and Methods

To achieve both of these goals, we employ a custom integrating cavity to enhance both excitation and collection efficiency. Integrating cavities, especially spherical cavities, are commonly used to measure the total radiant flux from a source, as a means to generate uniform illumination, and as pump cavities for lasers.[81] In addition to this, such devices have been shown to be a powerful tool for the spectroscopy of weakly absorbing materials.[85] Here, we present a novel application for such cavities: the enhancement of both the excitation and collection of fluorescent emission. Due to the nearly Lambertian behavior of the cavity walls, an isotropic field is created inside the cavity, allowing for fluorescence excitation of the entire volume of any sample placed inside the cavity. In addition, the high reflectivity of the cavity walls leads to very large effective optical path lengths inside the sample region of the cavity. To demonstrate this concept we can consider the following result by Fry *et al.* in.[81] The average distance between reflections, $\bar{d}$, inside an integrating cavity of arbitrary geometry can be expressed as,

$$\bar{d} = 4\frac{V}{S}, \tag{5.1}$$

where V is the cavity volume, and S is the surface area. The average number of reflections for a given photon inside a cavity of reflectivity ρ is given by

$$n = -\frac{1}{\ln \rho}. \tag{5.2}$$

Thus we can express the average effective path length, L, inside the cavity as,

$$L = n\bar{d} = -\frac{4}{\ln \rho} \approx \frac{4V}{S(1-\rho)} \tag{5.3}$$

where the final approximation is valid when ρ is close to unity.

To experimentally determine the reflectivity of the cavity, a cavity ring-down measurement is used.[78,85,119] This involves sending a temporally short pulse of light into the cavity and measuring the exponential decay of the pulse inside the cavity over time. For an empty cavity the decay constant, τ, is related to the cavity reflectivity by the well-known relation,

$$\tau = -\frac{1}{\ln \rho}\left(\frac{\bar{d}}{c}\right), \tag{5.4}$$

where c is the speed of light. In this study a 10 ns pulse from a frequency doubled Nd:YAG laser was launched into the cavity via an optical fiber. The decay, or ring-down signal is sampled with another optical fiber, and detected with a photomultiplier tube (PMT).

Fig. 5.3 shows the input laser pulse, the output decay curve and a fit to that curve. The fit yields a decay constant of 98.14 ns. Using equation 5.4, this gives a cavity reflectivity of 0.9988 at 532 nm. From equation 5.3 we see that our cavity with a diameter of 50.8 mm has an effective path length of approximately 30 m for light in the sample region. Additionally, the inner bore of the cavity has a volume of 103 cm^3, allowing for large sample volumes to be probed as compared to traditional spectroscopy. Thus, we see that this fumed silica integrating cavity provides an ideal means for counteracting the traditional limits of fluorescence spectroscopy. The diffuse scattering of the cavity walls provides isotropic illumination of the sample for maximum excitation, as well as the ability to collect some of the fluorescence signal

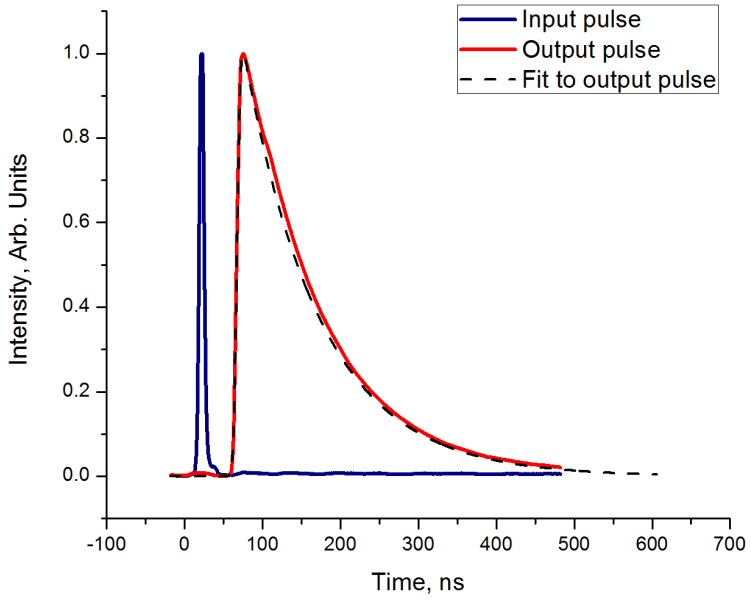

Figure 5.3: Ring-down measurement used to determine cavity reflectance for integrating cavity used in the urobilin detection experiments. The blue trace depicts the input laser pulse, whereas the red trace shows the decay of radiation inside the cavity as measured by a PMT. The black dashed trace is a fit to the decay curve.

emitted from the sample from all 4π steradians. In addition, the high reflectivity of the cavity enhances the fluorescence signal by providing long effective path lengths within the cavities sample region. This means that excitation photons can interact with the sample multiple times, increasing the likelihood of absorption followed by remission via a fluorescence or phosphorescence transition.

For these experiments, we utilized an integrating cavity fabricated from a fumed silica powder (Evonik Industries, Germany). Construction of these cavities was discussed in 3.2, but a brief description of the process is included here. Since the quartz powder is hydrophilic, the material is pre-baked under vacuum at a temperature of 250°C to remove any trapped water. This is done in an a Fischer Scientific Isotemp

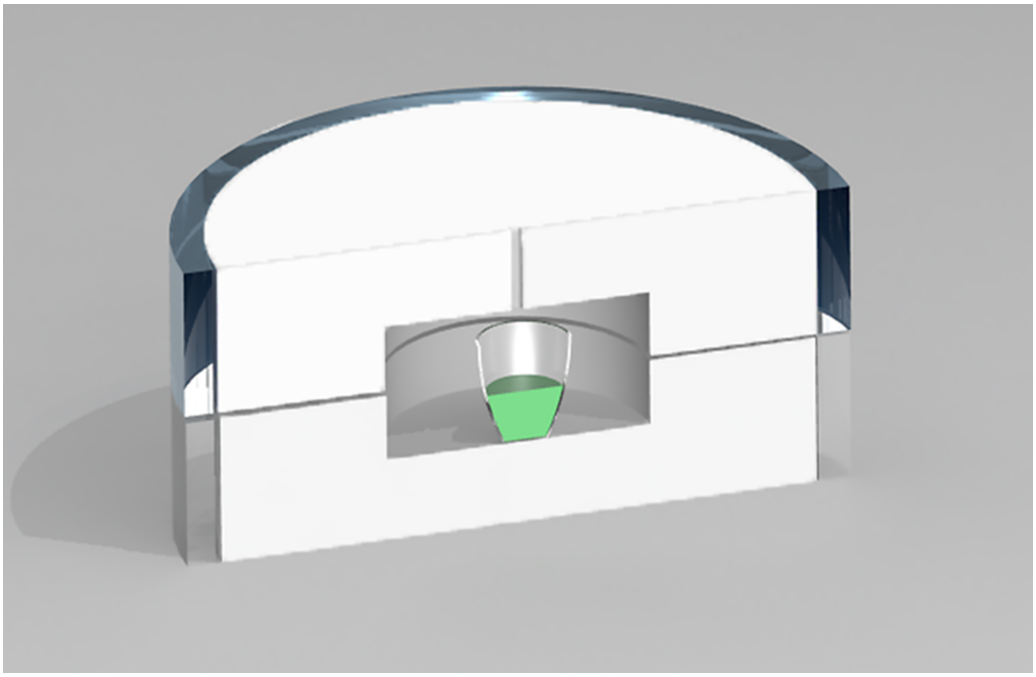

Figure 5.4: Cross-sectional rendering of the cavity including the crucible used to hold samples for urobilin fluorescence experiments

Vaccuum Oven that is coupled to a liquid nitrogen sorption pump, and is purged with high purity argon gas while the material cools. The baked powder is then packed into two sections of quartz tubing (Technical Glass Products, USA) using a hydraulic press. The quartz tubes have an inner diameter of 101.6 mm, an outer diameter of 114.3 mm, and a height of 50.8 mm. These packed pieces are then baked in a high-temperature oven (900-1000 °C) to sinter the material. Following the final bake, the semi-solid nature of the packed powder allow for it to be machined using standard machining techniques. A right circular cylinder is machined into each half to form the desired cavity geometry. Fig. 5.4 shows a cross sectional view of the geometry used. A small hole with diameter of 2.0 mm was drilled through one of the halves to be used for coupling light into and out of the cavity.

Fig. 5.5 shows a schematic of the optical system used for these experiments. A

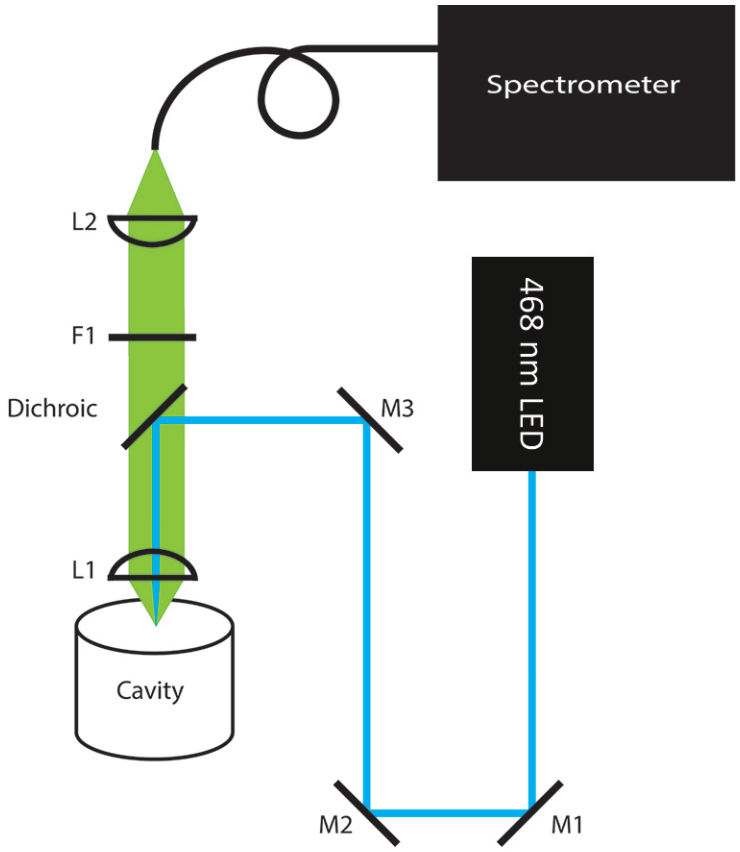

Figure 5.5: Schematic of the optical system use for fluorescent emission cavity-enhanced spectroscopy. Here, L1 and L2 are aspheric condenser lenses and F1 is a longpass filter.

5 mW light emitting diode (LED) (Radio Shack #276-316) centered around 468 nm served as the excitation source. The output of the LED was bandpass filtered to limit its inherently broad spectrum. A 490 nm dichroic mirror (Semrock Di02-R488) angled at 45°was used to direct the excitation light to a 20 mm focal length aspheric condenser lens (ThorLabs ACL2520). This allowed for delivery of approximately 420 μW of light into the integrating cavity. The fluorescence emission was collected by the same condenser lens, and filtered via a 500 nm long pass filter (Semrock, USA) before being imaged to a fiber bundle using a matching aspheric condenser lens (Thorlabs). The fiber bundle was coupled into an Acton 0.300m charge-coupled device (CCD) spectrometer. The CCD was thermoelectrically cooled to -70°C to minimize electrical noise. The entrance slit was set to 200 μm for all spectra collected.

A stock solution of urobilin was prepared by dissolving 1.1 mg of urobilin hydrochloride (Frontier Scientific) into 20 mL of ethanol. This solution was then diluted down to a concentration of 1 μM urobilin by the addition of more ethanol. 11.25mg of zinc acetate was added to the solution to allow for phosphor formation. Samples were prepared from the stock solution, ranging from 100 nM to 500 fM. This was done by successive dilutions by a factor of 10 from the stock solution. Due to detection limitations, the final dilution was only by a factor of 2. Five sets of dilutions were preformed to account for variation in the effective concentration of the samples due to the technique used to prepare samples. Equal volumes of solution were used for all fluorescence measurements taken.

5.2.3 Results

A fluorescence spectrum was recorded for the stock solution of 1 μm urobilin. A photograph of this was taken and is shown in Fig. 5.6. Here, a green band of light can be observed escaping between the two cavity halves. During data acquisition, the

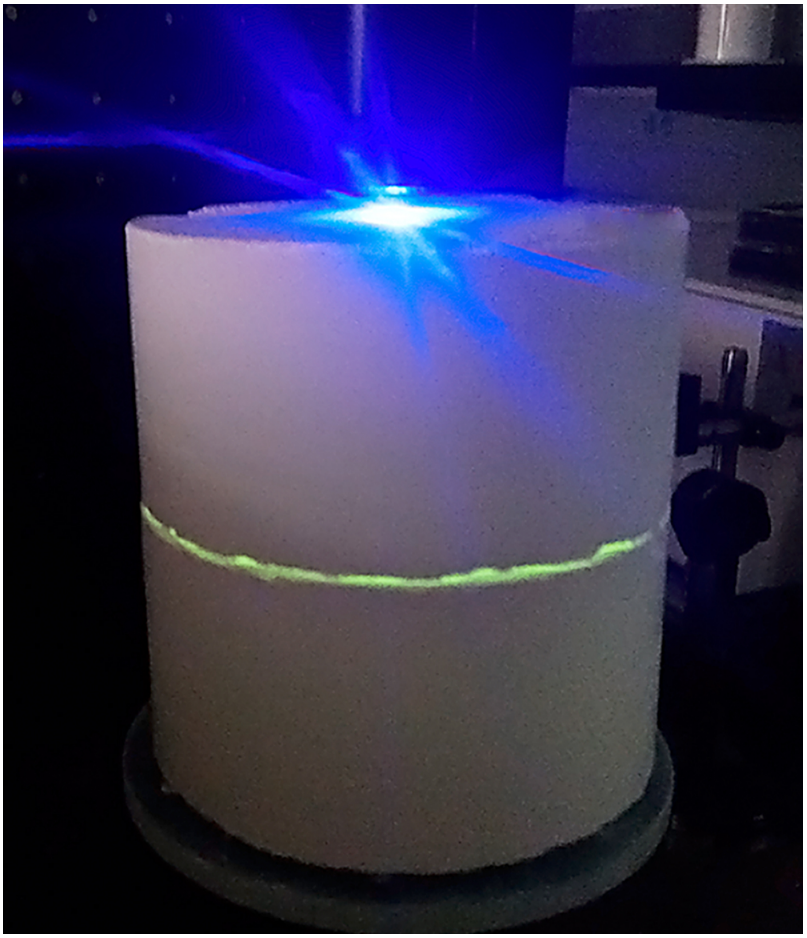

Figure 5.6: Photograph of integrating cavity during use. The excitation (blue light) can be seen entering the cavity. The green band visible is the fluorescent emission generated from a high concentration of urobilin in solution. During data acquisition, the cavity halves were clamped together to prevent light loss from this seam.

cavity halves were clamped together to prevent light loss from this seam. It should be noted that this photograph was processed after it was acquired to minimize the glare due to the blue excitation light and to highlight the green fluorescence emission.

Fluorescence spectra were recorded for concentrations ranging from 100 nM to 500 fM, where the typical excitation and emission spectra are shown in Fig. 5.7. In addition, a emission spectrum of the empty cavity and of the ethanol buffer were

collected and used for post processing and background removal. Integration times of 100 ms were used for the 100, 10, and 1 nM concentrations, and an integration time of 500 ms was used for all other concentration. Fig. 5.8 shows the measured fluorescence signal for each concentration. The intensity value for each concentration was calculated by integrating the area under the emission curve following removal of the cavity and ethanol background. Five spectra were taken for each concentration and averaged. Because spectrometer settings (i.e. integration time) had to be adjusted for lower concentration, the data was corrected to reflect this. Fluorescence signal above the background was detected for urobilin concentrations down to 500 fM. Even at this concentration, sufficient signal remaining to indicate the potential for single femtomolar detection, without the need for expensive laser sources. In addition, measurements can be taken in near real-time, as integration times below one second were sufficient for all samples.

Photobleaching did not seem to impact the measured fluorescence spectra for the urobilin phosphor complex. To test this, spectra were acquired over several minutes with the excitation source on and coupled into the cavity. No significant change in intensity was observed during this time duration. For sensing based applications with fluorophores that are susceptible to bleaching, care must be taken to trigger the excitation source such that the samples are not bleached prior to data acquisition.

5.2.4 Discussion

In summary, we demonstrate detection of sub-picomolar concentrations of urobilin in solution, via the use of an integrating cavity to enhance the excitation and aid in the collection of fluorescence emission from a sample. By placing the sample to be probed into an integrating cavity, isotropic illumination allows for fluorescent signal to be generated from the entire cavity volume. If larger volumes of sample

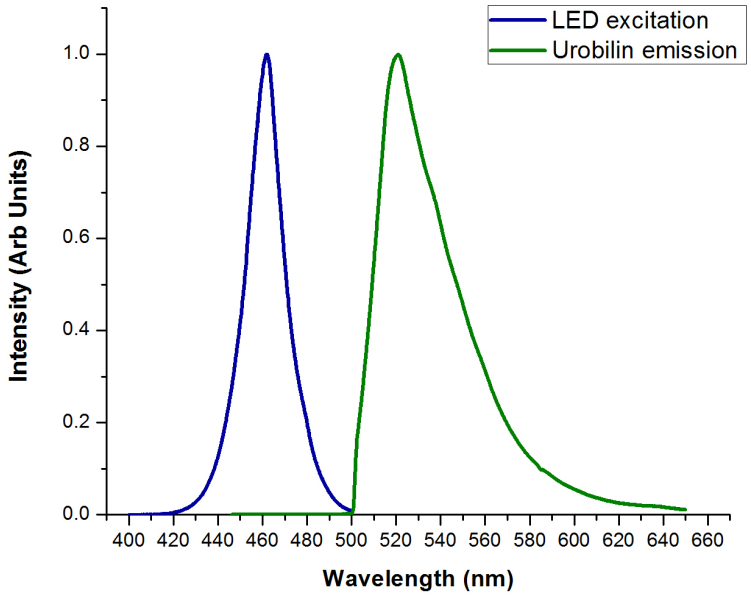

Figure 5.7: Excitation and emission spectrums for the LED and urobilin fluorescence. The blue trace shows the LED emission after it was bandpass filtered. The green traces shows the typical fluorescence observed from the cavity.

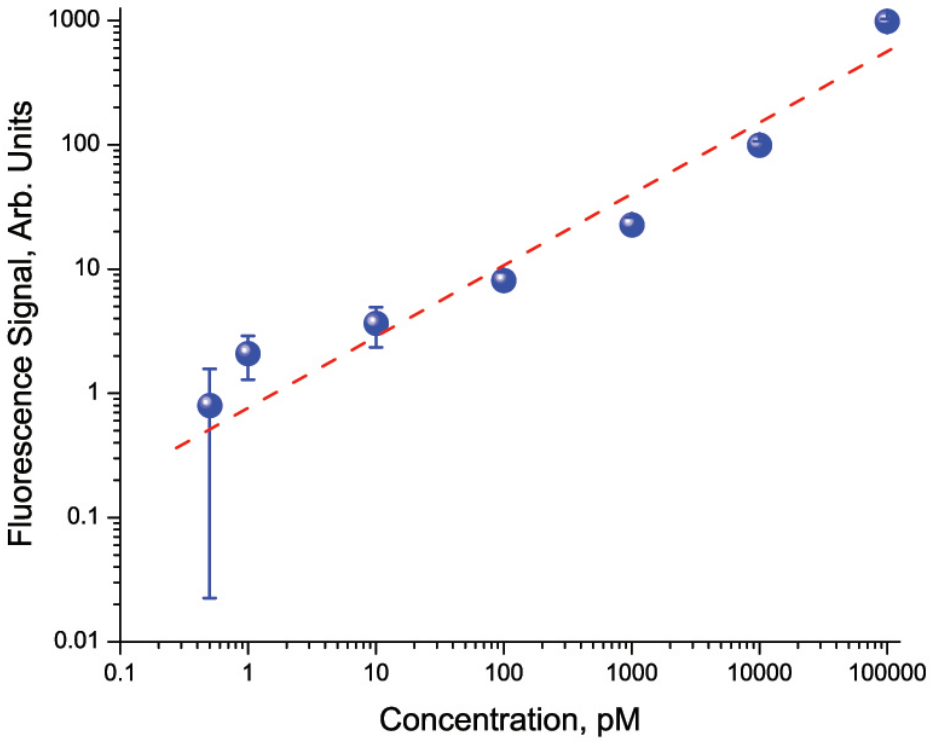

Figure 5.8: Fluorescence counts plotted against concentration following cavity and ethanol background removal and correction for varying acquisition times on the spectrometer. The blue dots indicate the average fluorescence intensitymeasured for each concentrationwhere the error bars represent SD between samples. The red dashed trace shows a linear fit to these data, indicating the potential for detection of even lower concentrations.

were placed inside the cavity, it is possible the detection limits could be pushed even lower. Additionally, careful filter of the emission could allow for the use of photodiode based detection. In this case, fewer numbers of photons would be required for detection. Detection limits would then be based on the ability to distinguish signal generated from a sample from the cavity background. The elastic scattering of the cavity walls limit energy lost inside the cavity, thus allowing for collection of a larger percentage of the diffuse emission. Significant enhancement can be achieved over conventional epi-illumination system even with the use of an extremely inexpensive excitation source such as a single LED. This technique has tremendous potential for analysis of global drinking water supplies, particularly in developing nations and following natural disasters, where sophisticated laboratory equipment many not be available.

5.3 Utilizing Increases in Scattering to Further Enhance Integrating Cavity Enhanced Spectroscopy

5.3.1 Background

Having access to clean air and water is paramount for human health. It is estimated that pathogens found in water result in more than 2 million deaths annually.[1] Additionally, many industrial pollutants, such as the incomplete burning of fossil fuels found in industrial exhaust can present carcinogenic hazards to the populations around those industrial facilities. A particular concern is the increasing contamination of fresh water systems, where more than one-third of the accessible and renewable freshwater systems are used for industrial and agricultural applications. Pollution from these sources leaves water contaminated with numerous synthetic and geogenic compounds.[106] Natural disasters can also present situations where quick and sensitive screening of water sources is critical for the health of the population

affected.[107,108]

Modern analytical techniques, such as liquid chromatography and mass spectroscopy, are quite powerful in detecting trace contaminates and are considered the gold standard for detection. Despite this, these techniques remain costly to perform and require significant time from sample collection to results as samples collected in the field must be sent off to a laboratory for analysis. These limitations here lead to the development of fluorescence emission cavity enhanced spectroscopy.[84] Here, trace contaminants of human and animal waste in water were detected utilizing urobilin fluorescence.[113–117] This technique provides significant enhancement compared to the results obtained using a traditional imaging system for detection. The enhancement stems from two major factors afforded through the use of an integrating cavity. First, the isotropic nature of the integrating cavity results in the entire sample volume being probed, providing enhancement simply due to a larger interaction volume of the excitation source with the sample. Second, as the cavity walls are highly reflective to both the excitation radiation and the fluorescence emission, signal generated is more efficiently collected from a full solid angle as a substantial portion of the emission will escape via a controlled exit point in the cavity. Cavity based spectroscopy, such as integrating cavity ring-down spectroscopy, has a wide variety of other applications, including a means to measure absorption coefficients of biological material and water[70,85,120] and single-cell detection.[121]

In this report, we present a simple method to further enhance the fluorescence signal generated inside of an integrating cavity. By introducing additional elastic scattering to the sample volume being probed to increase the average path length through the sample, fluorescence generation from the volume is further enhanced. The enhanced signal generation could lead to even lower detection limits for fluorescence based integrating cavity spectroscopy.

5.3.2 Materials and Methods

In order to test the effects of adding scattering to fluorescence generation inside an integrating cavity, a stock solution with 8 μL 8-hydroxypyrene-1,3,6-trisulfonic acid (HPTS) used as a fluorescent dye in 40 mL of ethanol was prepared, resulting in a concentration of 16.4 μM of HPTS. A second solution consisting of 9.4 mg of titanium dioxide (DuPont Ti-Pure R-931) suspended in 40 mL of ethanol and 8 μL of HPTS was prepared, having an identical concentration of HPTS to the first solution. HPTS, also known as pyranine, has been used as a fluorescent indicator for intracellular pH and has an excitation maximum at 454 nm, and emission maximum at 520 nm when dissolved in a solution with pH 7.0. HPTS has a absorption cross section of 9.176×10^{-14} cm^2 at 454 nm. The quantum yield of this dye is near 1.0 when dissolved in both acidic and basic solutions.[122] Titanium dioxide was selected due to its minimal absorption in the visible, as well as the fact that it suspends well in solution. The TiO_2 particles used had an average diameter of 0.55 μm, and an assumed Mie scattering cross section of 0.5721 μm^2.

From these two solutions, sample solutions were prepared where the only variable was the concentration of TiO_2. The total volume of each sample was set to be 5 mL. Scattering coefficients were calculated for each solution using a Mie scattering calculator.[123] This calculator uses expressions for Mie scattering found in Bohren and Huffman's book.[124] The values for scattering coefficients reported here only contain the contribution from the added TiO_2, thus the solution consisting of only dye and ethanol is considered to have a negligible scattering coefficient. Due to the particle size of the TiO_2, the anisotropy parameter, g, was calculated to be 0.52. Each sample was then placed inside a custom made integrating cavity made out of fumed silica powder. Details of the cavity construction are more thoroughly discussed in.[81,84,125]

density	4.23 g/cm^3
index of refraction (n)	2.609
particle size	0.55 μm
concentration of spheres in solution	7.98e^{-5} part/μm^3
anisotropy (g)	0.52
scattering coefficient	0.46 cm^{-1}
scattering mean free path	2.17 mm

Table 5.1: Mie scattering calculations for DuPont Ti-Pure R-931 TiO_2. Parameters entered into the calculator are shown on the top half of the table, while the outputs of the calculator are shown in the bottom half.

The mean particle size, along with index of refraction, and concentration of particles in the stock solution are listed in Table 5.1. The scattering coefficients for all sample solutions as a function of volume fraction of TiO_2 are shown in Table 5.2.

A 100-mW, 473-nm diode pumped solid state (DPSS) laser was used as the excitation source for these experiments. A schematic of the optical system is shown in Fig. 5.9(A) along with an illustration of the integrating cavity with a sample inside shown in Fig. 5.9(B). The integrating cavity was designed to be a right circular cylinder with an inner diameter and height both of 2.5 inches. The excitation light was reflected off a dichroic beamsplitter (Semrock Di02-R488) and gently focused into the cavity using an aspheric condenser lens (Thorlabs ACL2520). The fluorescent emission was collected using the same lens, and imaged to the tip of a fiber bundle coupled into an Acton 0.3-m CCD spectrometer (Princeton Instruments). A long pass filter (Semrock BLP01-488R) was used to remove any additional excitation light which passed through the dichroic. All spectra were recorded with an integration time of 5-ms on the CCD.

Volume fraction	μ_s
0.0	0
0.05	0.023
0.1	0.046
0.15	0.069
0.2	0.092
0.25	0.115
0.3	0.138
0.35	0.161
0.4	0.184
0.45	0.207
0.5	0.23
0.6	0.276
0.7	0.322
0.75	0.345
0.8	0.368
0.9	0.414
1.00	0.46

Table 5.2: Scattering coefficients as a function of volume concentration.

5.3.3 Results and Discussion

The fluorescent spectra for each scattering coefficient are shown in Fig.5.10. From this data, it can be seen that as the scattering coefficient of the solution increase, so does the measured fluorescent intensity until a point at which the solution becomes too highly scattering and light cannot fully penetrate into the entire sample volume. This can be seen from the spectra from the samples with the highest scattering coefficient, where the peak intensities for both begin to show a downward trend. Integrations of these traces plotted against the scattering coefficient are shown in Fig. 5.11, where the blue points correspond to the range of scattering coefficients which result in an increase in detected fluorescence intensity and the red points correspond to the solutions where the intensity began to drop. It should be noted

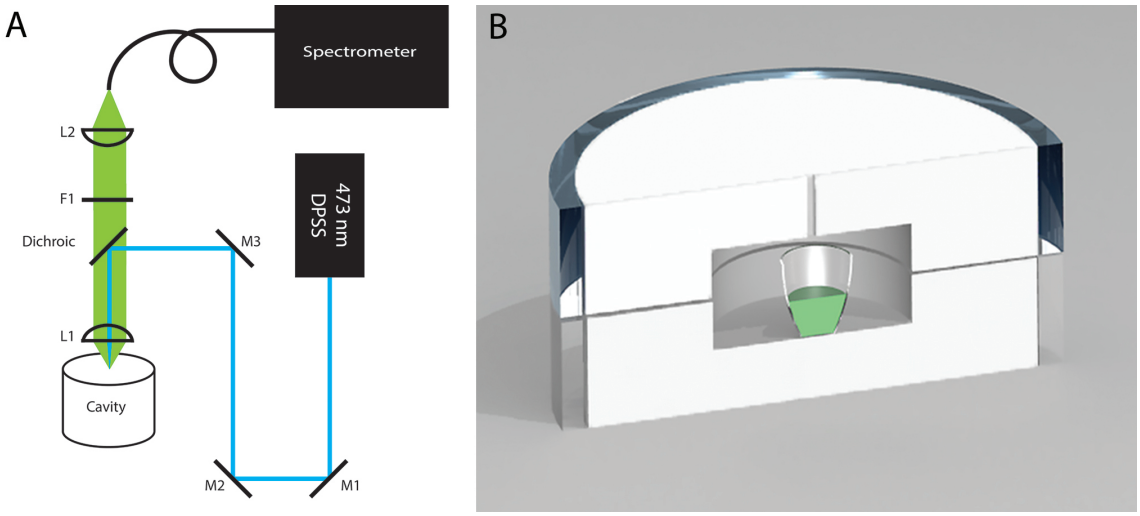

Figure 5.9: (A) Schematic of optical system for fluorescence emission cavity enhanced spectroscopy. (B) Illustration of the integrating cavity with a green fluorescent sample placed inside of the cavity. Here light would be coupled into the cavity through the channel shown directly above the crucible. The gap between the two cavity halves would be sealed during data collection, and is only shown here to more clearly depict how the two cavity halves.

that the narrow peaks in the emission spectrum are contributions from the Raman scattering of ethanol.

The enhancement in fluorescence is related to the increased path length of light inside the sample due to the added elastic scattering. This has previously been shown for Raman enhancement in a highly scattering media.[25] The added path length, or dwell time, for photons inside the scattering media was shown to be capable of producing an enhancement in Raman scattering. Just as was observed with the addition of scattering to the fluorescent sample, in the case of too much scattering, the Raman enhancement decreased due to the fact that a large portion of the incident beam is scattered out of the sample near the surface. Photons that do penetrate into the sample tend to have longer path lengths inside the sample, but these competing effects eventually compensate for each other, resulting in no further enhancement.

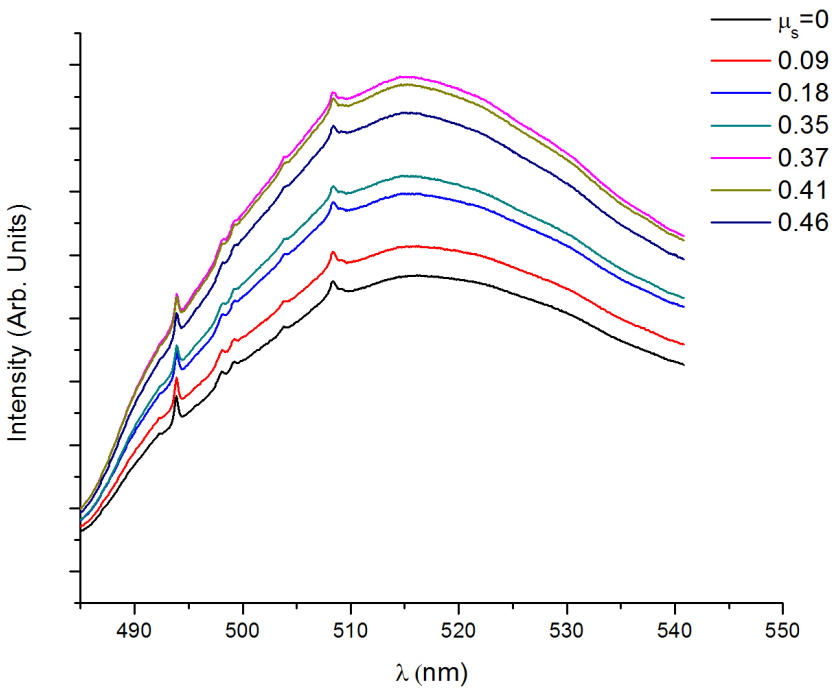

Figure 5.10: Measured fluorescence emission spectrum for solutions with varying scattering coefficient. The traces for s = 0.41 and 0.46 show a decrease in intensity.

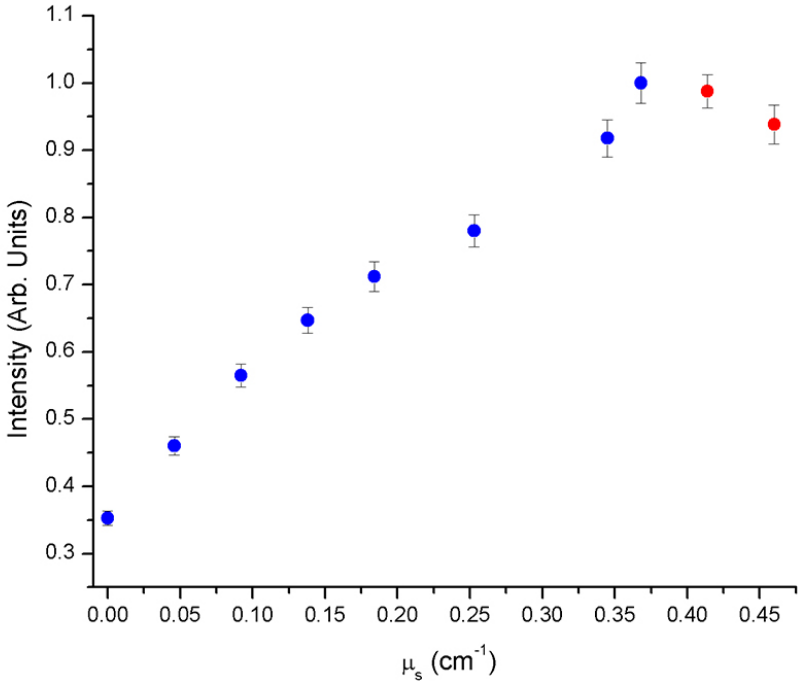

Figure 5.11: Integration of the fluorescence emission intensity as a function of scattering coefficient.

As fluorescence emission is a linear optical process just like spontaneous Raman scattering, we would expect these two optical processes to behave the same under additional scattering which is confirmed by the data presented here.

5.4 Conclusions

Integrating cavity enhanced spectroscopy can be a powerful tool for analysis of liquid and gaseous samples. We have shown a simple technique that can be used to further enhance the fluorescence signal generated inside an integrating cavity. Further work utilizing Monte Carlo simulations could help elucidate the optimal amount of scattering to introduce to a sample, depending on the particle size used, to maximize the generated fluorescence signal. This simple method has the potential to further enhance the detection limits of integrating cavity spectroscopy without adding any significant cost or complexity to the system. Careful calibration and accurate knowledge of the additional scattering introduced to a sample would be required for quantitative analysis using this technique. Regardless, this method had tremendous potential in sensing applications where the identification of a contaminant's presence in solution is the desired end goal.

5.5 Summary

Integrating cavity enhanced fluorescence spectroscopy can provide enhancement factors of 10^3 or greater in detection sensitivity. This enhancement comes from the large volume that can be simultaneously probed, when compared to a traditional fluorescence microscope. Additionally, the long pathlength inside the cavity allows for photons to interact with the fluorescent sample multiple times, increasing the likelihood of absorption and remission via a fluorescence or phosphorescence transition. This technique was demonstrated for detection of urobilin fluorescence. Further enhancement can be achieve by adding a suspended scatterer to the sample, particular

for the case where the scattering particles do not have significant absorption for the excitation wavelength.

The enhancement provided by an integrating cavity could be reduced if the fluorophore of interest easily photobleaches. Traditionally, photobleaching is overcome by stirring or agitating a sample to ensure unbleached flourophores enter the excitation volume. Since the entire sample volume is excited simultaneously, it is possible to bleach the entire sample.

Despite this, there are numerous additional applications where integrating cavity enhancement could greatly benefit detection sensitivities. Such applications include water quality monitoring by looking at the fluorescence of dissolved organic material using UV excitation, increasing the detection sensitivity of fluorescence based immunoassays, and increasing sensitivity of heavy metal sensing from synthetic biology based fluorescence.[47,126,127]

6. ALTERNATE INTEGRATING CAVITY DESIGNS

6.1 Introduction

Up until this point, all integrating cavities discusses have been constructed using the same basic principles. Two cylinders are manufactured by packing fumed silica powder into a mold, and material is then removed via standard machining techniques to create a cavity. These two cylinders are then stacked on top of each other for spectroscopy. While this cavity design has been shown to be quite effective in providing significant enhancement, there is virtually no control of the composition of the gases inside of the cavity, as atmosphere will always fill this area. This Chapter will focus on cavity design that can allow for careful control of the gases inside, thus allowing for Raman spectroscopy to be preformed on isolated gas samples.

Additionally, we will discuss other potential diffuse reflectors that can be used to manufacture integrating cavities. While fumed silica has been shown to have the highest diffuse reflectivity of any known material, several other materials such as white quartz and barium sulfate offer a diffuse reflectivity that could be sufficient for many applications, particularly with regard to fluorescence enhancement. This is because one of the main gain mechanisms for fluorescence spectroscopy is simply the larger volume that is probed, and thus maximum reflectivity is not entirely critical for all applications. White quartz is a much more robust material in the sense that it would be more durable, and is currently commercially available and can be manufactured to various design specifications.

Finally, we will discuss future directions for integrating cavity enhanced spectroscopy. Much of this work was done as a proof of concept, and there is room for additional improvement in cavity optimization and signal collection and detection.

6.2 Flow Through Integrating Cavity

In order to control the gas concentration inside of an integrating cavity, two methods were employed. In the first of these techniques, an integrating cavity was designed and constructed such that fumed silica walls could completely surround a inner quartz cell. This cell was equipped with an inlet and outlet port, such that gas could be flowed in and out of the inner cell. This method could allow for slight pressurization of the inner cell, which would increase the number of molecules inside of the cavity resulting in a stronger signal. As long as the pressure inside of the cell was known, the Raman intensity could be correlated with a concentration.

Fig. 6.1 shows a cross sectional view of the flow through integrating cavity designed. Fumed silica powder was packed into two quartz cylinders, labeled here as the outer mold. These pieces were manufactured identically to those previously described. The inner volume of the cavity was created by an end mill. In addition to the aperture used to couple light into and out of the cavity, two additional through holes were drilled into the cavity halves. These were added to allow for the inlet and outlet stems to protrude from the fumed silica walls. Quartz plates were placed on the top and bottom of the cylinder and included holes that fit the inlet and outlet stem. A 1.5 inch hole, labeled light coupling port in Fig. 6.1, was added to the top plate. This was placed to allow for the collection optics to be moved as close as possible to the entrance aperture of the cavity.

To measure Raman signal from this cavity, 532 nm light from a 15W Spectra Physics Millennia eV was coupled into the cavity using a dichroic mirror (Semrock Di02-532LP) mounted at 45° and a aspheric condenser lens (Thorlabs) with focal lenght of 20 mm. Raman emission passed through the dichroic and was further filtered by a 532 nm notch filter (Thorlabs) before being imaged to a 1 mm multi-

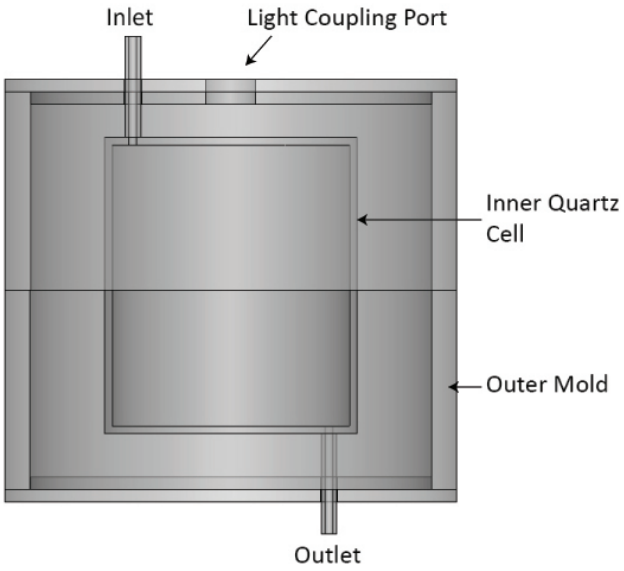

Figure 6.1: Cross section view of the flow through integrating cavity design for liquid or gas analysis. The space between the inner quartz cell and the outer mold is filled fumed silica powder.

mode optical fiber. Spectra were acquired with the laser power set to 800 mW, which was the lowest setting possible. A Andor Shamrock 303i spectrometer with a iDus DU420A CCD was used for detection. The entrance slit was set to 10 μm and an integration time of 30 μs was used for all spectra collected. Fig. 6.2 shows a photograph of the flow through cavity with 532 nm light coupled in.

The laser power was varied from 800 mW to 15 W to attempt to measure the Raman spectrum of atmosphere. Regardless of input power, no Raman peaks were observed. This is caused by two issues. First, the cavity reflectivity is decreased proportional to the fraction of surface area removed for the inlet, outlet, and light coupling ports. With the additional of these second and third hole, the reflectivity decreased compared to previous cavity designs, resulting in a greatly reduced path-length. Second, the additional of a large volume of quartz into the integrating cavity

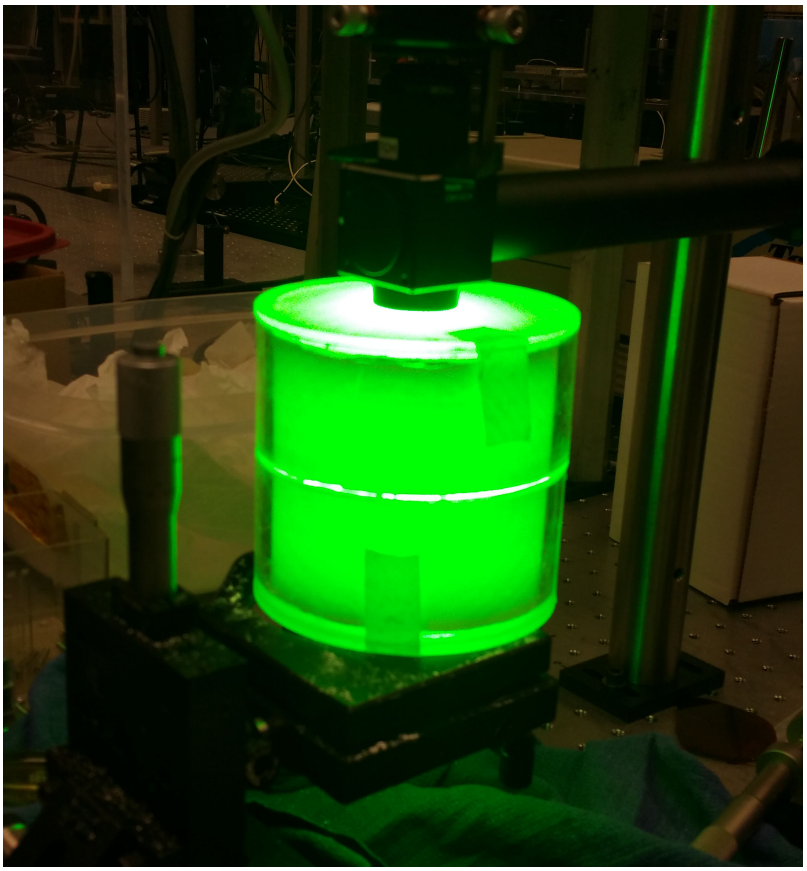

Figure 6.2: Photograph of the flow through integrating cavity with an inner quartz chamber.

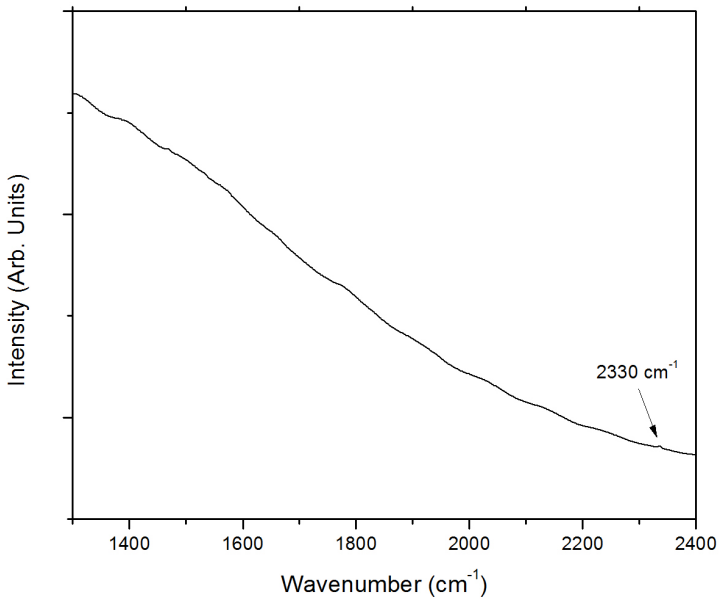

Figure 6.3: Plot of spectrum from flow-through integrating cavity design. The fluorescence dominates any siganl, and only a small peak can be seen at 2330 cm^{-1} corresponding to nitrogen.

resulted in an increase in the cavity background. This signal overwhelms the weak nature of spontaneous Raman scattering. Furthermore, 4% of the input light is lost to Fresnel reflections from the inner quartz cell.

Fig 6.3 shows the spectrum acquired for the first flow-through cavity design. The background fluorescence from the quartz piece inside of the integrating cavity dominates all signal. Only a very small peak is able to be seen at 2330 cm^{-1} corresponding to nitrogen. This spectra was acquired with 800 mW of 532 laser power, 125 ms integrating time, and 500 accumulations. Even with 15W coupled into the cavity, no peak could be seen at 1556 cm^{-1} for oxygen.

To overcome the losses in cavity reflectivity and the increases in background from the inner cell, we can simply change the design of the system to place an integrating

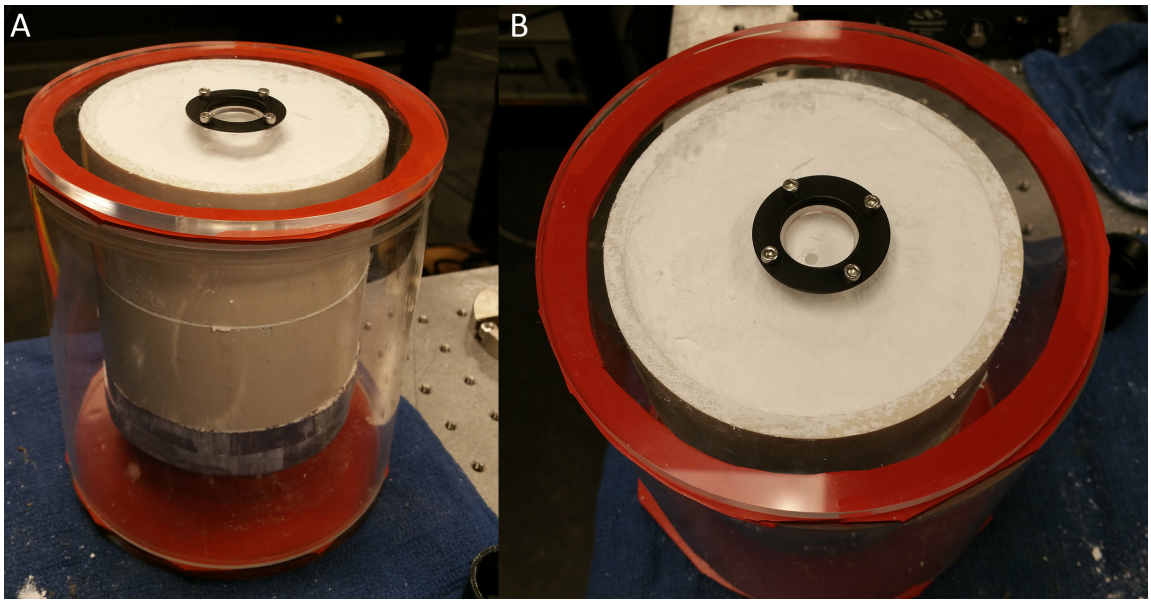

Figure 6.4: Photos of integrating cavity inside of a gas cell. (A) Photo of a side view of the gas well with integrating cavity inside. (B) Photo of the top of the gas cell. The optical window can be seen in the center of the lid.

cavity inside of a gas cell, as opposed to placing a gas cell in side of a cavity. This same issue has limited detection sensitivities in cavity ring-down based spectroscopy where the losses due to a gas cell placed inside an optical cavity decreased the sensitivity of the system too substantially.

A gas cell was constructed from acrylic materials. Tubing with a 6 inch inner diameter was cut to a length of 6 inches. A rubber gasket was placed on the bottom of the cylinder before a acrylic plate was attached with #6 screws. A 1 inch hole was bored into the top plate and sealed with a 1 mm thick UV Fused silica optical window with anti-reflection coating for 300 nm to 700 nm (Thorlabs). A rubber gasket was again used to seal this from the external environment. Inlet and outlet ports can be added to the top or bottom acrylic plates to allow for pressurization, although the 1 mm thick optical window will limit the pressure difference that can

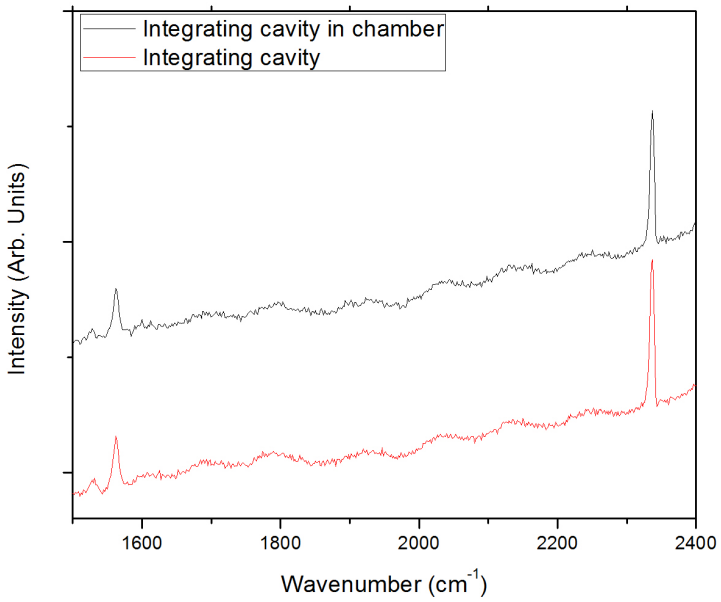

Figure 6.5: Plot of the Raman spectrum of atmosphere for an integrating cavity placed inside a gas chamber compared to an integrating cavity alone. The black trace shows the Raman spectrum of atmosphere from an integrating cavity placed inside a gas chamber. The red trace shows the Raman spectrum for atmosphere from the same integrating cavity alone. These spectra were offset for ease in viewing.

be achieved. Fig. 6.4 shows photographs of top and side views of the gas cell with an integrating cavity inside. The cell is clamped together during spectroscopy. Fittings with rubber gaskets can be inserted into the top of the cell to allow for air flow into and out of the cavity.

To test this integrating cavity design, the same optical setup described above was used for Raman spectroscopy. Raman spectra were acquired with 800 mW of 532 nm laser power from the Millennia eV. The spectrometer has a slit width of 10 μm and an integration time of 30 μs. 50 accumulations were acquired for any spectrum.

The Raman spectra of atmosphere for an integrating cavity placed inside the gas

cell, and for the same integrating cavity alone, are shown in Fig. 6.5. The spectra in this plot were offset for ease in viewing only. The spectra shown are not smoothed, and the background has not been subtracted. The oxygen and nitrogen peaks can easily be seen at 1556 cm^{-1}, and 2330 cm^{-1}, respectively. The peak intensities are approximately 8% lower for the spectra recorded with the integrating cavity placed inside the gas cell. The spectra in the plot are for a single detection with an integrating time of 30 μs.

6.3 Alternate Diffuse Reflecting Materials

6.3.1 Barium Sulfate

Barium sulfate has been used in several commercial diffuse reflectors such as Spectraflect®. Typically, barium sulfate has is mixed with a binding agent forming a paint or coating which can be applied to other substrates. This results in a durable diffuse reflective coating, but the absolute reflectivity is often only $> 98\%$. Spectraflect is often applied to surfaces that have been roughened with techniques such as sand blasting.

Pure barium sulfate itself can be used as a diffuse reflector. This material has very minimal absorption in the visible, and can be purchased in very pure forms. It is highly scattering, and this in itself can be used to enhance Raman scattering.[25] This enhancement can be used to generate a laser which uses stimulated Raman scattering as its gain mechanism.[128] While the BRDF has been measured for barium sulfate based coatings,[129] the scattering distribution has not been measured for pure barium sulfate to the best of this authors knowledge. One could still anticipate nearly Lambertian behavior from a barium sulfate cavity, as coatings made using this chemical exhibit such behavior. Despite this, barium sulfate can be packed using similar techniques to fumed silica to manufacture integrating cavities.

Barium sulfate based integrating cavities have several advantages over fumed silica for the construction of integrating cavities. The material is relatively low cost to purchase at high purities ($> 99\%$). One significant advantage for barium is the decrease in cavity background seen from this material. Barium sulfate has several strong Raman lines which will be present in any spectroscopy done inside such a cavity. But these lines are relatively narrow and well known in location. Thus, these lines can easily be subtracted out of any measured Raman spectrum, so long as the barium sulfate peaks do not overlap the Raman shifts of the sample that is being analyzed. Barium sulfate also does not take on water like fumed silica, allowing cavities made from this material to maintain high reflectivity over time.

A barium sulfate cavity was constructed using the similar techniques described in Chapter 3. Construction of these cavities is simpler in that pre-baking of the powder is not needed, and sintering after packing also does not need to occur. Because of these things, barium sulfate cavities can be constructed using relatively cheap molds. The cavity constructed here was made using a section of 4 inch inner diameter PVC pipe. Barium sulfate was packed into two cylinders of the PVC at a pressure of 4000 PSI. The cavity volume was then machined out using the same milling technique as is done with fumed silica. A small through hole with a diameter of approximately 1 mm was added to one of the cavity halves to couple light into and out of the cavity. A photo of this cavity with 532 nm laser light coupled in is shown in Fig. 6.6.

To test the effectiveness of this material, a Raman spectrum of oxygen was obtained using a 532 nm Spectra Physics Millennia eV laser with maximum output of 15W. Excitation light was directed into the integrating cavity via a dichroic beamsplitter (Semrock Di02-532) that was mounted at 45° and a aspheric condenser lens with focal length of 20 mm (Thorlabs). The Raman signal was filtered by a 532 nm notch filter (Thorlabs) before being imaged to the tip of a 1 mm core multimode

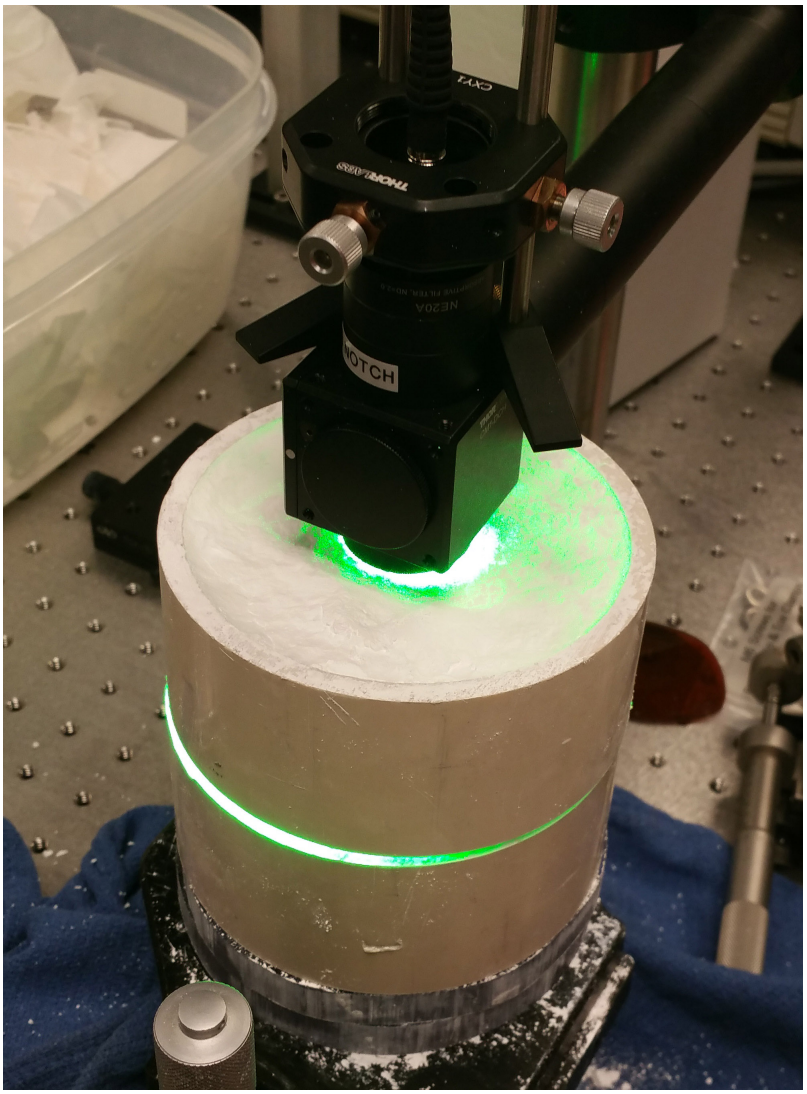

Figure 6.6: Photo of a barium sulfate intergrating cavity with 532 nm laser light coupled into it.

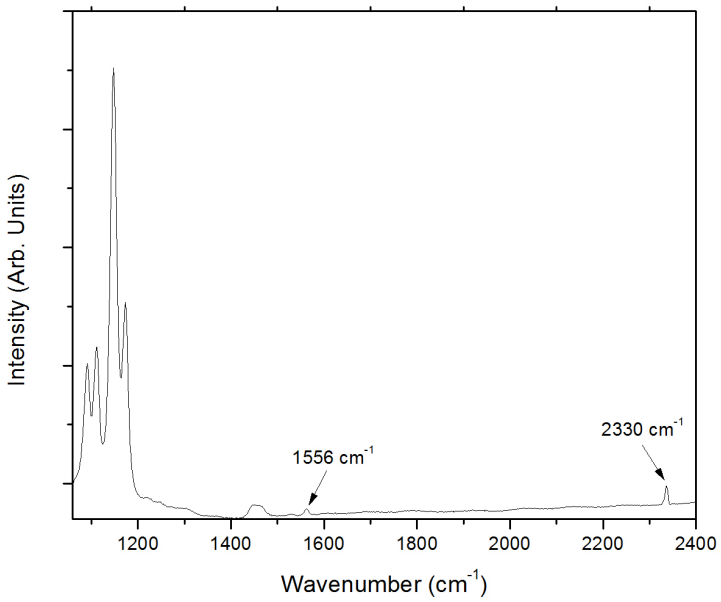

Figure 6.7: Plot of the Raman spectrum of atmosphere inside of a barium sulfate integrating cavity

fiber. This fiber was then imaged to the entrance slit to an Shamrock 303i spectrometer with a iDus DU420A CCD detector that was TE cooled to -52 °C (Andor). The spectrometer featured a grating turret with a 600 lines/mm, 1200 lines/mm, and 1800 lines/mm grating, allowing for a maximum spectral resolution of 0.12 nm. Raman spectra for atmosphere were collected from the barium sulfate cavity with a integration time of 30 μs and the entrance slit for the spectrometer set to 10 μm. The laser power was set to 800 mW, the lowest output power available. Spectra were acquired for a total of 100 accumulations, but Raman peaks were easily visible for a single shot.

The Raman spectrum of the empty barium sulfate cavity is shown in Fig. 6.7. The Raman shift for barium sulfate can be seen below 1200 cm^{-1}. Much like the

oxygen or nitrogen lines can be used for normalization, this Raman shift could also be used for the normalization of a dataset collected inside this type of cavity, so long as this line does not saturate the detector used. The background of the barium sulfate cavity is significantly reduced as compared to the background from fumed silica. This is even the case for relatively low purity barium sulfate with a purity of 99%. Purities of 99.99% are commercially available, but at significantly higher cost. The laser power delivered here was a factor of 5 greater than that of the source used for the 532 nm Raman spectroscopy detection limit study, but the integration times were a factor of 6000 shorter than those previously used. It is difficult to compare the relative intensities of the signals measured between these two optical systems, as the iDus CCD used in conjunction with the Shamrock 303i has a higher quantum efficiency than the CCD found in the Acton 0.300m spectrometer. Additionally, the spectrometers themselves could have different efficiencies caused by internal alignment.

It is visually apparent that significantly less light is lost out of the cavity walls for the barium sulfate cavity as compared to the fumed silica. It should be noted that the barium cavity was packed using white PVC piping, so only the top surface can be used for comparison. Regardless, significantly less green light is seen at around the circumference of the top of the barium cavity. Future work is needed to more quantitatively compared the two materials with measuring cavity ring-down times for barium sulfate, along with measurements of its BRDF. Additional work is also needed in optimizing the manufacturing process for barium based cavities. Nonetheless, this material has exciting potential for cavity enhanced spectroscopy.

6.3.2 White Quartz

White, or opaque, quartz is another material that makes for an excellent diffuse reflector. This material is manufactured with evenly distributed, micron-sized pores, providing a similar glass-air interface seen with the fumed silica. White quartz manufactured by Heraeus Quartzglas was tested for diffuse reflectivity using an optical parametric oscillator to deliver tunable nanosecond pulses of light. The optical setup used was identical to the system described in Chapter 3, Section 3.5. A integrating cavity was made from a white quartz cylinder and two white quartz plates. The wavelenght dependent ring-down times and corresponding reflectivity measurements from this test are shown in Table 6.1. The published reflectivity values for Spectralon are shown in the right most column of Table 6.1.

While the reflectivity values here are significantly lower than fumed silica in terms of absolute reflectivity, they are still higher than the current commercial standard in absolute diffuse reflectance. This material has significantly higher material strength and durability than an integrating cavity made from packed quartz powder. Additionally, this material is not hydrophilic like fumed silica, and should not suffer from decreases in reflectivity over time due to the absorption of water. There is also the potential to clean a cavity made from this material if a sample comes into contact with the cavity walls.

The durability and commercial availability of this material make it promising for cavity enhanced spectroscopy, particularly for applications such as fluorescence enhancement where excitation of a large volume alone offers increased sensitivity. One area of fluorescence based detection that could benefit from cavity enhancement is with fluorescence based immunoassays. For competitive immunoassays, the level of detection strongly depends on the antibody concentration.[131] Generally, a low

Wavelength (nm)	Decay Time (ns)	Diffuse Reflectivity	Spectralon
410	29.88	0.99402	0.991 (400 nm)
420	30.03	0.99405	
440	30	0.99404	
460	29.84	0.99401	
480	31.25	0.99428	
500	32.8	0.99455	0.991
520	33.22	0.99462	
540	32.44	0.99449	
560	33.15	0.99461	
580	32.62	0.99452	
600	33.19	0.99461	0.992
620	31.77	0.99437	
640	32.14	0.99444	
660	31.98	0.99441	
680	32.19	0.99445	
700	31.97	0.99441	0.992

Table 6.1: Diffuse reflectivity of white quartz from 410 nm to 700 nm. Reflectivity values for Spectralon, the current industrial standard for diffuse reflectance, are shown on the right most column for reference. This data was generously provided by John D. Mason and has been submitted for publication in Applied Optics.[130]

level of detection is achieved by keeping the antibody concentration low, but this also generates low signal. Methods that could generate increased fluorescence signal could allow for decreases in the levels of antibodies used, thus further reducing the detection sensitivity of competitive immunoassay based sensing.[47]

7. SUMMARY AND FUTURE DIRECTIONS

7.1 Summary

This work severs the purpose of exploring the use of integrating cavities for Raman and fluorescence sensing applications. Integrating cavity constructed from fumed silica powder offer the highest diffuse reflectivity of any known material. The Lambertian nature of the cavity walls results in a near isotropic field inside. The high reflectivity affords a long optical pathlength for light coupled into the cavity. These features combine to allow for significant enhancement of Raman scattering and fluorescence emission. Additionally, these cavities can be used for highly sensitive measurements of the absorption coefficients of materials, particularly in the case where scattering dominates absorption. This is because light that scatters from such a sample is not lost from the cavity, and thus only of absorption of the input light by a sample is detected.

Raman enhancement for gas detection was demonstrated by first collecting Raman spectra for atmosphere inside of an integrating cavity. The nitrogen and oxygen lines can easily be observed, and can provide useful information for trace molecule detection. If the cavity is filled with atmosphere in addition to the molecule of interest, these lines can be used as a reference to for normalization. By correction for differences in cavity alignment or coupling efficiency, accurate quantitative studies can be performed.

This was demonstrated with the detection of trace quantities of three PAH's. First, using 532 nm excitation, detection of pyrene, benzo(a)pyrene, and naphthalene in the micromolar concentrations was shown to be possible. Linear fits of the concentration of PAH vs. Raman intensity demonstrate the quantitative nature of

this technique, provided adequate calibration exists. Since the Raman cross-section scales as a function of $1\lambda^4$, the use of a 473 nm laser source allowed for decreasing the detection limits. Concentrations of pyrene down to 37 nM were detected in the integrating cavity. Based on the linear fit to a concentration vs. intensity curve, and the cavity background, the theoretical detection limit for pyrene from this system is 13 nM at a 3σ level.

Enhancement of fluorescence based sensing was then demonstrated. Urobilin, a biomarker indicating fecal contamination in water sources, was used as a fluorescence marker. Using a low cost, LED light source, fluorescence from a urobilin-zinc complex was detected down to concentrations of 800 fM.[84] Further enhancement of fluorescence generation was demonstrated by adding scattering particles to the sample. This causes the excitation light to scatter inside the fluorescence sample, allowing for longer optical pathlenghts and more fluorescence generation.

Finally, we demonstrated alternate integrating cavity designs that could potentially be used for controlled gas analysis. Several other diffuse reflectors, such as barium sulfate powder and white quartz, could be used for more commercially viable devices. White quartz is a solid, and thus is not as susceptible to damage over time. Barium sulfate does not suffer from broad background emission issues like the quartz powder, allowing for the potential for longer integrating times and more sensitive detection.

7.2 Future Work

While this dissertation has demonstrated significant enhancement to the linear variants of absorption, fluorescence, and Raman spectroscopy, significant work remains that could further optimize these techniques. Methods to improve the detection efficiency and simulation studies to optimize cavity design could potentially

add further orders of magnitude enhancement. In addition, work remains in further optimizing the manufacturing of the cavity itself, particularly in the case where an alternate diffuse reflector to fumed silica is used. This could allow for a lower cost device that could still provide significant enhancement.

Detection of the fluorescence or Raman signal was achieved by imaging the entrance aperture of the integrating cavity to an optical fiber or fiber bundle. Since the light exiting the cavity is diffuse in nature, it is difficult to collimate or image this with high efficiency to a fiber. Additionally, fiber coupling is inherently not the most efficient was of directing light to a spectrometer, as a significant percent can be lost when launching light into the fiber itself. Because of this, the use of a two-dimensional, aperture coded spectrometer could greatly improve the collection efficiency.[132] This type of system replaces the traditional dispersive spectrometer with a more complicated spatial filter which is then imaged to a two-dimensional detector such as a CCD or CMOS camera. These system have been previously optimized for Raman spectroscopy from diffuse sources such as tissue.[133] This design would allow for better collection efficiency of light exiting the integrating cavity, potentially further improving detection sensitivity. With *a priori* knowledge of the Raman spectrum being collected, careful construction of the coded mask could allow for reduction in the background intensity.

A second avenue for further improvement could come from the use of computer simulations. Monte Carlo based simulations are commonly used to model light propagation through turbid, scattering media.[90,91] These methods could be applied to modeling light propagation inside of an integrating cavity. Simulations could then be tailored to try to optimize the size of the entrance aperture, the size of the internal cavity, necessary wall thicknesses for different diffuse reflectors, as well as explore differences in geometry.

Figure 7.1: Conceptual rendering of an integrating cavity based water analysis system

As integrating cavity absorption spectroscopy can be done with low cost LED sources, the complete system could be packaged into a portable device. A conceptual rendering of this is shown in Fig. 7.1. This device could potentially be used to provide metrics of water quality, whether it be for dissolved organic matter.[50]

REFERENCES

[1] Schwarzenbach, R. P. *et al.* The challenge of micropollutants in aquatic systems. *Science* **313**, 1072–1077 (2006).

[2] Freire, C. *et al.* Association of traffic-related air pollution with cognitive development in children. *Journal of Epidemiology and Community Health* **64**, 223–228 (2010).

[3] Brandt, A. R. *et al.* Methane leaks from North American natural gas systems. *Science* **343**, 733–735 (2014).

[4] Kharitonov, S. A. & Barnes, P. J. Exhaled markers of pulmonary disease. *American Journal of Respiratory and Critical Care Medicine* **163**, 1693–1722 (2001).

[5] Baer, D. S., Paul, J. B., Gupta, M. & O'Keefe, A. Sensitive absorption measurements in the near-infrared region using off-axis integrated cavity output spectroscopy. *Proc. SPIE* **4817**, 167–176 (2002).

[6] Kim, K. H., Jahan, S. A. & Kabir, E. A review of breath analysis for diagnosis of human health. *TrAC - Trends in Analytical Chemistry* **33**, 1–8 (2012).

[7] McCulloch, M., Turner, K. & Broffman, M. Lung cancer detection by canine scent: will there be a lab in the lab? *European Respiratory Journal* **39**, 511–512 (2012).

[8] Wang, C. & Surampudi, A. B. An acetone breath analyzer using cavity ringdown spectroscopy: an initial test with human subjects under various situations. *Measurement Science and Technology* **19**, 105604 (2008).

[9] Hrubesh, L. W. & Droege, M. W. Pure-rotational spectrometry: a vintage analytical method applied to modern breath analysis. *Journal of Breath Research* **7**, 37105 (2013).

[10] de Lacy Costello, B. *et al.* A review of the volatiles from the healthy human body. *Journal of Breath Research* **8**, 14001 (2014).

[11] Amann, A., Corradi, M., Mazzone, P. & Mutti, A. Lung cancer biomarkers in exhaled breath. *Expert Review of Molecular Diagnostics* (2011).

[12] Huestis, M. A. & Cone, E. J. Relationship of Δ9-Tetrahydrocannabinol Concentrations in Oral Fluid and Plasma after Controlled Administration of Smoked Cannabis. *Journal of Analytical Toxicology* **28**, 394–399 (2004).

[13] Eng, J. K., McCormack, A. L. & Yates, J. R. An approach to correlate tandem mass spectral data of peptides with amino acid sequences in a protein database. *Journal of the American Society for Mass Spectrometry* **5**, 976–989 (1994).

[14] Jones-Lepp, T. L. Chemical markers of human waste contamination: analysis of urobilin and pharmaceuticals in source waters. *Journal of Environmental Monitoring* **8**, 472–478 (2006).

[15] Duckworth, H. E., Barber, R. C. & Venkatasubramanian, V. S. *Mass spectroscopy* (Cambridge University Press, New York, 1986).

[16] Snyder, L. R., Kirkland, J. J. & Dolan, J. W. *Introduction to modern liquid chromatography* (John Wiley & Sons, New York, 2009), 3rd edn.

[17] Ligor, T. *et al.* The analysis of healthy volunteers' exhaled breath by the use of solid-phase microextraction and GC-MS. *Journal of Breath Research* **2**, 46006 (2008).

[18] Buszewski, B., Ulanowska, A., Ligor, T., Denderz, N. & Amann, A. Analysis of exhaled breath from smokers, passive smokers and non-smokers by solid-phase microextraction gas chromatography/mass spectrometry. *Biomedical Chromatography* **23**, 551–556 (2009).

[19] Wzorek, B., Mochalski, P., Śliwka, I. & Amann, A. Application of GC-MS with a SPME and thermal desorption technique for determination of dimethylamine and trimethylamine in gaseous samples for medical diagnostic purposes. *Journal of Breath Research* **4**, 26002 (2010).

[20] Colthup, N. B., Daly, L. H. & Wiberley, S. E. *Introduction to infrared and Raman spectroscopy* (Academic Press, Inc., San Diego, 1990).

[21] Haka, A. S. *et al.* Diagnosing breast cancer by using Raman spectroscopy. *Proceedings of the National Academy of Sciences* **102**, 12371–12376 (2005).

[22] Lawson, E. E., Barry, B. W., Williams, A. C. & Edwards, H. G. M. Biomedical Applications of Raman Spectroscopy. *Journal of Raman Spectroscopy* **28**, 111–117 (1997).

[23] Hecht, E. *Optics* (Addison Wesley, San Francisco, 2002), 4th edn.

[24] TroyanovaWood, M. A., Troyanova-Wood, G. I., Petrov, V. V. & Yakovlev. Simple and inexpensive instrument for deep-UV Raman spectroscopy. *Journal of Raman Spectroscopy* **44**, 1789–1791 (2013).

[25] Hokr, B. H. & Yakovlev, V. V. Raman signal enhancement via elastic light scattering. *Optics Express* **21**, 11757–11762 (2013).

[26] Cheng, J.-x. & Xie, X. S. Coherent Anti-Stokes Raman Scattering Microscopy: Instrumentation, Theory, and Applications. *Journal of Physics Chemical B* **108**, 827–840 (2004).

[27] Stiles, P. L., Dieringer, J. A., Shah, N. C. & Van Duyne, R. P. Surface-enhanced Raman spectroscopy. *Annual Review of Analytical Chemistry* **1**, 601–626 (2008).

[28] Pestov, D. *et al.* Single-shot detection of bacterial endospores via coherent Raman spectroscopy. *Proceedings of the National Academy of Sciences* **105**, 422–427 (2008).

[29] Arora, R., Petrov, G. I., Yakovlev, V. V. & Scully, M. O. Detecting anthrax in the mail via coherent Raman microspectroscopy. *CLEO: 2011 - Laser Science to Photonic Applications* **109**, 1–2 (2011).

[30] Evans, C. L. & Xie, X. S. Coherent anti-Stokes Raman scattering microscopy: chemical imaging for biology and medicine. *Annual Review of Analytical Chemistry* **1**, 883–909 (2008).

[31] Fu, Y., Wang, H., Huff, T. B., Shi, R. & Cheng, J.-X. Coherent anti-stokes Raman scattering imaging of myelin degradation reveals a calcium-dependent pathway in lyso-PtdCho-induced demyelination. *Journal of Neuroscience Research* **85**, 2870–2881 (2007).

[32] Nie, S. & Emory, S. R. Probing single molecules and single nanoparticles by surface-enhanced Raman scattering. *Science* **275**, 1102–1106 (1997).

[33] Altun, A. O., Youn, S. K., Yazdani, N., Bond, T. & Park, H. G. Metal-dielectric-CNT nanowires for femtomolar chemical detection by surface enhanced Raman spectroscopy. *Advanced Materials* **25**, 4431–4436 (2013).

[34] Biggs, K. B., Camden, J. P., Anker, J. N. & Duyne, R. P. V. Surface-Enhanced Raman Spectroscopy of Benzenethiol Adsorbed from the Gas Phase onto Silver Film over Nanosphere Surfaces: Determination of the Sticking Probability and

Detection Limit Time. *The Journal of Physical Chemistry A* **113**, 4581–4586 (2009).

[35] Teich, M. C. & Saleh, B. E. A. *Fundamentals of photonics* (Canada, Wiley Interscience, 1991).

[36] Berezin, M. & Achilefu, S. Fluorescence lifetime measurements and biological imaging. *Chemical Reviews* **110**, 2641–2684 (2010).

[37] Shaner, N. C., Steinbach, P. A. & Tsien, R. Y. A guide to choosing fluorescent proteins. *Nature Methods* **2**, 905–909 (2005).

[38] Hong, G. *et al.* Through-skull fluorescence imaging of the brain in a new near-infrared window. *Nature Photonics* **8**, 723–730 (2014).

[39] Flusberg, B. A., Jung, J. C., Cocker, E. D., Anderson, E. P. & Schnitzer, M. J. In vivo brain imaging using a portable 3.9 gram two-photon fluorescence microendoscope. *Optics Letters* **30**, 2272–2274 (2005).

[40] Ntziachristos, V., Tung, C.-H., Bremer, C. & Weissleder, R. Fluorescence molecular tomography resolves protease activity in vivo. *Nature Medicine* **8**, 757–761 (2002).

[41] Polglase, A. L. *et al.* A fluorescence confocal endomicroscope for in vivo microscopy of the upper- and the lower-GI tract. *Gastrointestinal Endoscopy* **62**, 686–695 (2005).

[42] Le Goualher, G. Towards Optical Biopsies with an Integrated Fibered Confocal Fluorescence Microscope. *Medical Image Computing and Computer-Assisted Intervention* **3217**, 761–768 (2004).

[43] Flusberg, B. A. *et al.* Fiber-optic fluorescence imaging. *Nature Methods* **2**, 941–950 (2005).

[44] Kara, M. A. *et al.* Characterization of tissue autofluorescence in Barrett's esophagus by confocal fluorescence microscopy. *Dis Esophagus* **20**, 141–150 (2007).

[45] Lee, C. M., Engelbrecht, C. J., Soper, T. D., Helmchen, F. & Seibel, E. J. Scanning fiber endoscopy with highly flexible, 1 mm catheterscopes for wide-field, full-color imaging. *Jouranl of Biophotonics* **3**, 385–407 (2010).

[46] Hsiung, P. L. *et al.* Detection of colonic dysplasia in vivo using a targeted heptapeptide and confocal microendoscopy. *Nature Medicine* **14**, 454–458 (2008).

[47] Tan, C., Gajovic-Eichelmann, N., Polzius, R., Hildebrandt, N. & Bier, F. F. Direct detection of Δ9-tetrahydrocannabinol in aqueous samples using a homogeneous increasing fluorescence immunoassay (HiFi). *Analytical and Bioanalytical Chemistry* **398**, 2133–2140 (2010).

[48] Rigler, R. Fluorescence correlations, single molecule detection and large number screening applications in biotechnology. *Journal of Biotechnology* **41**, 177–186 (1995).

[49] Mertz, J., Xu, C. & Webb, W. W. Single-molecule detection by two-photon-excited fluorescence. *Optics Letters* **20**, 2532–2534 (1995).

[50] Cory, R. M. & McKnight, D. M. Fluorescence spectroscopy reveals ubiquitous presence of oxidized and reduced quinones in dissolved organic matter. *Environmental Science & Technology* **39**, 8142–8149 (2005).

[51] Ye, J. & Lynn, T. W. Applications of Optical Cavities in Modern Atomic, Molecular, and Optical Physics. *Advances In Atomic, Molecular, and Optical Physics* **49**, 1–83 (2003).

[52] Knittel, J., Swaim, J. D., McAuslan, D. L., Brawley, G. A. & Bowen, W. P. Back-scatter based whispering gallery mode sensing. *Scientific Reports* **3**, 2974 (2013).

[53] Beier, H. T., Coté, G. L. & Meissner, K. E. Whispering gallery mode biosensors consisting of quantum dot-embedded microspheres. *Annals of Biomedical Engineering* **37**, 1974–83 (2009).

[54] Wheeler, M. D., Newman, S. M., Orr-Ewing, A. J. & Ashfold, M. N. R. Cavity ring-down spectroscopy. *Journal of the Chemical Society, Faraday Transactions* **94**, 337–351 (1998).

[55] Berden, G., Peeters, R. & Meijer, G. Cavity ring-down spectroscopy: Experimental schemes and applications. *International Reviews in Physical Chemistry* **19**, 565–607 (2000).

[56] Herbelin, J. M. *et al.* Sensitive measurement of photon lifetime and true reflectances in an optical cavity by a phase-shift method. *Applied Optics* **19**, 144–7 (1980).

[57] Anderson, D. Z., Frisch, J. C. & Masser, C. S. Mirror reflectometer based on optical cavity decay time. *Applied Optics* **23**, 1238 (1984).

[58] Mazurenka, M., Orr-Ewing, A. J., Peverall, R. & Ritchie, G. A. D. Cavity ring-down and cavity enhanced spectroscopy using diode lasers. *Annual Reports Section "C" (Physical Chemistry)* **101**, 100 (2005).

[59] Baer, D. S., Hanson, R. K., Newfield, M. E. & Gopaul, N. K. J. M. Multiplexed diode-laser sensor system for simultaneous H2O, O2, and temperature measurements. *Optics Letters* **19**, 1900 (1994).

[60] Peeters, R., Berden, G., Apituley, A. & Meijer, G. Open-path trace gas detection of ammonia based on cavity-enhanced absorption spectroscopy. *Applied Physics B* **71**, 231–236 (2000).

[61] Bayrakli, I. & Akman, H. Ultrasensitive, real-time analysis of biomarkers in breath using tunable external cavity laser and off-axis cavity-enhanced absorption spectroscopy. *Journal of Biomedical Optics* **20**, 37001 (2015).

[62] Paul, J. B., Lapson, L. & Anderson, J. G. Ultrasensitive absorption spectroscopy with a high-finesse optical cavity and off-axis alignment. *Applied Optics* **40**, 4904–4910 (2001).

[63] Symes, R., Meresman, H., Sayer, R. M. & Reid, J. P. A quantitative demonstration of the enhancement of cavity enhanced Raman scattering by broad band external laser seeding. *Chemical Physics Letters* **419**, 545–549 (2006).

[64] Hill, R. A., Mulac, A. J. & Hackett, C. E. Retroreflecting multipass cell for Raman scattering. *Applied Optics* **16**, 2004–6 (1977).

[65] King, D. A. & Pittaro, R. J. Simple diode pumping of a power-buildup cavity. *Optics Letters* **23**, 774 (1998).

[66] Taylor, D. J., Glugla, M. & Penzhorn, R.-D. Enhanced Raman sensitivity using an actively stabilized external resonator. *Review of Scientific Instruments* **72**, 1970 (2001).

[67] Ohara, S., Yamaguchi, S., Endo, M., Nanri, K. & Fujioka, T. Performance Characteristic of Power Build-Up Cavity for Raman Spectroscopic Measurement. *Optical Review* **10**, 342–345 (2003).

[68] Li, X., Xia, Y., Zhan, L. & Huang, J. Near-confocal cavity-enhanced Raman spectroscopy for multitrace-gas detection. *Optics Letters* **33**, 2143–2145 (2008).

[69] Kim, A., Roy, M., Dadani, F. & Wilson, B. C. A fiberoptic reflectance probe with multiple source-collector separations to increase the dynamic range of derived tissue optical absorption and scattering coefficients. *Optics Express* **18**, 5580–5594 (2010).

[70] Cone, M. T. *et al.* Measuring the absorption coefficient of biological materials using integrating cavity ring-down spectroscopy. *Optica* **2**, 162–168 (2015).

[71] Labsphere. Reflectance Materials and Coatings. Tech. Rep., Labsphere Inc., (2011). URL `http://www.labsphere.com`.

[72] Palmer, J. M. & Grant, B. G. *The art of radiometry* (SPIE Press, Bellingham, 2010).

[73] Pickering, J. W. *et al.* Double-Integrating-Sphere System for Measuring the Optical Properties of Tissue. *Applied Optics* **32**, 399–410 (1993).

[74] Salomatina, E., Jiang, B., Novak, J. & Yaroslavsky, A. N. Optical properties of normal and cancerous human skin in the visible and near-infrared spectral range. *Journal of Biomedical Optics* **11**, 64026–64029 (2006).

[75] Bashkatov, A. N., Genina, E. A., Kochubey, V. I. & Tuchin, V. V. Optical properties of human skin, subcutaneous and mucous tissues in the wavelength range from 400 to 2000 nm. *Journal of Physics D: Applied Physics* **38**, 2543 (2005).

[76] Grum, F. & Wightman, T. E. Absolute reflectance of Eastman White Reflectance Standard. *Applied Optics* **16**, 2775–2776 (1977).

[77] Grum, F. & Luckey, G. W. Optical sphere paint and a working standard of reflectance. *Applied Optics* **7**, 2289–94 (1968).

[78] Musser, J. A. *Novel instrumentation for a scattering independent measurement of the absorption coefficient of natural waters, and a new diffuse reflector for spectroscopic instrumentation and close cavity coupling.* Ph.D. thesis, Texas A&M (2006).

[79] Barthel, H., Heinemann, M., Stintz, M. & Wessely, B. Particle Sizes of Fumed Silica. *Chemical Engineering & Technology* **21**, 745–752 (1998).

[80] Stokes, G. On the intensity of the light reflected from or transmitted through a pile of plates. *Proceedings of the Royal Society of London* **11**, 545–556 (1860).

[81] Fry, E. S., Musser, J., Kattawar, G. W. & Zhai, P.-W. Integrating cavities: temporal response. *Applied Optics* **45**, 9053–9065 (2006).

[82] Labsphere. Technical Guide: Integrating Sphere Theory and Applications. Tech. Rep. (2011). URL `http://www.labsphere.com/`.

[83] Cone, M. T. *A new diffuse reflecting material with applications including integrating cavity ring-down spectroscopy.* Ph.D. thesis, Texas A&M (2014).

[84] Bixler, J. N. *et al.* Ultrasensitive detection of waste products in water using fluorescence emission cavity-enhanced spectroscopy. *Proceedings of the National Academy of Sciences* **111**, 7208–7211 (2014).

[85] Fry, E. S., Kattawar, G. W. & Pope, R. M. Integrating cavity absorption meter. *Applied Optics* **31**, 2055–2065 (1992).

[86] Jacques, S. L. Optical properties of biological tissues: a review. *Physics in Medicine and Biology* **58**, R37–61 (2013).

[87] Prahl, S. A. *Light transport in tissue.* Ph.D. thesis, University of Texas at Austin (1988).

[88] Prahl, S. A. The Adding-Doubling Method. In Welch, A. J. & van Gemert, M. J. C. (eds.) *Optical-Thermal Response of Laser Irradiated Tissue*, chap. 5, 101–129 (Plenum Press, New York, 1995).

[89] Prahl, S. A., van Gemert, M. J. C. & Welch, A. J. Determining the Optical Properties of Turbid Media by Using the Adding-Doubling Method. *Applied Optics* **32**, 559–568 (1993).

[90] Hokr, B. H. *et al.* Modeling focusing Gaussian beams in a turbid medium with Monte Carlo simulations. *Optics Express* **23**, 8699 (2015).

[91] Wang, L., Jacques, S. L. & Zheng, L. MCMLMonte Carlo modeling of light transport in multi-layered tissues. *Computer Methods and Programs in Biomedicine* **47**, 131–146 (1995).

[92] Denton, M. L. *et al.* Damage Thresholds for Exposure to NIR and Blue Lasers in an In Vitro RPE Cell System. *Investigative Ophthalmology & Vsual Science* **47**, 3065–73 (2006).

[93] Hanlon, E. B. *et al.* Prospects for in vivo Raman spectroscopy. *Physics in Medicine and Biology* **45**, R1 (2000).

[94] Salter, R., Chu, J. & Hippler, M. Cavity-enhanced Raman spectroscopy with optical feedback cw diode lasers for gas phase analysis and spectroscopy. *Analyst* **137**, 4669–4676 (2012).

[95] Bixler, J. N. & Yakovlev, V. V. A new SERS: scattering enhanced Raman scattering. In *SPIE BiOS*, 893906–893909 (2014).

[96] Zhao, J., Lui, H., McLean, D. I. & Zeng, H. Automated Autofluorescence Background Subtraction Algorithm for Biomedical Raman Spectroscopy. *Applied Spectroscopy* **61**, 1225–1232 (2007).

[97] Lieber, C. A. & Mahadevan-Jansen, A. Automated method for subtraction of fluorescence from biological Raman spectra. *Applied Spectroscopy* **57**, 1363–1367 (2003).

[98] Brandt, N. N., Brovko, O. O., Chikishev, A. Y. & Paraschuk, O. D. Optimization of the rolling-circle filter for Raman background subtraction. *Applied Spectroscopy* **60**, 288–293 (2006).

[99] Zhang, Z.-M. *et al.* An intelligent background-correction algorithm for highly fluorescent samples in Raman spectroscopy. *Journal of Raman Spectroscopy* **41**, 659–669 (2009).

[100] Short, K. W., Carpenter, S., Freyer, J. P. & Mourant, J. R. Raman spectroscopy detects biochemical changes due to proliferation in mammalian cell cultures. *Biophysical Journal* **88**, 4274–4288 (2005).

[101] Phillips, D. H. Fifty years of benzo(a)pyrene. *Nature* **303**, 468–472 (1983).

[102] Denissenko, M. F., Pao, A., Tang, M.-s. & Pfeifer, G. P. Preferential formation of benzo[a]pyrene adducts at lung cancer mutational hotspots in P53. *Science* **274**, 430–432 (1996).

[103] Moorthy, B., Chu, C. & Carlin, D. J. Polycyclic Aromatic Hydrocarbons: From Metabolism to Lung Cancer. *Toxicological Sciences* **145**, 5–15 (2015).

[104] Petersen, D. G., Sundbäck, K., Larson, F. & Dahllöf, I. Pyrene toxicity is affected by the nutrient status of a marine sediment community: implications for risk assessment. *Aquatic Toxicology* **95**, 37–43 (2009).

[105] Snow, J. *On the mode of communication of cholera* (John Churchill, London, 1855).

[106] Grant, S. B. *et al.* Taking the waste out of wastewater for human water security and ecosystem sustainability. *Science* **337**, 681–686 (2012).

[107] Waring, S. C. & Brown, B. J. The threat of communicable diseases following natural disasters: a public health response. *Disaster Management & Response* **3**, 41–47 (2005).

[108] Richardson, S. D. & Ternes, T. A. Water analysis: emerging contaminants and current issues. *Analytical Chemistry* **77**, 3807–3838 (2005).

[109] Bisceglia, K. J., Yu, J. T., Coelhan, M., Bouwer, E. J. & Roberts, A. L. Trace determination of pharmaceuticals and other wastewater-derived micropollutants by solid phase extraction and gas chromatography/mass spectrometry. *Journal of chromatography A* **1217**, 558–564 (2010).

[110] Ternes, T. A., Hirsch, R., Mueller, J. & Haberer, K. Methods for the determination of neutral drugs as well as betablockers and β2-sympathomimetics in aqueous matrices using GC/MS and LC/MS/MS. *Fresenius' Journal of Analytical Chemistry* **362**, 329–340 (1998).

[111] Girones, R. *et al.* Molecular detection of pathogens in waterthe pros and cons of molecular techniques. *Water Research* **44**, 4325–4339 (2010).

[112] Wéry, N., Lhoutellier, C., Ducray, F., Delgenès, J.-P. & Godon, J.-J. Behaviour of pathogenic and indicator bacteria during urban wastewater treatment and sludge composting, as revealed by quantitative PCR. *Water Research* **42**, 53–62 (2008).

[113] Miyabara, Y., Sugaya, N., Suzuki, J. & Suzuki, S. Estimation of urobilin as a fecal pollution indicator in the aquatic environment. *Bulletin of Environmental Contamination and Toxicology* **53**, 77–84 (1994).

[114] Collinder, E. *et al.* Gastrointestinal host-microbial interactions in mammals and fish: Comparative studies in man, mice, rats, pigs, horses, cows, elks, reindeers, salmon and cod. *Microbial Ecology in Health and Disease* **15**, 66–78 (2003).

[115] Miyabara, Y., Tabata, M., Suzuki, J. & Suzuki, S. Separation and sensitive determination of i-urobilin and l-stercobilin by high-performance liquid chromatography with fluorimetric detection. *Journal of Chromatography B: Biomedical Sciences and Applications* **574**, 261–265 (1992).

[116] Lam, C.-W., Lai, C.-K. & Chan, Y.-W. Simultaneous fluorescence detection of fecal urobilins and porphyrins by reversed-phase high-performance thin-layer chromatography. *Clinical Chemistry* **44**, 345–346 (1998).

[117] Kerkhoff, J. F. & Peters, H. J. A reproducible estimation of the urobilin concentration in urine by means of a modified Schlesinger test. *Clinica Chimica Acta* **21**, 133–137 (1968).

[118] Bull, R. V. A., Lim, C. K. & Gray, C. H. High-performance liquid chromatography of bile pigments: Separation and characterization of the urobilinoids. *Journal of Chromatography A* **218**, 647–652 (1981).

[119] OKeefe, A. & Deacon, D. A. G. Cavity ringdown optical spectrometer for absorption measurements using pulsed laser sources. *Review of Scientific Instruments* **59**, 2544–2551 (1988).

[120] Pope, R. M. & Fry, E. S. Absorption spectrum (380–700 nm) of pure water. II. Integrating cavity measurements. *Applied Optics* **36**, 8710–8723 (1997).

[121] Tarsa, P. B., Wist, A. D., Rabinowitz, P. & Lehmann, K. K. Single-cell detection by cavity ring-down spectroscopy. *Applied Physics Letters* **85**, 4523–4525

(2004).

[122] Han, J. & Burgess, K. Fluorescent indicators for intracellular pH. *Chemical Reviews* **110**, 2709–2728 (2010).

[123] Prahl, S. Mie scattering calculator (2007). URL `omlc.org/calc/mie_calc.html`.

[124] Bohren, C. F. & Huffman, D. R. *Absorption and Scattering of Light by Small Particles* (John Wiley & Sons, New York, 2008).

[125] Cone, M. T., Musser, J. A., Figueroa, E., Mason, J. D. & Fry, E. S. Diffuse reflecting material for integrating cavity spectroscopy, including ring-down spectroscopy. *Applied Optics* **54**, 334–346 (2015).

[126] McKnight, D. M. *et al.* Spectrofluorometric characterization of dissolved organic matter for indication of precursor organic material and aromaticity. *Limnology and Oceanography* **46**, 38–48 (2001).

[127] Bereza-Malcolm, L. T., Mann, G. & Franks, A. E. Environmental Sensing of Heavy Metals Through Whole Cell Microbial Biosensors: A Synthetic Biology Approach. *ACS Synthetic Biology* (2014).

[128] Hokr, B. H. *et al.* Bright emission from a random Raman laser. *Nature Communications* **5**, 4356 (2014).

[129] Jackson, R. D., Clarke, T. R. & Susan Moran, M. Bidirectional calibration results for 11 spectralon and 16 BaSO4 reference reflectance panels. *Remote Sensing of Environment* **40**, 231–239 (1992).

[130] Mason, J. D. *et al.* Robust Commercial Diffuse Reflector for UV-VIS-NIR Applications. *Applied Optics* **54** (2015).

[131] Wild, D. *The immunoassay handbook: theory and applications of ligand binding, ELISA and related techniques* (Elsevier, Amsterdam, 2013), fourth edn.

[132] Gehm, M. E. *et al.* Static two-dimensional aperture coding for multimodal, multiplex spectroscopy. *Applied Optics* **45**, 2965–2974 (2006).

[133] McCain, S. T., Gehm, M. E., Wang, Y., Pitsianis, N. P. & Brady, D. J. Coded aperture Raman spectroscopy for quantitative measurements of ethanol in a tissue phantom. *Applied Spectroscopy* **60**, 663–671 (2006).

APPENDIX A

RAW PYRENE RAMAN SPECTRA

The individual Raman spectra for each concentration used in the 473 nm detection limit study are shown here. The left plot in each figure shows the both the Raman shift for pyrene at 1403 cm^{-1} as well as the oxygen peak. The right plot shows a magnified view of the 1403 cm^{-1} Raman shift.

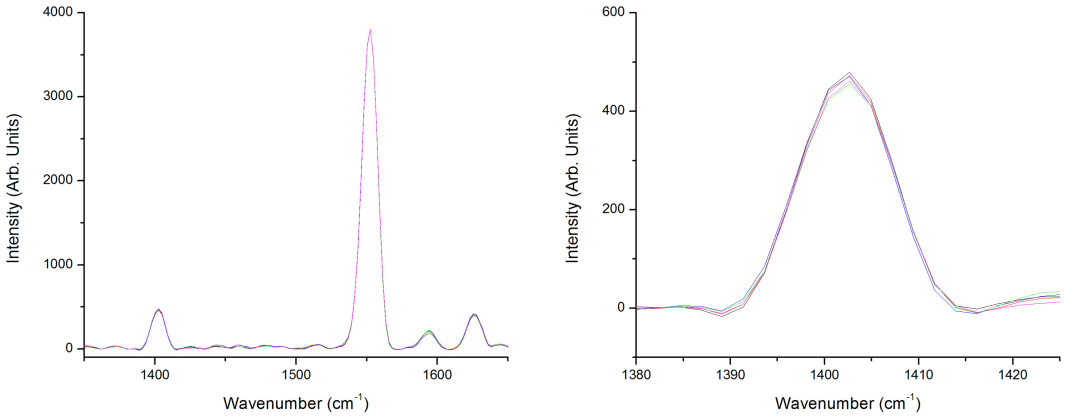

Figure A.1: Plot of the Raman spectra for 740.7 nM pyrene

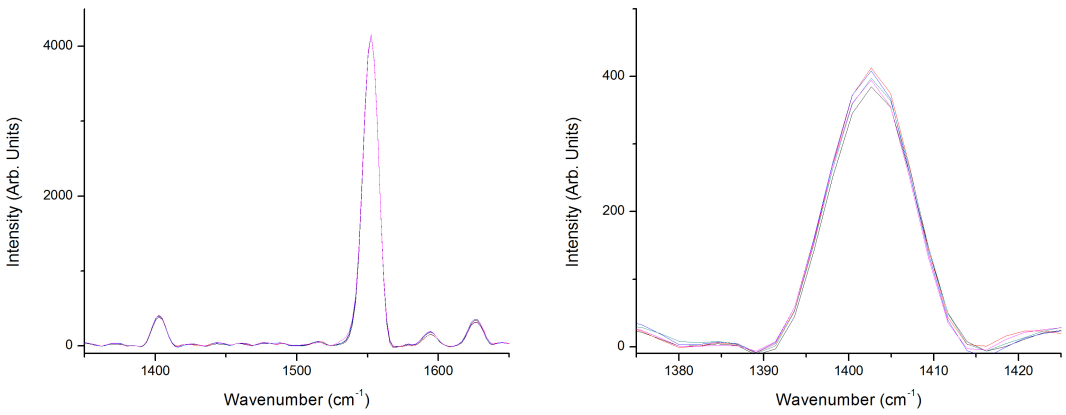

Figure A.2: Plot of the Raman spectra for 555.5 nM pyrene

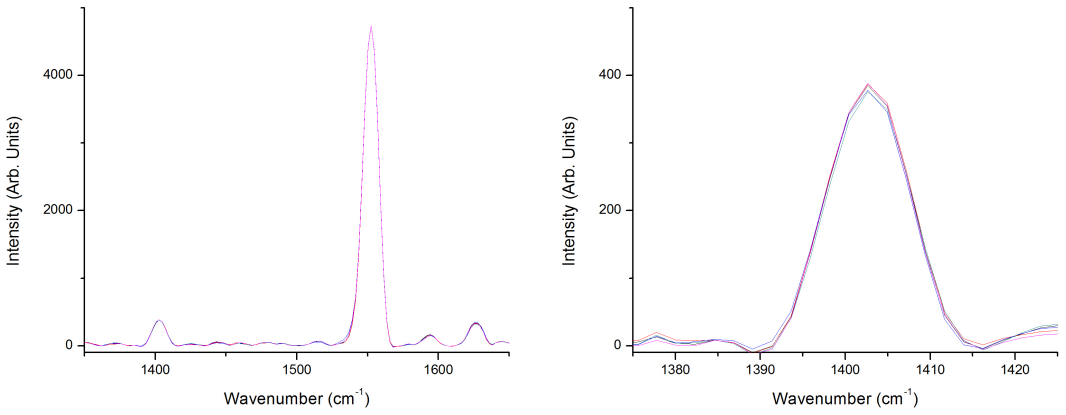

Figure A.3: Plot of the Raman spectra for 463.0 nM pyrene

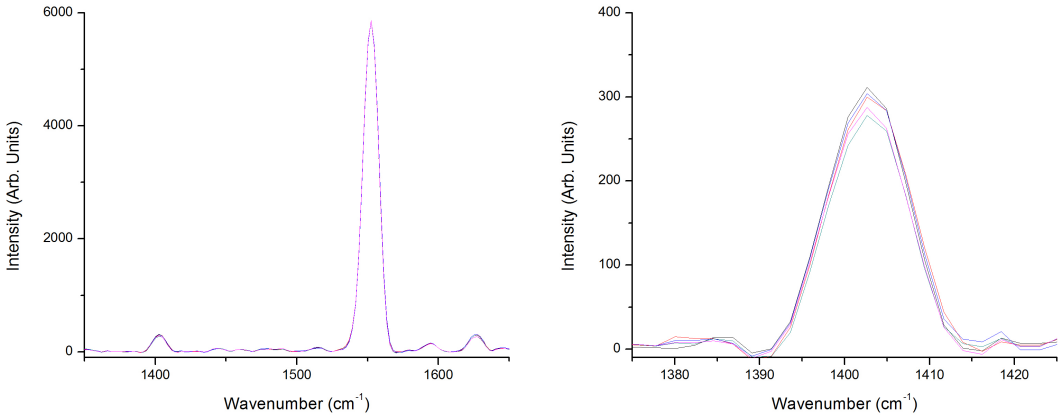

Figure A.4: Plot of the Raman spectra for 370.4 nM pyrene

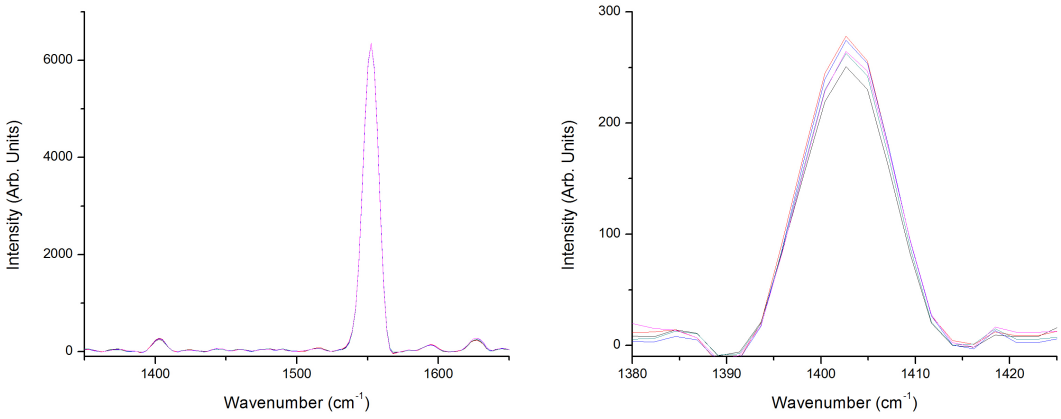

Figure A.5: Plot of the Raman spectra for 277.8 nM pyrene

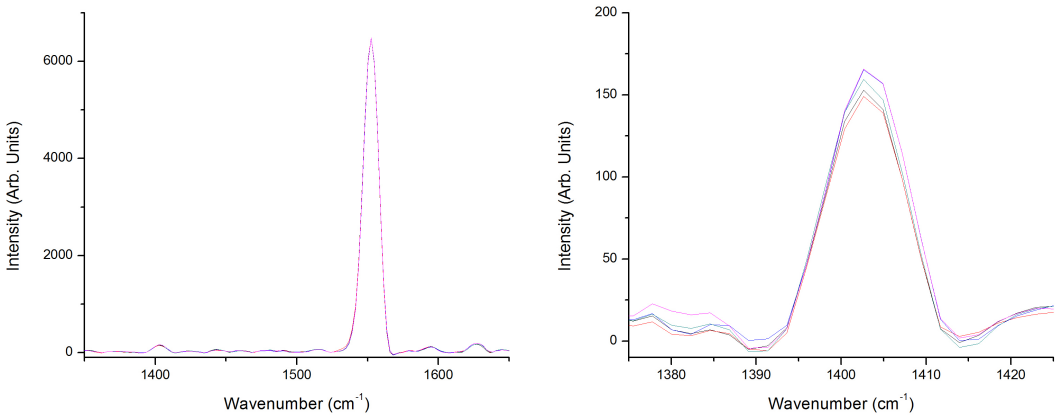

Figure A.6: Plot of the Raman spectra for 185.2 nM pyrene

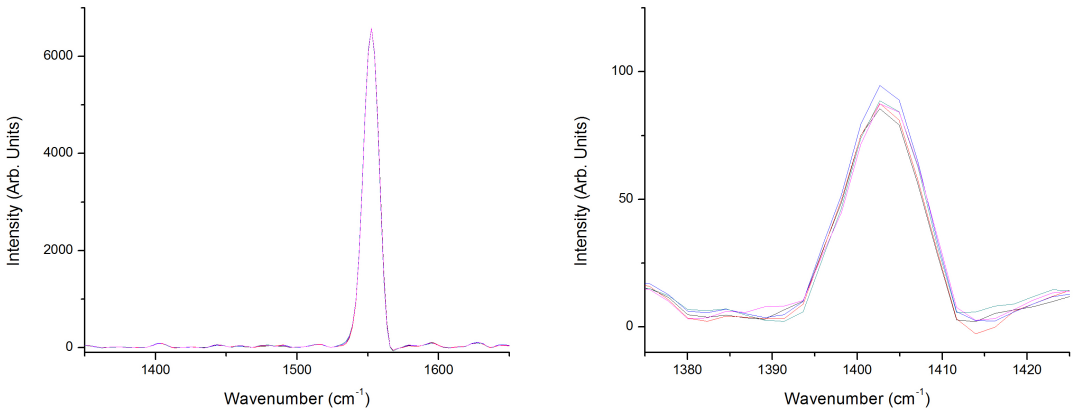

Figure A.7: Plot of the Raman spectra for 92.6 nM pyrene

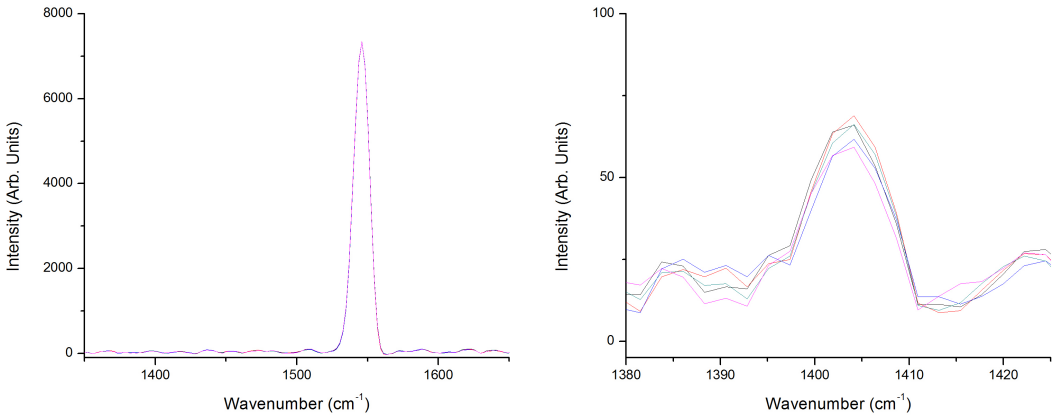

Figure A.8: Plot of the Raman spectra for 37.0 nM pyrene

APPENDIX B

RAMAN SPECTROSCOPY PROCESSING CODE

B.1 Background Subtraction Code

MATLAB code used for background subtraction. backSub3 is first called from a script that loads in the raw data. The original spectrum and a smoothed spectrum are passed to this function, along with the number of iterations and dampening parameter.

```
%Background Subtract
function [newRaman] = backSub3(w,y,y2,iter,p)
% w = nm
% y = raman data with background
% p = dampening parameter.



initial = y;
for i = 1:1:iter
[fit,gof] = createFit1(w,y,p);
newY = fit(w);


for j=1:1:length(newY)
if(newY(j)>y2(j))
newY(j) = y2(j);
end
```

```
end
y = newY;
end

%figure;plot(w,y2,w,y);
newRaman = y;
%newRaman = initial-y; %

%figure;plot(w,newRaman);
```

MATLAB code for generation the iterative cubic spline fit.

```
function [fitresult, gof] = createFit1(X, Yfit, p)

%      X Input : X
%      Y Output: Yfit
%  Output:
%      fitresult : a fit object representing the fit.
%      gof : structure with goodness-of fit info.
%
%  See also FIT, CFIT, SFIT.

[xData, yData] = prepareCurveData( X, Yfit);

% Set up fittype and options.
ft = fittype( 'smoothingspline' );
opts = fitoptions( 'Method', 'SmoothingSpline' );
```

```
opts.SmoothingParam = p;
%8.316800817771172E-6;

% Fit model to data.
[fitresult, gof] = fit( xData, yData, ft, opts );

% Plot fit with data.
% figure( 'Name', 'untitled fit 1' );
% h = plot( fitresult, xData, yData );
% legend( h, 'Yfit vs. X', 'untitled fit 1',
 'Location', 'NorthEast' );
% % Label axes
% xlabel X
% ylabel Yfit
% grid on
```

B.2 Atmosphere Processing

This MATLAB script was used to read in and process the atmospheric Raman data.

```
clear all; close all;
[filename1,filepath1,filterindex]=uigetfile('*.*',
'select file','Multiselect','on');
[x,num] = size(filename1);

for k=1:num
file = strcat(filepath1,filename1{k});
```

```
data =load(file);
%Import x,y spectral data. Discard anything under 1325 cm^-1
x = data(251:1024,1); %wavenumbers
raw(:,k) = data(251:1024,2); %intensity

%Split into two ranges for background removal
x1 = x(1:215);
x2 = x(216:end);
y1 = raw(1:215,k);
y2 = raw(216:774,k);

%Smooth data to remove fluorescence background
y1b = smooth(y1,25,'rlowess'); %Smooth to remove Raman peaks
y2b = smooth(y2,25,'rlowess');

%Background Subtract
%Interative fitting of dampened cubic spline
background1 = backSub3(x1,y1b,3,0.005430707416226324);

%Interative fitting of dampened cubic spline
background2 = backSub3(x2,y2b,3,0.005430707416226324);

ySub1 = y1 - background1; %Subtract raw from background
ySub2 = y2 - background2;

%Merge data
```

```
YSub = [ySub1;ySub2];
YSub = smooth(YSub,9,'sgolay');

N = max(YSub); %Calculates N2 peak for normalization
%Build array of background subtracted data
Y(:,k) = YSub;
end

%Normalize and Average
N2 = mean(N); %Normalize based on the mean of the N2 peaks

%initialize array
avgY = zeros(length(Y),1);

%Sum y data
for i=1:num
avgY = avgY+Y(:,i);
end
avgY = avgY./num; %Compute average

figure;plot(x,avgY);
figure;plot(x,raw);

%Prepare to write out data
out = [x'; avgY'];
```

```
%Print data to text file
fileID = fopen(filename1{k},'w');
fprintf(fileID,'%f \t %f\r\n',out);
fclose(fileID);
```

B.3 Intensity Calculation

This MATLAB code was used to calculate the area of the pyrene peaks.

```
function [fitresult, gof] = figGaussian(peak1X, peak1Y)
%CREATEFIT2(PEAK1X,PEAK1Y)
%  Create a fit.
%
%  Data for 'untitled fit 1' fit:
%      X Input : peak1X
%      Y Output: peak1Y
%  Output:
%      fitresult : a fit object representing the fit.
%      gof : structure with goodness-of fit info.
%
%  See also FIT, CFIT, SFIT.

%  Auto-generated by MATLAB on 31-May-2015 15:47:59


%% Fit: 'untitled fit 1'.
[xData, yData] = prepareCurveData( peak1X, peak1Y );
```

```
% Set up fittype and options.
ft = fittype('a*exp(-((x-1403)/6.2)^2) + d', ...
'independent','x', ...
'dependent', 'y' );



%ft = fittype( 'a1*exp(-((x-b1)/c2)^2) + c1',
'coefficients',{'b1','c2'},'independent', 'x', 'dependent', 'y' );
opts = fitoptions( 'Method', 'NonlinearLeastSquares' );
opts.Display = 'Off';
opts.StartPoint = [0.685687136978989 6.2];

% Fit model to data.
[fitresult, gof] = fit( peak1X, peak1Y, ft, opts );

% Plot fit with data.
figure( 'Name', 'untitled fit 1' );
h = plot( fitresult, xData, yData );
legend( h, 'peak1Y vs. peak1X', 'untitled fit 1',
'Location', 'NorthEast' );
% Label axes
xlabel peak1X
ylabel peak1Y
grid on
```

B.4 Toxin Processing Code

MATLAB code used to process the toxin spectra. Parts of this were commented out depending on the data set being analyzed.

```
clear all; close all;
[filename1,filepath1,filterindex]=uigetfile('*.*',
'select file','Multiselect','on');
[x,num] = size(filename1);


for k=1:num
file = strcat(filepath1,filename1{k});
data =load(file);
%Import x,y spectral data. Discard anything under 1325 cm^-1
x = data(137:1024,1); %wavenumbers
raw(:,k) = data(137:1024,2); %intensity
raw(:,k) = smooth(raw(:,k),5,'sgolay');


%Split into three ranges for background removal
x1 = x(1:79);
x2 = x(80:327);
x3 = x(328:end);
y1 = raw(1:79,k);
y2 = raw(80:327,k);
y3 = raw(328:888,k);
```

```
%Smooth data to remove fluorescence background
y1b = smooth(y1,15,'rlowess'); %Smooth to remove Raman peaks
y2b = smooth(y2,15,'rlowess');
y3b = smooth(y3,15,'rlowess');



%Background Subtract
%Interative fitting of dampened cubic spline
background1 = backSub3(x1,y1b,y1,3,0.005430707416226324);
background2 = backSub3(x2,y2b,y2,3,0.005430707416226324);
background3 = backSub3(x3,y3b,y3,3,0.005430707416226324);

ySub1 = y1 - background1; %Subtract raw from background
ySub2 = y2 - background2;
ySub3 = y3 - background3;

%Merge data
YSub = [ySub1;ySub2;ySub3];
YSub = smooth(YSub,9,'sgolay');

O(k) = YSub(225); %Calculates N2 peak for normalization
%Build array of background subtracted data
Y(:,k) = YSub;

L2(k) = Y(158,k); %1403 line peak
end
```

```
%figure;plot(x,YSub);

%Normalize and Average
O2 = mean(O); %Normalize based on the mean of the N2 peaks
scale = O2./(O);
for i=1:num
%scale(i) = O2./O(i);
normY(:,i) = Y(:,i).*scale(i);
end

%Average
avgY = mean(normY,2);
figure;plot(x,avgY);
figure;plot(x,raw);

%Gaussian fit
% %select range
% xfit = x(138:178);
% yfit = normY(138:178,:);
% for i = 1:num;
%     [fitresult, gof] = createFit(xfit,yfit(:,i));
%     coeffs =coeffvalues(fitresult);
%     fit = coeffs(1)*exp(-((xfit-1420)/6.2).^2);% + coeffs(2);
%     %figure;plot(xfit,fit);
%     Area(i) = sum(fit);
% end
```

```
%Average and StdDev for peak intensity and area
peakAvg = mean(L2,2);
peakStd = std(L2,0,2);
%AreaAvg = mean(Area);
%AreaStd = std(Area);

%Prepare to write out data
out = [x'; avgY'];
out2 = [x';normY'];
peaksOut = [peakAvg, peakStd, O2, std(O)];

%Print spectral data to text file
file = strsplit(filepath1,'\');
filename = file{length(file)-1};

fileID = fopen(strcat(filename,'avg.txt'),'w');
fprintf(fileID,'%f \t %f\r\n',out);
fclose(fileID);

fileID = fopen(strcat(filename,'full.txt'),'w');
fprintf(fileID,'%f \t %f \t %f \t %f \t %f \t %f\r\n',out2);
fclose(fileID);

%Print peak data
filename2 = strrep(filename1{1},'.txt','Peaks.txt');
```

```
fileID2 = fopen(filename2,'w');
%fprintf(fileID2,'%f \t %f \t %f \t %f\r\n',peaksLoc);
fprintf(fileID2,'%f \t %f \t %f \t %f\r\n',peaksOut);
fclose(fileID2);
```

MATLAB code used to analyze the low concentration pyrene data generated by the toxin processing code.

```
clear all; close all;
[filename1,filepath1,filterindex]=uigetfile('*.*',
'select file','Multiselect','on');
[x,num] = size(filename1);

%Import Average Data
for k=1:num
file = strcat(filepath1,filename1{k});
data =load(file);
%Import x,y spectral data. Discard anything under
1325 cm^-1

x = data(:,1); %wavenumbers
y(:,k) = data(:,2);
O2(k) = y(225,k);
end

figure;plot(x,y);
```

```
%Normalize to O2
meanO2 = mean(O2);

for i=1:num
normY(:,i) = y(:,i).*(meanO2./O2(i));
L1(i) = normY(83,i);
L2(i) = normY(158,i);
end

figure;plot(x,normY);
mass = [2 5 10 15 20 25 30 40 0];
%scales = [1 5/4 5/4 5/3.75 5/3.75 5/3.25 5/2.75 5/2.5 .9];

figure;scatter(mass,L2);
for i = 1:8
scaledY(:,i) = normY(:,i);
end

out = [mass;L2];
out2 = [x,scaledY];
figure;plot(x,scaledY);

% %Average and StdDev for peak intensity
% peaksAvg = mean(peaks,2);
% peaksStd = std(peaks,0,2);
```

```
% peaksOut = [peaksAvg, peaksStd];
% peaksLoc = [x(67),x(155),x(255),x(751)];
%
%
%
% %Prepare to write out data
% out = [x'; avgY'];
%
% %Print spectral data to text file
file = strsplit(filepath1,'\');
filename = file{length(file)-1};
fileID = fopen(strcat(filename,'.txt'),'w');
fprintf(fileID,'%f \t %f\r\n',out2);
fclose(fileID);
%
% %Print peak data
% filename2 = strrep(filename1{1},'.txt','Peaks.txt');
% fileID2 = fopen(filename2,'w');
% fprintf(fileID2,'%f \t %f \t %f \t %f\r\n',peaksLoc);
% fprintf(fileID2,'%f \t %f \t %f \t %f\r\n',peaksOut);
% fclose(fileID2);


%-----------------------------------%
%Import Peaks and Area
% for k=1:num
%     file = strcat(filepath1,filename1{k});
```

```
%     data =load(file);
%     L2peak(k) = data(1);
%     L2std(k) = data(2);
%     O2(k) = data(3);
%     O2Std(k) = data(4);
% end
%
% mass = [2 5 10 15 20 25 30 40 0];
% scales = mean(O2)./O2;
% %scales = [1 5/4 5/4 5/3.75 5/3.75 5/3.25 5/2.75 5/2.5 1];
% figure;scatter(mass,L2peak.*scales);
% %figure;scatter(mass,area.*scales);
%
% out = [mass ; L2peak.*scales; L2std];
%
% %Print peak data
% filename2 = strrep(filename1{1},'.txt','Peaks.txt');
% fileID2 = fopen('curve3.txt','w');
% fprintf(fileID2,'%f \t %f \t %f \r\n',out);
% fclose(fileID2);
```

APPENDIX C

FLUORESCENCE SPECTROSCOPY PROCESSING CODE

```
%fluorescence background removal and integration
%clear all;close all;
%load
[fn,pn]=uigetfile('*.txt','Choose spectra.');
fp=strcat(pn,fn);           % fp = (full) file path
signal = load(fp);
[fn,pn]=uigetfile('*.txt','Choose background.');
fp=strcat(pn,fn);           % fp = (full) file path
back = load(fp);

%remove offset
offset = mean(signal(300:500,2))
if offset>0
    signal(:,2)=signal(:,2)-offset;
    back(:,2)=back(:,2)-offset;
else
    signal(:,2)=signal(:,2)+offset;
    back(:,2)=back(:,2)+offset;
end

%remove background
scale = max(signal)/max(back);
```

```
back(:,2)=back(:,2).*scale;
newSpec = signal(:,2)-back(:,2);


%calc area
area = sum(newSpec(969:2696))
figure;plot(signal(:,1),signal(:,2),back(:,1),back(:,2));
figure;plot(signal(:,1),newSpec(:,1));
```